

Copyright Warning & Restrictions

The copyright law of the United States (Title 17, United States Code) governs the making of photocopies or other reproductions of copyrighted material.

Under certain conditions specified in the law, libraries and archives are authorized to furnish a photocopy or other reproduction. One of these specified conditions is that the photocopy or reproduction is not to be “used for any purpose other than private study, scholarship, or research.” If a user makes a request for, or later uses, a photocopy or reproduction for purposes in excess of “fair use” that user may be liable for copyright infringement,

This institution reserves the right to refuse to accept a copying order if, in its judgment, fulfillment of the order would involve violation of copyright law.

Please Note: The author retains the copyright while the New Jersey Institute of Technology reserves the right to distribute this thesis or dissertation

Printing note: If you do not wish to print this page, then select “Pages from: first page # to: last page #” on the print dialog screen

The Van Houten library has removed some of the personal information and all signatures from the approval page and biographical sketches of theses and dissertations in order to protect the identity of NJIT graduates and faculty.

ABSTRACT

FUNCTIONALIZATION, GROWTH AND APPLICATIONS OF SINGLE WALL CARBON NANOTUBES

**by
Yubing Wang**

Because of their remarkable structural, mechanical and electrical properties, carbon nanotubes, and especially single wall carbon nanotubes (SWNTs), represent one of the most widely investigated materials today in the emerging field of nanotechnology. The development of oriented growth of SWNTs critical for applications, novel approaches for the creation of functional SWNTs, and applications of both as-prepared and chemically functionalized SWNTs for electrochemically-induced hydrogen storage, *in-situ* formation of new polymer and ceramic nanocomposites with SWNTs, and the fabrication and study for the first time, to the best of our knowledge, of a SWNT-based biofuel cell and self-powered biosensor, are the thrusts of the research discussed in this thesis.

Introduction to the science and the potential applications of carbon nanotubes are presented in Chapters 1 to 2 of the thesis, and an overview of the methods used in this work is discussed in Chapter 3. Chapters 4 to 6 discuss the results of the work performed. Spin-coating deposition of a polymer-chelated catalyst precursor on conductive silicon wafers developed for the oriented growth of SWNTs, is discussed in Chapter 4. Oriented growth of SWNTs was obtained using chemical vapor deposition with alcohol as the carbon source. For application in biofuel cells and biosensors (discussed in the final segment), the oriented SWNTs on silicon were functionalized with selected redox enzymes to form the fuel cell and sensor electrodes. In initial tests, a substantial open

circuit cell voltage of 200 mV, and analyte-sensitive direct electron transfer, were observed from the fabricated biofuel cell and biosensor devices, respectively.

Environmentally friendly, rapid and efficient microwave-induced chemical functionalization of SWNTs was achieved for the first time in the course of this work and is described in Chapter 5 of the thesis. The microwave radiation assisted technique has brought down the functionalization time from days using typical chemical methods, such as refluxing, to the order of minutes. Chemical functionalizations by the microwave method achieved include amidation, 1,3-dipolar cycloaddition and nitration, with the latter providing SWNTs that are very soluble in water and alcohol. Both microwave-induced and supercritical carbon dioxide approaches were also used to prepare and study the formation of ceramic (silicon carbide, SiC) and polymer (polymethyl methacrylate, PMMA) nanocomposites with SWNTs, respectively.

Electrochemically-induced functionalization of SWNTs by nitro groups and enzymes has been studied in some detail, whereas electrochemical hydrogen storage for fuel cell operation using pristine and functionalized SWNTs as the storage medium has also been studied in this work and discussed in Chapter 6 of this thesis. Strong evidence for electrochemically-induced hydrogen uptake approaching 3 wt % based on thermogravimetric measurements has been obtained on SWNT nanopaper membranes on which the nitrogen-containing conducting polymer, polyaniline, was deposited.

A summary of the work performed and suggestions for future work are provided in Chapter 7. The schematic molecular structures of the more complex molecules, polymers and enzymes used in this work (except those shown in the tables) are shown schematically in Appendix A.

**FUNCTIONALIZATION, GROWTH AND APPLICATIONS OF SINGLE WALL
CARBON NANOTUBES**

by
Yubing Wang

**A Dissertation
Submitted to the Faculty of
New Jersey Institute of Technology
in Partial Fulfillment of the Requirements for the Degree of
Doctor of Philosophy in Chemistry**

Department of Chemistry and Environmental Science

August 2005

Copyright © 2005 by Yubing Wang

ALL RIGHTS RESERVED

APPROVAL PAGE

**FUNCTIONALIZATION, GROWTH AND APPLICATIONS OF SINGLE WALL
CARBON NANOTUBES**

Yubing Wang

Dr. Zafar Iqbal, Dissertation Advisor
Research Professor of Chemistry, NJIT

Date

Dr. Somenath Mitra, Committee Member
Professor of Chemistry, NJIT

Date

Dr. Joseph Bozzelli, Committee Member
Distinguished Professor of Chemistry, NJIT

Date

Dr. Sergiu Gorun, Committee Member
Associate Professor of Chemistry, NJIT

Date

Dr. Frank Owens, Committee Member
Senior Scientist, Armament Research, Development and Engineering Center,
Picatinny, NJ

Date

BIOGRAPHICAL SKETCH

Author: Yubing Wang
Degree: Doctor of Philosophy
Date: August 2005

Undergraduate and Graduate Education:

- Doctor of Philosophy in Chemistry
New Jersey Institute of Technology, Newark, NJ, 2005
- Bachelor of Science in Medicinal Chemistry
West China University of Medical Sciences, China, June 1998

Major: Chemistry

Selected Publications and Presentations:

- Wang, Y., Mitra, S., Iqbal, Z. 'Microwave-induced, "green" and rapid chemical functionalization of single-walled carbon nanotubes', American Chemical Society 229th, 2005, San Diego, CA
- Wang, Y., Iqbal, Z. "Hydrogen Sorption/Desorption in Surface-Modified Single Wall Carbon Nanotube", MRS Fall Meeting 2004, Boston, MA
- Wang, Y., Malhotra, S. V., Iqbal, Z. "Electrochemical Nitration of Single Wall Carbon Nanotubes", American Chemical Society 228th, 2004, Philadelphia, PA
- Wang, Y., Malhotra, S., Iqbal, Z. "Nanoenergetics with Carbon Nanotubes", MRS Fall Meeting 2003, Boston, MA
- Wang, Y., Malhotra, S. V., Owens, F. J., Iqbal, Z. "Electrochemical nitration of single-walled carbon nanotubes", Chem. Phys. Lett. 407, 68-72 (2005).
- Wang, Y., Iqbal, Z., Malhotra, S. "Functionalization of carbon nanotubes with amines and enzymes", Chem. Phys. Lett. 402, 96-101 (2005).

- Wang, Y., Iqbal, Z., Mitra, S. "Microwave-induced rapid chemical functionalization of single-walled carbon nanotubes", *Carbon* 43, 1015-1020 (2005).
- Wang, Y., Iqbal, Z. "Electrochemical hydrogen adsorption/chemisorption on single-walled carbon nanotubes", *Mater. Res. Soc. Symp. Proc. Vol. 837, N4.4.1* (2005).
- Wang, Y., Iqbal, Z. "Vertically Oriented Single Wall Carbon Nanotube/Enzyme on Silicon as Biosensor Electrode" *J. Minerals, Metals and Materials* 58, 27-29 (2005).
- Wang, Y., Iqbal, Z., Mitra, S. "Rapidly functionalized and highly water-soluble carbon nanotubes", submitted to *J. Am. Chem. Soc.*
- Wang, Y., Iqbal, Z., Mitra, S. "Synthesis of silicon carbide and single-walled carbon nanotube composite", submitted to *Carbon*.

To my beloved family

ACKNOWLEDGEMENT

I would like to express my greatest gratitude towards my advisor, Prof. Zafar Iqbal, for his guidance, support and all other opportunities he provided me during the course of this study. I would also like to express my deepest appreciation to Prof. Somenath Mitra for his guidance and help. I am very thankful to Prof. Joseph Bozzelli, Prof. Sergiu Gorun, and Dr. Frank Owens (US Army, Picatinny) for serving on my thesis committee.

I would also like to thank Prof. Sanjay V. Malhotra for his help and advice. I greatly appreciate Mr. Yogish Gandhi, Supervisor of the Chemistry Laboratory at NJIT, for all his help. I thank all my colleagues Dr. Yan Zhang, Dr. Xueyan Zhang, Dr. Aidong Lan, Dr. Cheng Li, Amit Goyal, Baohua Xue, Hui Han, Jing Cheng, and Husnu Emrah Unalan (Rutgers) for their help and friendship.

Financial support from the US Army, ARDEC-Picatinny and the Chemistry and Environmental Science Department of NJIT, is gratefully acknowledged.

I am deeply grateful to my wife and my parents for their love and support throughout all these years.

TABLE OF CONTENTS

Chapter	Page
1 INTRODUCTION.....	1
1.1 Objectives and Rationale.....	1
1.2 Background	2
1.2.1 Different Forms of Carbon.....	2
1.2.2 Carbon Nanotubes.....	4
1.2.3 Characterization of Single Wall Carbon Nanotubes.....	10
2 REVIEW OF PRIOR WORK ON SYNTHESIS, FUNCTIONALIZATION AND POTENTIAL APPLICATIONS OF SINGLE WALL CARBON NANOTUBES....	14
2.1 Synthesis	14
2.1.1 Arc-discharge.....	14
2.1.2 Laser Ablation.....	15
2.1.3 Chemical Vapor Deposition.....	16
2.2 Functionalization of Single Wall Carbon Nanotubes.....	21
2.2.1 Non-covalent Wrapping or Adsorption.....	21
2.2.2 Functionalization of SWNTs involving Covalent Bonding	22
2.3 Applications of Single Wall Carbon Nanotubes.....	26
2.3.1 Potential Applications of SWNTs in Micro- or Nano-electronics.....	26
2.3.2 Hydrogen Storage.....	28
2.3.3 SWNT-filled nanocomposites.....	31
3 OVERVIEW OF RESEARCH CONDUCTED AND METHODOLOGIES USED.	33

TABLE OF CONTENTS
(Continued)

Chapter	Page
3.1 Synthesis of Single Wall Carbon Nanotubes (SWNTs) Using Chemical Vapor Deposition Method.....	33
3.2 Functionalization of Single Wall Carbon Nanotubes.....	35
3.2.1 Functionalization Approaches.....	35
3.2.2 Basics of Microwave-Induced Chemistry.....	37
3.3 Applications of Single Wall Carbon Nanotubes.....	39
3.4 Characterization.....	41
4 SYNTHESIS OF SINGLE WALL CARBON NANOTUBES.....	43
4.1 Introduction.....	43
4.2 Experimental Section.....	44
4.3 Results and Discussion.....	46
5 FUNCTIONALIZATION OF SINGLE WALL CARBON NANOTUBES.....	53
5.1 Introduction.....	53
5.2 Functionalization of Single Wall Carbon Nanotubes With Amines and Enzymes.....	54
5.3 Microwave-Induced Rapid Chemical Functionalization of Single Wall Carbon Nanotubes.....	63
5.3.1 Amidation	64
5.3.2 1,3-dipolar cycloaddition.....	68
5.3.3 Preparation and Characterization of Rapidly Functionalized Highly Water-Soluble Carbon Nanotubes.....	73
5.4 Electrochemical Nitration of Single Wall Carbon Nanotubes.....	80
6 APPLICATIONS OF SINGLE WALL CARBON NANOTUBES.....	90

TABLE OF CONTENTS
(Continued)

Chapter	Page
6.1 Introduction.....	90
6.2 Electrochemical Hydrogen Adsorption/Storage in Pure and Functionalized Single Wall Carbon Nanotubes.....	91
6.3 Single Wall Carbon Nanotube Reinforced Ceramic and Polymeric Composites	100
6.3.1 Rapid, Low Temperature Microwave Synthesis of Novel Carbon Nanotube- Silicon Carbide Composite.....	100
6.3.2 Synthesis of Carbon Nanotube/Poly Methyl Methacrylate Nanocomposite in Supercritical Carbon Dioxide.....	109
6.4 Applications of Vertical Oriented Single Wall Carbon Nanotubes in Biofuel Cell and Biosensor.....	120
7 SUMMARY.....	128
APPENDIX.....	131
REFERENCES.....	133

LIST OF TABLES

Table		Page
2.1	Energy Densities of Various Fuels.....	28
2.2	Hydrogen Sorption Characteristics for Different Carbon Nanomaterials...	30

LIST OF FIGURES

Figure		Page
1.1	Four allotropes of carbon.....	3
1.2	Images of MWNTs.....	5
1.3	The chiral vector of a single wall carbon nanotube.....	6
1.4	Schematic models for single-wall carbon nanotubes with the nanotube axis normal to the chiral vector of different θ	7
1.5	TEM images of SWNTs bended in different angle.....	9
1.6	Kataura plot generated for SWNTs in a diameter range of 0.4 to 3 nm.....	11
1.7	Raman spectrum of SWNTs showing radical breathing mode (RBM), G-band and D-band.....	12
2.1	Schematic setup of arc-discharge system used for nanotube growth.....	14
2.2	Schematic illustration of a laser ablation setup and a TEM image of a bundle of SWNTs produced with a continuous laser	16
2.3	Schematic illustration of a CVD setup for carbon nanotubes synthesis.....	17
2.4	Carbon nanotube growth models.....	19
2.5	SEM images of suspended and aligned SWNTs.....	20
2.6	Non-covalent functionalization of SWNTs.....	22
2.7	Reversibly stored amount of hydrogen on various carbon materials versus the specific surface area.....	31
3.1	Schematic illustration of the CVD system used.....	34
3.2	Photograph of the microwave system used.....	36
3.3	Schematic depiction of the dipolar polarization mechanism.....	37
3.4	Schematic depiction of the conduction mechanism.....	39

LIST OF FIGURES
(Continued)

Figure	Page
4.1 SEM image and Raman spectrum of the purified SWNTs obtained from bulk synthesis.....	46
4.2 SEM image from the edge of vertically aligned SWNT film on silicon obtained using the dip-coating method for depositing the catalyst/promoter precursors.....	47
4.3 SEM and TEM images of vertically aligned SWNTs on Si obtained from polymer (PVP) supported catalyst/promoter.....	48
4.4 Raman spectrum of the vertically aligned SWNTs.....	49
4.5 SEM image of catalyst/promoter particles obtained from the spin coating procedure.....	50
4.6 Photographs of different catalyst/promoter solution.....	51
4.7 SEM image of unevenly distributed SWNTs from the 0.05wt% of Mo and Co and 2 wt% (or more) of PVP (in 90% ethanol) catalyst precursor.....	52
5.1 ATR-FTIR spectra of functionalized SWNTs.....	59
5.2 Raman spectra of SWNTs before and after functionalization.....	60
5.3 UV-vis absorption spectra of SWNT-PPL and SWNT-AK.....	61
5.4 FE-SEM images of SWNTs before and after functionalization.....	62
5.5 FTIR spectra from the amidation reaction of SWNTs.....	67
5.6 Raman spectra from the amidation of SWNTs.....	68
5.7 FTIR spectra from the 1,3-dipolar cycloaddition of SWNTs.....	70
5.8 SEM images of pristine and functionalized SWNT bundles.....	71
5.9 UV-vis-NIR spectra of pristine and functionalized SWNTs.....	73
5.10 Photographs of SWNTs solution in DI water.....	75
5.11 SEM and TEM images of functionalized SWNTs deposited from aqueous solution.....	76

LIST OF FIGURES
(Continued)

Figure	Page
5.12 FTIR and Raman spectra of the functionalized SWNTs.....	78
5.13 Vis-NIR spectra and TGA of pristine and microwave functionalized SWNTs.....	79
5.14 The cyclic voltammogram of a SWNT nanopaper in 6M KNO ₂ aqueous solution.....	82
5.15 Raman spectra of SWNTs before and after electrochemical charging.....	84
5.16 TEM images of SWNT bundles before and after electrochemical nitration..	85
5.17 ATR-FTIR spectra of the SWNT sheet before and after electrochemical nitration.....	87
5.18 DTA and TGA data of SWNTs after electrochemical nitration.....	88
6.1 Schematic of set-up for electrochemical hydrogen adsorption.....	93
6.2 Cyclic voltammograms from the electrochemical hydrogen adsorption of different SWNT sheets.....	95
6.3 Tangential mode Raman of SWNT sheet before and after electrochemical hydrogen adsorption.....	96
6.4 Raman spectra and TGA data of Mg functionalized nanopaper before and after electrochemical hydrogen adsorption.....	97
6.5 Raman and FTIR spectra of Co functionalized nanopaper before and after electrochemical hydrogen adsorption.....	98
6.6 TGA data of polyaniline functionalized carbon paper, and SWNT sheet before and after electrochemical hydrogen adsorption.....	99
6.7 Optical picture of the SWNTs and SiC composite.....	102
6.8 XRD of SiC-SWNT composite.....	103
6.9 FTIR spectra of SiC-SWNT composite and the starting material.....	105
6.10 Raman spectra of pristine SWNTs and SiC-SWNT composite.....	106

LIST OF FIGURES
(Continued)

Figure	Page
6.11 SEM and TEM images of SWNTs-SiC composite.....	107
6.12 Growth mechanism and pictorial illustration of the SiC-SWNT composite..	108
6.13 FTIR spectra of SWNT-COOH, SWNT-AEMA and, SWNT-PMMA.....	114
6.14 SEM images of SWNT-COOH and SWNT-AEMA, and the photo images of the nanotube sample in the polymerization mixture.....	115
6.15 SEM images of PMMA and PMMA/CNT composite.....	116
6.16 SEM images of the PMMA/CNT composite after first wash with acetone...	117
6.17 SEM images of PMMA/CNT composite after second wash and third wash or more.....	117
6.18 TEM images of pristine CNT and PMMA/CNT composite.....	118
6.19 SEM image of PMMA coating of unmodified CNT bundles.....	119
6.20 Cyclic Voltammogram of oriented SWNT film on silicon with 50 mM β - NAD synthetase.....	123
6.21 SEM images of pristine and enzyme-functionalized, oriented SWNT film on silicon.....	124
6.22 Schematic illustration of the fuel cell set up.....	125
6.23 Schematic set up of a glucose biosensor.....	126
6.24 CV curves of the biosensor electrode in pH 7 phosphate buffer with and without glucose.....	127

CHAPTER 1

INTRODUCTION

1.1 Objectives and Rationale

The primary objective of the work described in this thesis is to synthesize and characterize single wall carbon nanotubes (SWNTs) that are chemical functionalized via side-wall bonding to energetic and biologically active molecules, such as nitro groups, amines, nitroanilines and enzymes. Different new and previously investigated methods for functionalization will be used and *in-situ* methods for the formation of polymer and ceramic nanocomposites will be studied. The functionalized SWNTs prepared will be used to study electrochemically-induced hydrogen adsorption and storage, fabricate a biofuel cell and a biosensor device, and evaluate nanoscale energetics or energy release processes. Since the formation of large-scale, aligned SWNT architectures are critical for nanotube applications, a secondary objective of this work will be to develop chemical vapor growth of vertically aligned SWNT arrays on conductive platforms (such as, doped silicon) and demonstrate their use as biofuel cell and biosensor devices after functionalization with biocatalysts.

The as-prepared SWNTs used in these studies will be either synthesized in-house or obtained from commercial sources (for example, Carbon Nanotechnologies Inc and Carbolex Inc). Electrochemically-induced hydrogen storage and nitration and electrochemical functionalization by the conducting polymer, polyaniline, will involve the use of thermally annealed SWNTs in the form of self-assembled membranes (also referred to as nanopaper).

One rationale for this work, for example, for nitration is that it would lead in combination with hydrogen insertion or chemisorption to novel nanoscale energetic materials for defense applications. Functionalization involving charge transfer is expected to make the normally inert SWNTs soluble in water and other common solvents, which will subsequently lead to easy processability for applications in medical and biological fields, as well as in the fabrication of high strength nanocomposites.

1.2 Background

1.2.1 Different Forms of Carbon

There are four different allotropes of carbon, which are: graphite, diamond, fullerenes and nanotubes. Diamond forms under the conditions of extremely high temperature and pressure. It is the most precious mineral found in nature. It is transparent, highly insulating in its pure form and the hardest material known. As shown in Figure 1.1(a), in diamond each carbon is sp^3 hybridized and forms four equivalent σ covalent bonds with the four neighbouring carbons in the tetrahedral direction.

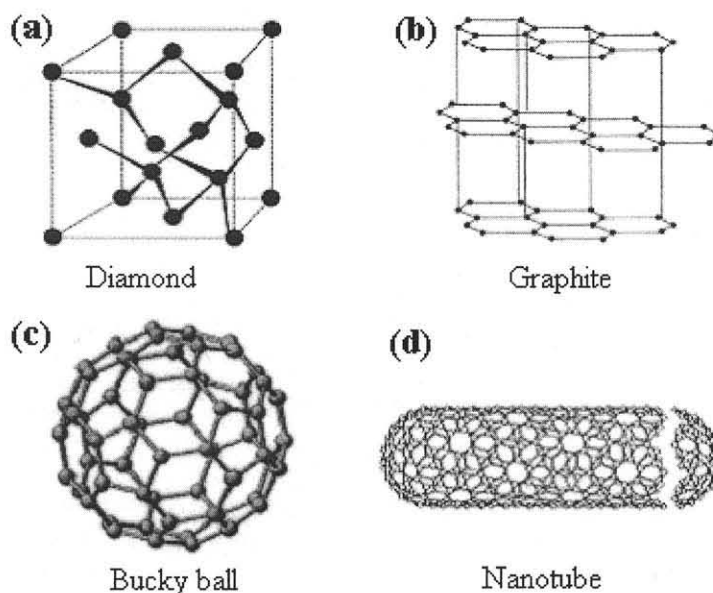


Figure 1.1 Four allotropes of carbon: (a) diamond, (b) graphite, (c) fullerene and (d) carbon nanotube [1].

Graphite is the most abundant and most stable allotrope of carbon at one atmosphere and ambient temperature. It is composed of hexagonal sheets, usually referred to as graphene layers, which are held parallel to each other by van der Waals forces. The weak van der Waals interaction between the sheets makes graphite soft. As shown in Figure 1.1(b), each carbon atom is sp^2 hybridized in graphite, and the delocalized π electrons makes graphite thermally and electrically conductive along the direction of its graphene layers.

There also exists a whole range of closed-caged carbon structures called fullerenes, the most famous of which is the C_{60} molecule. C_{60} , also called bucky ball, is made of 20 hexagons and 12 pentagons, which is shown as Figure 1.1(c). The bonding in bucky ball is also sp^2 , but it is mixed with sp^3 character because of the high curvature.

As a new member of the family of carbon allotropes, carbon nanotube (CNT), shown as Figure 1.1(d), is the material lying between graphite and fullerenes. A CNT can be viewed as a hollow and seamless cylinder formed by rolling up a graphene sheet, and

capped with half a fullerene at each end. Bonding in CNTs is essentially sp^2 . However, the circular curvature will cause quantum confinement and σ - π rehybridization in which three σ bonds are slightly out of plane; for compensation, the π orbital is more delocalized outside the tube. This makes nanotubes mechanically stronger, electrically and thermally more conductive, and chemically and biologically more active than graphite [2]. Nanotubes can be either single walled or multiwalled. Double walled tubes have also been prepared and can be considered to be a sub-set of multiwalled tubes.

1.2.2 Carbon Nanotubes

Carbon nanotubes (CNTs) can be either single walled or multiwalled. The geometry of a single walled carbon nanotube (SWNT) can be imagined as one layer of graphite (so-called graphene) rolled into a seamless cylinder with a typical diameter of 1~2 nanometers (nm). As indicated in Figure 1.2(a), a multi-walled carbon nanotube (MWNT) is comprised of multiple, concentrically arranged set of SWNTs with an interlayer spacing of 0.34 nm and a typical diameter of 10~20 nm. In 1991, Iijima reported the first observation of MWNTs [3]. About two years later, he reported the observation of SWNTs [4]. The structure of carbon nanotubes was explored by high resolution Transmission Electron Microscopy (TEM) and Scanning Tunneling Microscopy (STM) [5], yielding direct confirmation that they are seamless cylinders derived from the honeycomb lattice representing a single atomic layer of a graphene sheet. Figure 1.2(b) shows the TEM images of MWNTs [3].

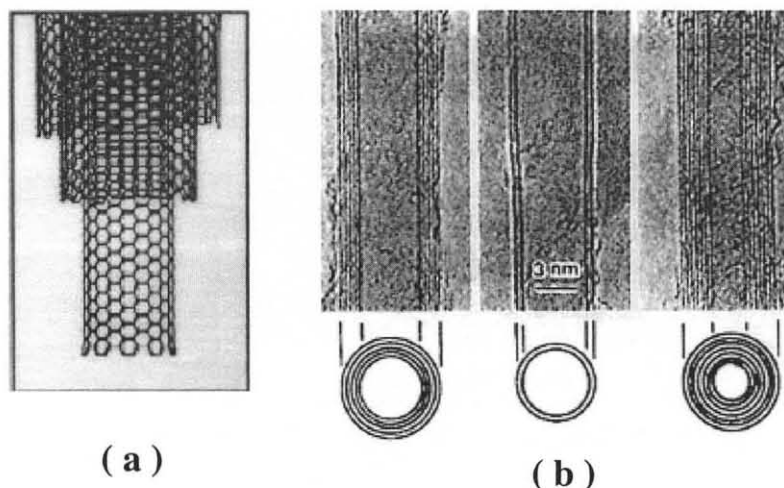


Figure 1.2 Images of MWNTs: (a) Schematic illustration of a MWNT [6]; (b) TEM images of different MWNTs with two and more number of SWNT layers [3].

For a single-wall carbon nanotube, its cylinder-like structure is explained in terms of an one-dimensional (1D) unit cell, defined by the vectors C_h and T in Figure 1.3a [7]. The circumference of a carbon nanotube is expressed in terms of the chiral vector $C_h = n\hat{a}_1 + m\hat{a}_2$, which connects two crystallographically equivalent sites on a 2D graphene sheet [7]. Three distinct types of nanotubes: armchair, zigzag, and chiral nanotubes can be constructed, depending on how the two-dimensional graphene sheet is rolled up. The different types of SWNTs can be explained in terms of the unit cell of a carbon nanotube. The integers n and m specify the chiral vector C_h , and \hat{a}_1 and \hat{a}_2 are the unit vectors of the 2D hexagonal lattice. Another important parameter is the chiral angle θ , which is the angle between C_h and \hat{a}_1 . When the graphene sheet is rolled up to form the nanotube, the ends of the chiral vector meet each other [8]. The chiral vector (C_h) thus forms the circumference of the nanotubes' circular cross-section, and different values of n and m lead to different nanotube structures of different diameters (Figure 1.3b).

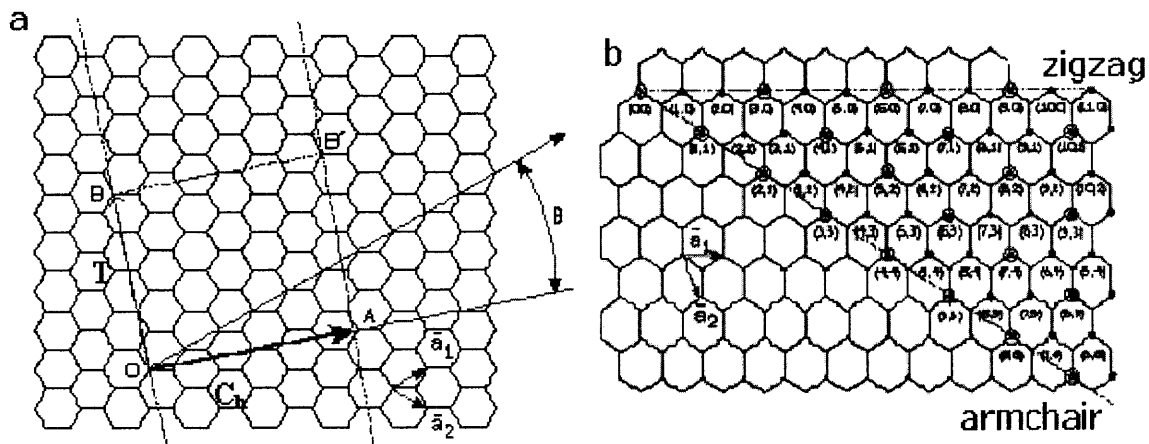


Figure 1.3 (a). The chiral vector OA or $C_h = n\hat{a}_1 + m\hat{a}_2$ is defined on the honeycomb lattice of carbon atoms by unit vectors \hat{a}_1 and \hat{a}_2 and the chiral angle θ with respect to the zigzag axis $\theta = 0^\circ$. Along the zigzag axis $\theta = 0^\circ$. (b) Possible vectors specified by the pairs of integers (n, m) for general carbon nanotubes including zigzag, armchair, and chiral nanotubes [7].

Figure 1.4 shows the three different types of single-walled nanotubes (armchair, zigzag, and chiral). Armchair nanotubes are formed when $n=m$ and the chiral angle is 30° . Zigzag nanotubes are formed when either n or m is zero and the chiral angle is 0° . All others are chiral nanotubes with $0^\circ < \theta < 30^\circ$ [8]. The unit cell of the 1D lattice is the rectangle defined by the chiral vector C_h and the translation vector T . The two ends of each cylinder either have dangling bonds or are capped by two hemispherical fullerenes.

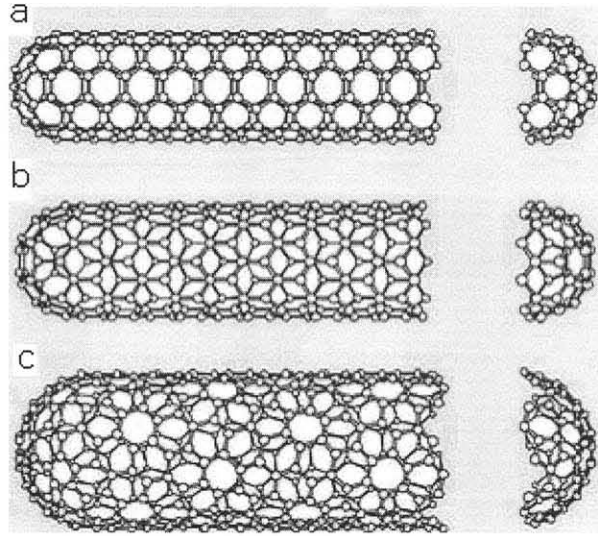


Figure 1.4 Schematic models for single-wall carbon nanotubes with the nanotube axis normal to the chiral vector of: (a) $\theta = 30^\circ$ [an armchair (5,5) nanotube], (b) $\theta = 0^\circ$ [a zigzag (9,0) nanotube], (c) $0 < \theta < 30^\circ$ (a chiral tube), which corresponds to a (10,5) tube [9].

The properties of the nanotubes are determined by their different chiral angles and diameters, and both of them depend on n and m . The nanotubes are metallic if $n = m$ or $n - m = 3d$ where d is an integer. For all the others, the tube is a semiconductor. Their chiral angle θ and diameter (d_t) are respectively given by:

$$\theta = \tan^{-1} [\sqrt{3}n/(2m+n)], \quad (1.1)$$

and

$$d_t = \sqrt{3}a_{C-C}(m^2+mn+n^2)^{1/2}/\pi = C_h/\pi \quad (1.2)$$

Where C_h is the length of the chiral vector C_h , a_{C-C} is the C-C bond length [8].

Typical diameters of individual tubes are in the range of 0.7 to about 2 nm, although smaller and larger diameter nanotubes have been reported [10,11]. SWNTs produced by the different methods typically tend to self-assemble via van der Waals forces into hexagonally arranged bundles, with bundle diameters typically of a few ten nanometers and tube/bundle lengths from a few micrometers up to 100 μm or more.

There are two general categories of nanotubes: SWNTs and MWNTs. The latter are nested SWNTs and those with large diameters are similar to hollow graphite fibers. MWNTs comprise of concentric cylinders placed around a central tubular pore, with the sidewall layers separated by 0.34 nm, which is close to the interplanar distance in graphite [12]. The smallest MWNTs comprise of two walls. They have similar 1D properties as SWNTs and are usually referred to as double-wall nanotubes (DWNTs).

The basic structure of the nanotube lattice is the C-C sp^2 bond (as in the graphite planes). The perfect alignment of the lattice along the tube axis and the closed topology endows nanotubes with the in-plane properties of graphite, such as high conductivity, excellent strength and stiffness, chemical inertness together with some unusual properties, such as electronic properties that are dependent on helicity, quasi-one dimensionality and elasticity [12]. In addition, the nanoscale dimensions provide a large surface area, which is useful in mechanical and chemical applications [12].

By chemical doping with holes and electrons, the electrical conductivity of the semi conducting SWNTs and MWNTs can be increased. The doped nanotubes might be considered as a new generation of unique synthetic metals [13,14]. In addition to their novel electronic properties, the mechanical properties of nanotubes are fascinating as well. The strength of the carbon bonds and high aspect ratios makes nanotubes the strongest and stiffest material known [15]. The hollow structure and closed topology of nanotubes produce a distinct mechanical response in nanotubes compared to that of other graphitic structures. Nanotubes can sustain extreme strains (40%) in tension without showing signs of brittle behavior, plastic deformation, or bond rupture [16].

The topology leads to stepwise deformation behavior in nanotubes. Highly deformed nanotubes are observed to reversibly switch into different morphological patterns with an abrupt release of energy (Figure 1.5) [17]. The reversibility of deformations, such as buckling, has also been seen in TEM studies [12,17]. The elastic property of CNTs is related to the in-plane flexibility of the graphene sheet and the ability of carbon atoms to undergo sp^2 to sp^3 rehybridization.



Figure 1.5 TEM images of SWNTs bent at different angles [17].

CNTs are not entirely chemically inert. Earlier oxidation studies show that the ends of the nanotubes are more reactive than the walls [18,19]. The presence of pentagonal defects at the ends and the higher curvature caused by these defects are responsible for the enhanced reactivity of the tube tips. In addition to the reactive tip, the presence of a large number of topological defects (bond rotational defects or pairs of 5-7 rings) can also enhance the reactivity of the tube walls.

In summary, strong covalent bonding, unique one-dimensional structure and nanometer size combine to impart CNTs and in particular SWNTs with exceptionally high mechanical strength, high resilience, and novel electronic properties ranging from metallic to semi-conducting with the ability to sustain high current densities, and high thermal conductivity that is greater than that of diamond along the tube axis. With all these remarkable properties, CNTs have tremendous potential for use as quantum wires

in nanoelectronics and heterojunction devices, nanoprobe for scanning probe microscopes, field-effect transistors, light emitters for flat panel displays, gas sensing devices, components for forming novel nanocomposites, and in energy production and storage devices. They are indeed one of the most fascinating nanoscale materials known today.

1.2.3 Characterization of Single Wall Carbon Nanotubes

Raman spectroscopy and electron microscopy are the most commonly applied and most powerful techniques used for the characterization of carbon nanotubes.

The Raman spectrum of SWNTs is understood in terms of resonance enhancement in a one-dimensional conductor with the so-called van Hove singularities in the electronic density of states. More specifically, when the incident photons in the Raman process are in resonance with an electronic transition between the valence and conduction bands of a nanotube at the special energy states, E_{ij} , the Raman signal becomes very large as a result of the strong coupling, which occurs between the electrons and phonons of the nanotube under these resonance conditions. Calculations have been performed by Kataura and coworkers [20] to correlate nanotube diameters with transition energies across the so called van Hove singularities induced in the electron density-of-states by the 1D structure of the SWNTs. This so-called Kataura plot is shown in Figure 1.6. In this plot, the interband energies E_{ij} , denoting the energy difference between i^{th} van Hove singularities in the conduction and valence bands, are plotted as a function of nanotube diameter. This plot is useful in determining whether a given laser excitation wavelength couples to semi conducting or metallic SWNTs. Then the corresponding unique (n, m) values of the SWNTs in the sample can in general be identified.

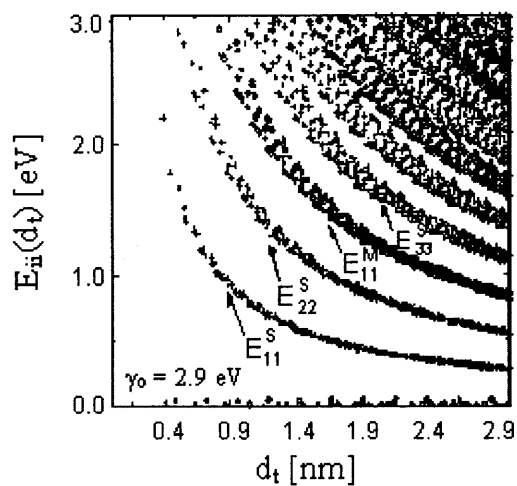


Figure 1.6 Kataura plot generated for SWNTs in a diameter range of 0.4 to 3 nm [20].

Resonance Raman spectroscopy has played an important role in the characterization of carbon nanotubes, to determine the diameter distribution in SWNT bundles (an ensemble of different tubes with different diameters and chiralities) and also to determine whether a nanotube is metallic or semi conducting [21]. As indicated in Figure 1.7, the Raman spectrum shows three important features of SWNTs, which include the radial breathing mode (RBM) lines, the tangential mode lines (G) and the disorder induced line (D).

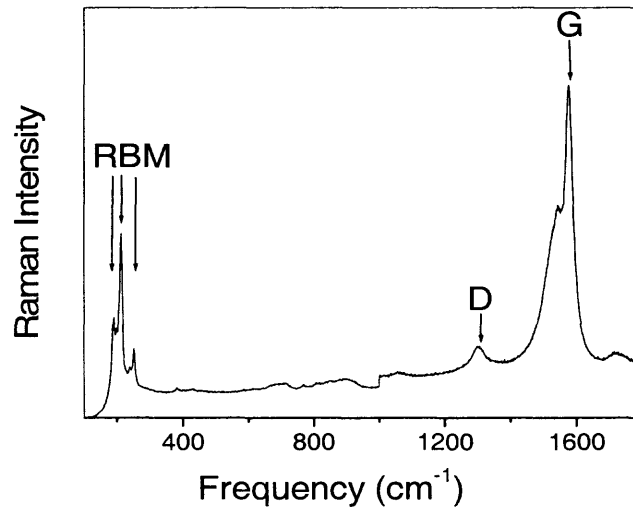


Figure 1.7 Raman spectrum of SWNTs showing radical breathing mode (RBM), G-band and D-band.

In the RBM, all carbon atoms move in-phase in the radial direction. The frequency (ω , cm^{-1}) of the RBM Raman line varies linearly with the reciprocal of the tube diameter (d_t , nm) and is given by the relation:

$$\omega_{\text{RBM}} = \alpha/d_t \quad (1.3)$$

where α is a constant which is equal to 248 cm^{-1} for an isolated tube. The RBM frequency therefore serves as a convenient tool for the determination of the diameter of individual tubes, which is one of the parameters needed to determine the tube indices (n , m). Because of tube-tube interactions in a bundle, equation 1.1 can be written as:

$$d_t = (238/\omega_{\text{RBM}})^{1.075} \quad (1.4)$$

In the G-band mode, all the neighboring carbon atoms are moving in opposite directions tangential to the surface of the tube as in 2D graphite. By rolling a graphite sheet into a nanotube, the tube curvature lifts the degeneracy of the tangential mode, resulting in two primary lines that correspond to an axial and circumferential tangential mode. Therefore there are typically two, well-defined peaks seen in the tangential mode

region for SWNTs. However, further field splitting of the G-mode lines are also observed. Moreover, the tangential mode in metallic tubes shows a broader line shape than in semi conducting SWNTs because of electron-phonon coupling effects.

The disorder-induced D-band is the third distinct line that appears in the Raman spectrum of SWNTs, and is similar in origin to the disorder-induced line seen in nanoscale graphite. It is associated with defects and amorphous carbon on the SWNT sidewalls.

Electron microscopy, such as Transmission Electron Microscopy (TEM) and Scanning Electron Microscopy are also very common and powerful techniques used for the characterization of carbon nanotubes. In fact, the first observations of MWNTs and SWNTs were made using high resolution TEM. SEM and TEM provide images of the tubular structure of nanotubes; TEM in addition allows one to clearly distinguish SWNTs from MWNTs. Localized defects and impurities can be determined by TEM and SEM respectively. Additionally, the orientation of as-prepared oriented architectures can be evaluated SEM imaging.

Pristine carbon nanotubes show very limited or no features in the mid-infrared spectral region because of the near-absence of infrared activity of the nanotube vibrations. However, after attaching functional groups to the nanotubes, new features appear in the Fourier Transform Infrared (FTIR) spectrum. Therefore FTIR together with Nuclear Magnetic Resonance (NMR) are frequently used for the characterization of functionalized nanotubes.

CHAPTER 2

REVIEW OF PRIOR WORK ON SYNTHESIS, FUNCTIONALIZATION AND POTENTIAL APPLICATIONS OF SINGLE WALL CARBON NANOTUBES

2.1 Synthesis

Carbon nanotubes can be synthesized by several different methods. The three most widely used methods for the growth of SWNTs will be briefly discussed here. These three methods include arc discharge, laser ablation and chemical vapor deposition (CVD).

2.1.1 Arc-discharge

In the arc-discharge method, carbon atoms from graphite are evaporated by the plasma of helium gas ignited by a high current passed between opposing graphite electrodes (Figure 2.1). The carbon atoms generated then grow into carbon nanotubes.

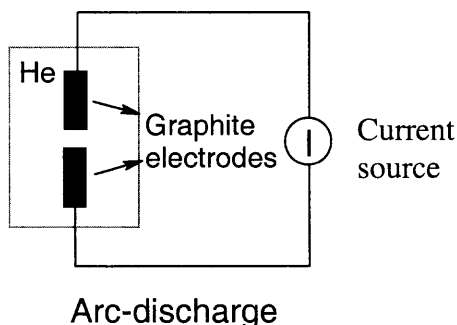


Figure 2.1 Schematic setup of arc-discharge system used for nanotube growth [22].

For the synthesis of SWNTs, the anode is comprised of graphite mixed with a metal catalyst (Fe, Co, Ni, Y, or Mo). The first success in producing appreciable amounts of SWNTs by the arc-discharge method was achieved by Bethune and coworkers in 1993 [23]. A small amount of Co catalyst embedded in the anode was used in their experiment. SWNTs synthesized by the arc-discharge method contain large fractions of metal catalyst

and defected carbon, and are difficult to purify. Because of the high temperatures involved narrow diameter distributions of the most stable SWNT configurations are formed by this method. The optimization of SWNT growth by arc-discharge was achieved by Journet and coworkers using a carbon anode containing 1.0 atomic weight % of yttrium mixed with 4.2 atomic weight % of nickel as catalyst [24].

2.1.2 Laser Ablation

In 1996, Smalley's group at Rice University reported a 1~10 g scale synthesis of carbon nanotubes by laser vaporization [25]. As shown in the schematic setup of Figure 2.2a, in the laser ablation method, a pulsed (such as a Nd:YAG laser) or a continuous CO₂ laser can be used to vaporize a graphite target in an oven. The main difference between continuous and pulsed lasers, is that the pulsed laser produces a much higher power density (100 kW/cm² compared with 12 kW/cm²). The method used by Smalley's group utilized intense laser pulses to ablate a graphite target containing 0.5 atomic percent of nickel and cobalt. The target was placed in a 1200°C tube-furnace. During laser ablation, a flow of inert gas was passed through the growth chamber to carry the growing nanotubes downstream to be collected on a cold finger. The SWNTs produced were mostly in the form of ropes consisting of tens of individual nanotubes closed-packed into a hexagonal lattice by van der Waals forces (see Figure 2.2b).

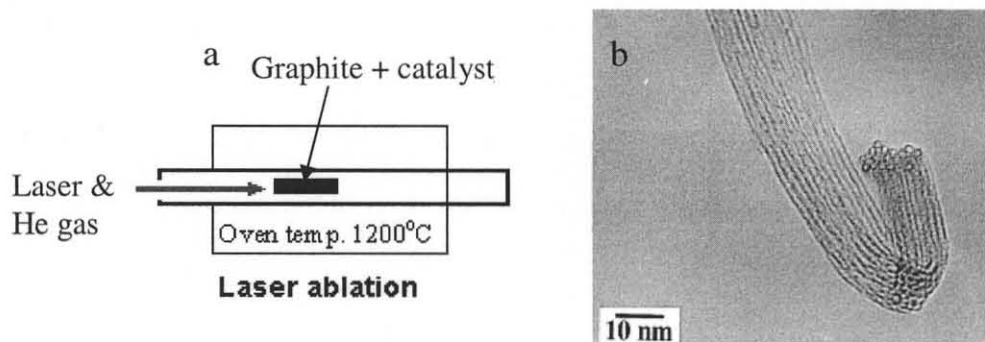


Figure 2.2 (a) Schematic illustration of a laser ablation setup, (b) TEM image of a bundle of SWNTs catalyzed by Ni/Y (2:0.5 at. %) mixture, produced with a continuous laser [26].

The laser ablation method results in a higher yield of SWNTs than in the arc-technique and the nanotubes have fewer defects and a somewhat narrower diameter distribution than SWNTs produced by arc-discharge. Laser ablation is similar to arc discharge, since the optimum background gas and catalyst mix is same in the two methods. In SWNT growth by arc-discharge and laser ablation, typical by-products include fullerenes, graphitic polyhedrons with enclosed metal particles, and amorphous carbon in the form of particles or overcoating on the sidewall of the nanotubes [22]. A purification process for SWNT materials has been developed by Smalley and coworkers involving refluxing of the as-prepared product in concentrated nitric acid for about 45 hours, and is now widely used [27].

2.1.3 Chemical Vapor Deposition

A schematic experimental setup for chemical vapor deposition (CVD) growth is depicted in Figure 2.3. The growth process involves putting a carbon source in the gas phase and using an energy source, such as plasma, a resistively heated coil or a furnace, to transfer

energy to the gaseous precursor carbon molecule. Commonly used carbon sources include methanol, ethanol, methane, carbon monoxide and acetylene. Materials grown over the catalyst can be collected after cooling to room temperature. The key parameters in nanotube growth by this method are the carbon source, catalyst and the growth temperature. The general nanotube growth mechanism in a CVD process involves the dissociation of the carbon source catalyzed by a transition metal catalyst (for example, Ni, Fe, or Co) and a catalyst promoter (typically, Mo), followed by dissolution and saturation of carbon atoms in the metal particle. The precipitation of carbon from the saturated metal particle leads to the formation of tubular carbon solids with sp^2 bonding [22]. Nanotube formation is favored over other forms of carbon, such as graphitic sheets with open edges. This is because a capped tube contains no dangling bonds and therefore is a low energy form [22].

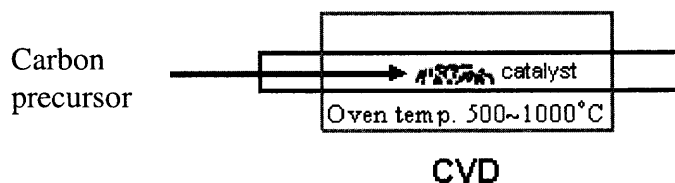


Figure 2.3 Schematic illustration of a CVD setup for carbon nanotubes synthesis [22].

Both arc-discharge and laser ablation methods rely on evaporating carbon from solid carbon sources at 3000°C or above. These processes are not energy-efficient and limit the scale-up production of SWNTs. Additionally, SWNTs obtained from both methods are difficult to purify and manipulate. Recently, CVD methods were developed for the synthesis of SWNTs. CVD methods are simple and easy to scale up and can be used to grow aligned SWNTs for device applications, as will be demonstrated later in this thesis. High temperatures, but only up to 700-1000°C are necessary to form SWNTs by

the CVD technique. The SWNTs formed have small diameters and thus high strain energies, and allow for the formation of nearly-defect free nanotube structures [22]. Various gaseous carbon sources have been chosen for growth of SWNTs by the CVD method. However, the catalytic decomposition temperature varies among these precursor molecules. Therefore, the choices of carbon feedstock and growth temperature are the key elements in the CVD synthesis of high quality SWNTs containing no defects and amorphous carbon over-coating on the sidewalls. In the methane CVD approach for SWNT growth, researchers have found that the chemical and textural properties of the catalyst materials dictate the yield and quality of the SWNTs produced [22]. Catalyst optimization is proposed to be based on the finding that a good catalyst material for SWNT synthesis should exhibit strong metal-support interactions, possess high surface area and large pore volume. The strong metal-support interactions allow high metal dispersion and thus a high density of catalyst sites. The interactions prevent metal-species from aggregating and forming unwanted large particles that could yield graphitic particles or defective multi-walled tube structures. High surface area and large pore volume of the catalyst support facilitate high-yield SWNT growth due to the high density of catalyst sites made possible by the former and rapid diffusion and efficient supply of carbon feedstock to the catalytic sites by the latter [22].

There are two general growth modes of nanotubes in the CVD method, one of which is the bottom growth, and the other is the tip growth mode [28]. Both mechanisms are shown in Figure 2.4. The only difference between the two is whether the tube grows underneath or above the catalyst. The interaction between the catalyst and the support material can be characterized by the contact angle. When the interaction between the

catalyst and the support material is weak, tip growth is favored. On the other hand, for strong interaction, bottom growth is favored. In the bottom growth case, catalyst nanoparticles are anchored to the support material while in the tip growth process, the carbon diffuses through the catalyst particle and growth occurs beneath the metal particle. The catalyst is then pushed upward by the growing nanotube.

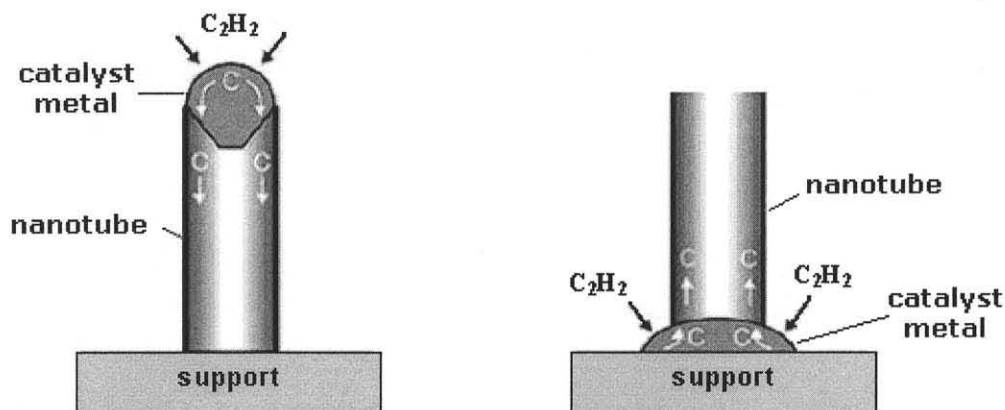


Figure 2.4 Carbon nanotube growth models for: (left) tip growth, (right) bottom growth [28].

Different carbon precursors, catalysts, and energy sources have been studied for the growth of SWNTs [29-34]. Smalley and coworkers have developed a gas phase catalytic process to grow bulk quantities of SWNTs [29]. The carbon feedstock is carbon monoxide (CO) and the growth temperature is in the range of 800-1200°C. Catalytic particles for SWNT growth are generated *in-situ* by thermal decomposition of $\text{Fe}(\text{CO})_5$. CO is very stable and it does not produce unwanted amorphous carbonaceous material at high temperature. To enhance the disproportionation of the CO carbon feedstock to carbon and thus enhance the growth of SWNTs, high pressures of CO (up to 10 atm) have been used. This CVD process is usually referred to as the high pressure CO (HiPCO) process. The SWNTs produced by this method have an average diameter about 1.1 nm. Diameters down to 0.7 nm are also observed.

Ordered and aligned growth of SWNTs by the CVD method has been reported [33,35,36]. Ordered growth involves contact printing for transfer of catalyst to lithographically patterned silicon pillars used for support. Suspended SWNTs were then self-assembled in the orientation directed by the pattern of the pillars (Figure 2.5a)

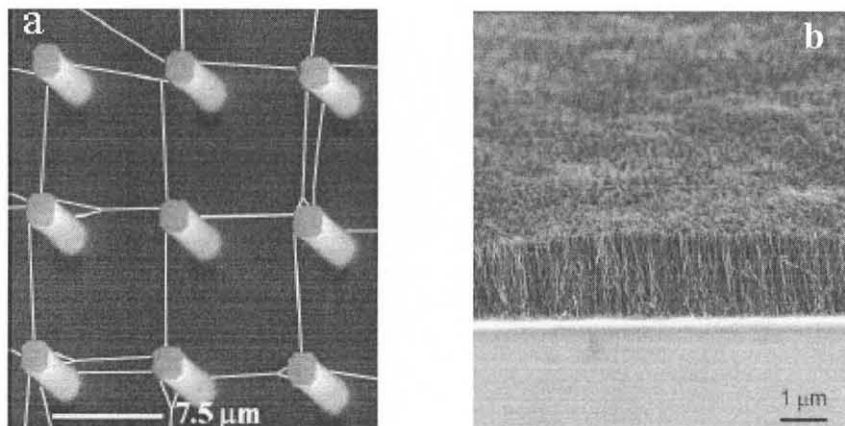


Figure 2.5 SEM images of (a) suspended SWNTs on patterned silicon support [36]; (b) aligned SWNTs on a quartz substrate [33].

The aligned growth method involves dip-coating of catalyst and catalyst promoter precursors (Co and Mo acetates in alcohol solution) on quartz substrates. Forest-like growth of SWNTs was obtained due to the extremely close packing of catalyst particles on the substrate (Figure 2.5b).

In summary, CVD methods are extremely promising for producing large quantities of high quality nanotubes on a large scale. Controlling nanotube growth with CVD strategies has led to organized SWNT nanowires that can be readily integrated into addressable structures useful for fundamental characterization and potential applications involving electronic, chemical, and electrochemical nano-devices [22].

2.2 Functionalization of Single Wall Carbon Nanotubes

Functionalized carbon nanotubes offer enormous potential as components of nanoscale electronics and sensors. The prospect of these applications has led to many successful functionalizations of SWNTs and MWNTs. These functionalizations may be separated into two categories: a non-covalent wrapping or adsorption and covalent tethering. Both of them will be discussed briefly in the following sections.

2.2.1 Non-covalent Wrapping or Adsorption

Aromatic compounds are known to interact strongly with the graphitic sidewalls of SWNTs through π - π stacking [37]. These interactions certainly increase the solubility of SWNTs in some aromatic solvents, and in the solution of aromatic surfactants [38, 39]. Many polynuclear aromatic compounds, such as anthracene, pyrene, and phthalocyanine derivatives have been used for immobilization of chemical or biological molecules on SWNTs [40-42].

In 2001, Smalley and his coworkers managed to wrap water-soluble linear polymers around SWNTs. This technique resulted in the solubility of SWNTs in water in the gram/liter range, allowing for the first time the manipulation of SWNTs by solution phase techniques like chromatography and electrophoresis, and simplifying their use as chemical agents [43]. A schematic image of a polyvinylpyrrolidone (PVP) wrapped SWNT is shown in Figure 2.6a.

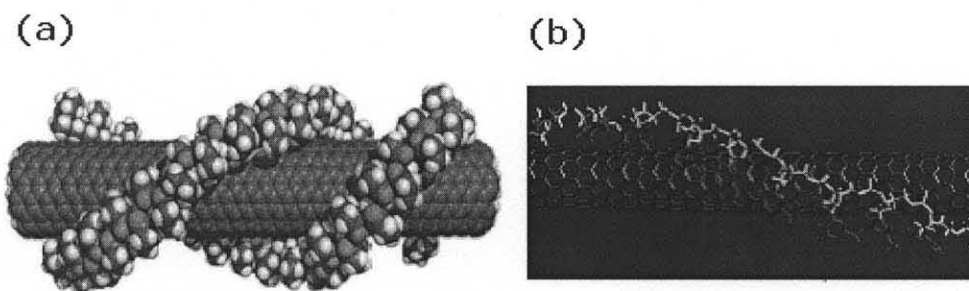


Figure 2.6 Non-covalent functionalization of SWNTs: (a) a possible wrapping arrangement of PVP on a SWNT [43]; (b) one possible binding structure of DNA wrapped SWNT [44].

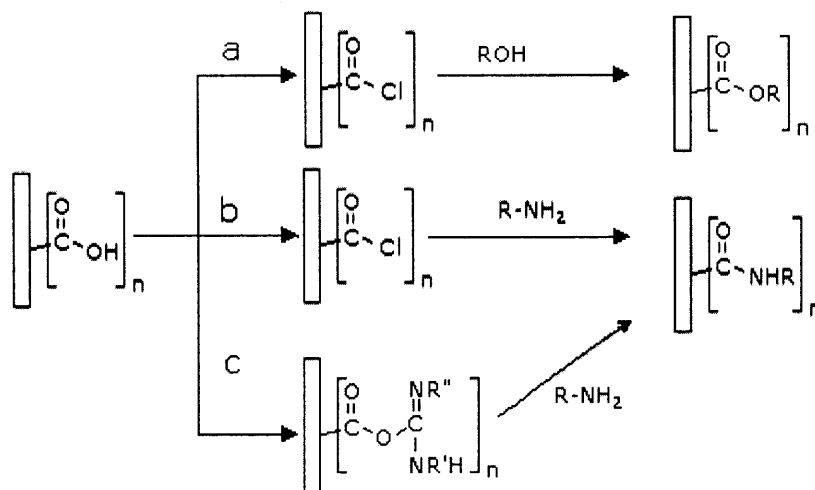
In addition to polymer wrapping, single stranded deoxyribonucleic acid (DNA) was found to more efficiently wrap and disperse SWNTs in water. A computer model image of DNA wrapped SWNTs is shown in Figure 2.6(b) [44]. More importantly, separation of SWNTs according to their electronic properties was achieved by DNA wrapping. DNA wrapped metallic SWNTs were found to have less surface charge than the DNA wrapped semiconducting SWNTs [44]. It is therefore possible to separate semiconducting from metallic SWNTs by this method.

Non-covalent functionalization of SWNTs by different polymers or by DNA will provide many simple methods to manipulate SWNTs in aqueous solution. Moreover, the non-covalent functionalization of SWNTs will leave the SWNT structure intact.

2.2.2 Functionalization of SWNTs involving Covalent Bonding

Covalent tethering, where the functional group is chemically bonded to the SWNT sidewall, offers stronger interaction between SWNTs and different functionalities. Many successful functionalizations of SWNTs and MWNTs have been reported [45-52]. Few common methods for the functionalizations of SWNTs will be briefly reviewed and discussed below.

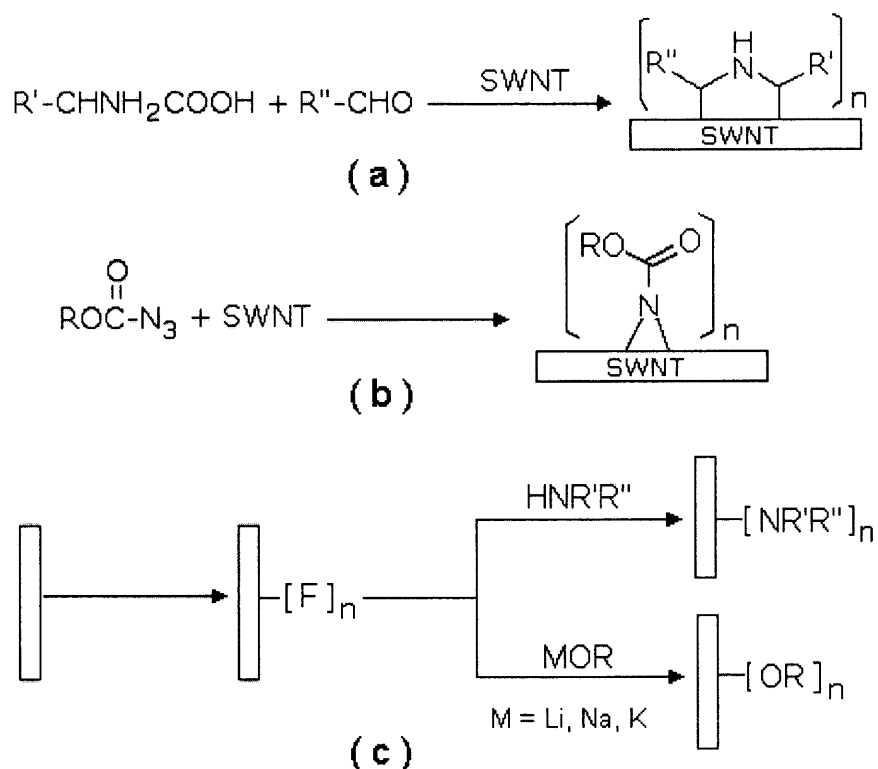
Amidation (formation of $-RHN-C=O$) and esterification (formation of $-O=C-OR$) of the carboxylic acid groups ($-COOH$) is the most widely used approach for the functionalization of SWNTs (Scheme 2.1). Various functional groups and molecules have been successfully attached to the nanotubes using this method [49,53,54].



Scheme 2.1 Reaction illustration of (a) esterification; (b) acyl chlorination and amidation; (c) diimide-activated amidation.

Before the attachment of the functional groups, SWNTs are generally refluxed in nitric acid solution or sonicated in a mixture of concentrated H_2SO_4 and HNO_3 to generate carboxylic acid groups ($COOH$). Then, the nanotubes grafted with $COOH$ groups are used for esterification or amidation with different reagents. The whole procedure is simple, but usually it takes few days to complete the reaction.

Direct sidewall tethering (Scheme 2.2) is another common approach used for carbon nanotubes functionalization. This method includes cycloaddition and fluorination. The fluorinated nanotubes can be subsequently derivatized.



Scheme 2.2 Cycloaddition functionalization of SWNTs: (a) five member ring formation by 1,3-dipolar cycloaddition; (b) three member ring formation via nitrene; (c) fluorination and derivatization of fluorinated SWNTs.

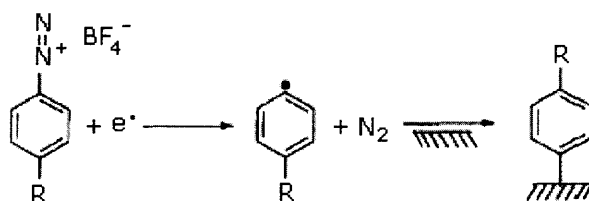
Cycloaddition to form five member or three member rings have been successfully carried out for the functionalization of SWNTs [55-57]. Prato and coworkers first reported the 1,3-dipolar cycloaddition (Scheme 2.2a) functionalization of SWNTs [55]. SWNTs functionalized by this approach are highly bundled (about 10-fold greater than in the starting material) and the method is straightforward. However, it took five days to complete the reaction.

Functionalization of SWNTs via the addition of nitrenes is also effective (Scheme 2.2b), and a variety of functional groups, such as alkyl chains, aromatic groups, dendrimers, crown ethers, and oligoethylene have been attached to the nanotubes [57]. For this technique, the generation of chlorocarbonates was needed, and subsequently,

azidocarbonates were synthesized. The whole procedure for this approach was not difficult, but many days of reaction time were still needed to achieve the functionalization of SWNTs.

Smalley and coworkers first reported the fluorination of SWNTs in 1998 [58], since then, many reports of the derivatization of fluorinated SWNTs have been reported [59-61]. The reaction is shown as Scheme 2.2(c). Fluorination is normally carried out between 150° to 600°C. The saturation stoichiometry of C₂F can be reached without destroying the nanotube structure [59]. Then the fluorinated SWNTs were refluxed with amine or sonicated with the alkanol salts to derivatize the SWNTs [60,61].

Electrochemical reactions are sometimes preferred because of their relative simplicity and because large quantities of organic solvents are not needed. SWNTs have been successfully derivatized via electrochemical reduction of a variety of aryl diazonium salts [48]. The reaction (Scheme 2.3) is shown below.



Scheme 2.3 Electrochemical functionalization of SWNTs [48].

For this reaction, a self-assembled SWNT nanopaper sheet or membrane was used as the working electrode. In the presence of the diazonium salt, the derivatization was accomplished in one step.

2.3 Applications of Single Wall Carbon Nanotubes

Carbon nanotubes have attracted the attention of many scientists world-wide. The molecular-scale dimensions and remarkable electronic, thermal and mechanical properties make them a unique material with a wide variety of potential applications. A few important applications are discussed below.

2.3.1 Potential Applications of SWNTs in Micro- and Nano-electronics

The uniqueness of the carbon nanotubes (CNTs) arises from their one dimensional structure discussed earlier. The helicity, along with the diameter (which determines the size of repeating structural unit) introduces significant changes in their electronic density of states, and hence provides unique one-dimensional characteristics to the electronic properties [62]. These novel electronic properties create the potential of applying carbon nanotubes for a range of fascinating electronic device applications.

One such application area is field emission, which is a quantum effect. It is an attractive source for electrons compared to thermo-ionic emission. When subject to a sufficiently high electric field, electrons near the Fermi level can overcome the energy barrier to escape to the vacuum level. The emission current from a metal surface is determined by the Fowler-Nordheim equation:

$$I = aV^2 \exp(-b\phi^{3/2}/\beta V) \quad (2.1)$$

where the I , V , ϕ and β are the current, applied voltage, work function, and field enhancement factor, respectively [62]. For technological applications, such as flat panel displays and electron guns, electron emissive materials should have low threshold emission fields and should be stable at high current density (for displays, a current density of 1-10 mA/cm² is required [63].) In order to minimize the electron emission

threshold field, it is desirable to have emitters with a low work function and a large field enhancement factor, which depends mostly on the geometry of the emitter and can be approximated as: $\beta = 1/5r$ where r is the radius of the emitter tip [62].

Carbon nanotubes have the right combination of properties – nanometer-size diameter, structural integrity, high electrical conductivity, and chemical stability for making good electron emitters. Electron field emission from CNTs was first demonstrated in 1995 [64], and since then intensive studies have been carried out on the electron emission properties of different types of carbon nanotubes. Compared to conventional emitters, CNTs exhibit a lower threshold electric field (1-3 V/ μm). The low threshold field for electron emission observed in carbon nanotubes is a direct result of the large field enhancement factor rather than a reduced electron work function [62]. Stable emission above 20mA/cm² has been demonstrated in SWNT films deposited on Si substrates, also, a current density above 4A/cm² (measured by a 1 mm local probe) was obtained from SWNTs produced by the laser ablation method [65]. The current densities observed above from the CNTs are significantly higher than from conventional emitters. Prototype matrix-addressable diode flat panel displays have been fabricated using carbon nanotubes as the electron emission source [66].

In summary, carbon nanotube emitters show clear advantages in properties over conventional emitters in terms of the threshold electrical field and current density, and therefore have high potential for use in display devices.

2.3.2 Hydrogen storage

Hydrogen has the highest energy content per unit weight of any known fuel as shown in Table 1 [67]. It is therefore considered to be a clean, alternative energy source. Interest in hydrogen as a fuel has grown dramatically since 1990, and many advances in hydrogen production and utilization technologies have been made [68].

Table 2.1 Energy Densities of Various Fuels [67].

Fuel	Energy Density [MJ Kg ⁻¹]
Hydrogen	141.90
Methane	55.50
Ethane	51.92
Propane	50.39
Gasoline	47.27
Natural Gas	47.21
Kerosene	46.00
Crude Oil	45.55
Benzene	42.29
Coal	31.38
Ethanol	29.70
Methanol	22.69
Ammonia	20.54
Wood	17.12

The safe storage of hydrogen is critical to hydrogen/air fuel cells or hydrogen driven combustion engines in vehicles. Today, compressed or liquefied hydrogen is used in most cases. However, this is disadvantageous for safety reasons and the liquefying process is very energy consuming. Hydrogen can be stored reversibly in metals hydrides. However, there are issues of weight and costs for transportation for compressed or liquefied hydrogen[68]. Extensive efforts have therefore been made to find new hydrogen storage materials. The cylindrical and hollow shape, and nanometer scale diameter of nanotubes suggests that the empty space could be filled with liquid and gas through a

capillary effect. Dillon and coworkers first found that 5 to 10% hydrogen can be stored in the bundles of SWNTs in 1997 [69]. Since then, a large number of studies of hydrogen storage in SWNTs were carried out using different methods (mainly by high pressure or electrochemical methods) [68-76]. However, conflicting results were reported: Nützenadel and coworkers found out that only 0.39 wt% of hydrogen can be stored reversibly in 0.7 to 1.2 nm SWNTs [70]; Lee et al. predicted that up to 16.7 wt% hydrogen can be inserted in (10,10) SWNTs [71]; Ye et al. reported that about 8% of H₂ adsorption can be obtained by high pressure at 80 K [72]. An even higher hydrogen uptake, up to 14-20 wt%, at 20^o-400^oC under ambient pressure was reported in alkali-metal intercalated carbon nanotubes [73] – this result has been later shown to be associated with the exposure of the samples to air.

High and reversible adsorption values were reported for single walled carbon nanotubes and graphite nanofibers in the literature. However, many of these results have not been independently confirmed as discussed below. The following table summarizes the values obtained by various groups.

Table 2.2 Hydrogen Sorption Characteristics for Different Carbon Nanomaterials. GNF = Graphite Nanofibers [77].

Material	Maximum Capacity		
	(wt%)	T (K)	P(Mpa)
SWNT	8.25	80	7.18
SWNT	5 – 10	133	0.04
SWNT	4.2	300	10 – 12
SWNT	6.5 – 7	300	0.1
SWNT	1.1 – 5.2	293	10
SWNT	3.5	300	5 – 10
GNF	11-67	300	11
GNF	0.4	298	0.1
GNF	10 -12	373	11
GNF	2.5	300	5 – 10
Li-GNF	20	473	0.1
K-GNF	14	473	0.1
GNF	10	300	12
GNF	15	300	15

Correlation between storage capacity and specific surface area for carbon materials including CNTs has been reported. The surface area was measured using the Braunner-Emmet-Teller (BET) method. A linear relationship with a storage capacity of 1.5 wt% at 1000 m²/g specific surface area was found [78], as shown in Figure 2.7. It was also reported that at low temperatures, a higher hydrogen storage capacity was achieved [79]. The curvature of the surface of SWNTs increases their reactivity with hydrogen, leading to higher storage capacities [78].

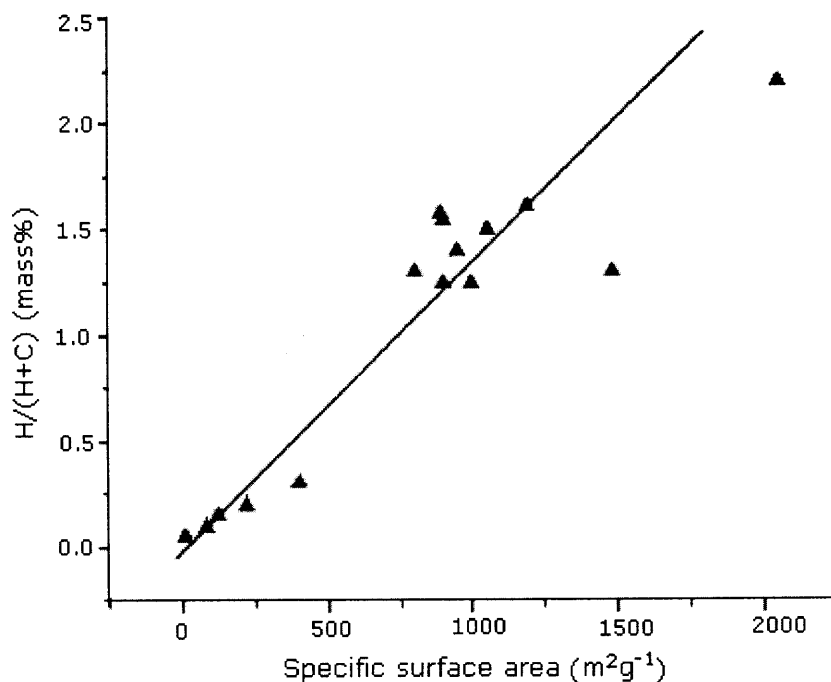


Figure 2.7 Reversibly stored hydrogen on various carbon materials versus the specific surface area [80]. Best-fit through the data points is indicated.

Although none of the promising experiments on hydrogen storage in SWNT could be reproduced independently, research on hydrogen storage in carbon nanotubes has remained active. Among the different materials for H₂ storage, SWNTs still appear to have the most potential. It is likely that reproducible hydrogen storage capacities in carbon nanotubes will be obtained after controlled tailoring and sidewall functionalization, and after a more detailed theoretical and experimental understanding of the adsorption process in these materials is achieved.

2.3.3 SWNT-filled Nanocomposites

The mechanical properties of SWNTs, such as their stiffness, elasticity, and high Young's modulus, make them ideal candidates for structural reinforcements in the fabrication of high strength, light-weight, and high performance ceramic, polymer and metal nanocomposites. Both theoretical and experimental works have confirmed that

CNTs are one of the stiffest structures ever made [62]. Theoretical studies have suggested that SWNTs could have a Young's Modulus as high as one TPa [81]. An increase in fracture toughness on the order of 25% has been seen in nano-crystalline alumina-nanotube composites [62]. Significant improvements in tensile strength and modulus also have been observed experimentally by other groups in SWNT-filled composites [82, 83].

There are certain advantages in mechanical properties that have already been realized by using CNTs for structural polymer and ceramic nanocomposites. It is therefore very likely that nanotube-filled composites will, in the short term, be used for structural applications. However, the full potential of CNTs in structural polymer composites will be achieved only with suitably functionalized nanotubes that can bind efficiently to polymer side groups.

CHAPTER 3

OVERVIEW OF RESEARCH CONDUCTED AND METHODOLOGIES USED

3.1 Synthesis of Single Wall Carbon Nanotubes (SWNTs) Using Chemical Vapor Deposition

A wide range of applications of SWNTs have been postulated, and for carrying out or evaluating these applications, large amounts of cost-effective SWNTs are needed. However, scaleable, cost-effective bulk synthesis as well as oriented growth of SWNTs still remain challenges and are therefore under active investigation world-wide.

In this research, both bulk and oriented synthesis of SWNTs have been carried out, but the focus has been on the synthesis of oriented SWNTs. The Chemical Vapor Deposition (CVD) method had been used for SWNT synthesis with different carbon sources, such as carbon monoxide (CO) and alcohol.

CVD offers a number of advantages over other growth techniques. First of all, the CVD system is simple to set up, and this method can be easily scaled up. Secondly, both high quality SWNTs and MWNTs can be synthesized using this method with a variety of choices for carbon precursors, such as methane, acetylene, carbon monoxide, alcohol, etc. Also, this method is capable of direct synthesis on desired substrates or within a matrix for *in-situ* fabrication of composites, and for making nanoelectronic devices with patterned catalysts. Additionally, the CVD approach can provide the opportunity for synthesizing nanotubes with controlled diameter using specifically-sized porous templates.

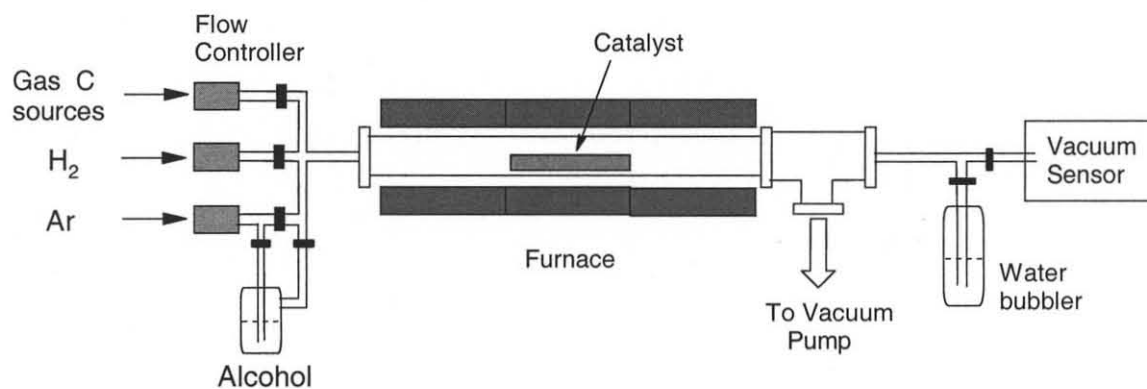


Figure 3.1 Schematic illustration of the CVD system used in this work.

The system, shown schematically in Figure 3.1, was used for nanotube synthesis. The furnace has three heating zones (which can be used for scaled up growth or *in-situ* catalyst processing), which are controlled independently by incorporated temperature controllers. Gas phase carbon precursors are directly introduced into the furnace and regulated through a gas flow meter, while liquid phase carbon precursors (such as alcohol) are transported by flowing Argon (Ar).

Bimetallic Co and Mo were always used as catalyst and promoter, respectively. For bulk growth, carbon monoxide (CO) was used as carbon source and magnesium oxide (MgO) was used as support. After synthesis pure SWNTs were obtained after removing MgO and the catalyst/promoter using acid treatment. Vertically aligned SWNT films on silicon (Si) wafers coated with catalyst were also synthesized using the CVD method. The synthesis and applications of both the bulk and the oriented nanotubes will be discussed in the following chapter.

3.2 Functionalization of Single Wall Carbon Nanotubes

Many hurdles need to be overcome for various applications of SWNTs to be realized. For example, pristine SWNTs exist in bundles, and they are not soluble in aqueous or organic solvents. Pristine bundles bond weakly to various matrices, are non-uniformly distributed and in addition slippage occurs between the van der Waals bonded individual tubes. This results in the formation of composites with relatively poor mechanical properties. Moreover, pristine SWNTs are difficult to manipulate due to inter-tube van der Waals interactions and their insolubility in common solvents. Selective functionalization can overcome most of these obstacles. Depending on the conditions used, functionalized SWNTs can be rendered soluble either in water or organic solvents. This will lead to the easier processability of nanotubes, and functional groups on the SWNT sidewalls will improve their interfacial binding with composite-forming matrices. Furthermore, the functionalization process can result in debundled SWNTs, and for many applications as well as for studying the properties and testing, debundled individual nanotubes are needed. Additionally, functionalized nanotubes with peptides, proteins and enzymes are the key steps for biological and sensing applications of SWNTs.

3.2.1 Functionalization Approaches

In this research, SWNTs made in our group (using the CO-CVD technique) or bought from outside sources (usually from Carbon Nanotechnologies using the HiPCO method) have been functionalized with amines and enzymes through conventional heating and stirring. This was done by first treating SWNTs in acids for generating $-\text{COOH}$ groups, followed by acyl chlorination (with thionyl chloride) and amidation with different amines

and enzymes. Other than this conventional approach, SWNTs have been successfully nitrated electrochemically in a three-electrode electrochemical cell. Electrochemical reaction offers advantages over conventional approaches such as, simplicity and cleanness. However, most of the functionalizations carried out in this research were performed using microwave radiation. These include amidation, 1,3-dipolar cycloaddition, nitration and the *in-situ* fabrication of a nanotube/silicon carbide composite. The microwave reaction technique provides a rapid, efficient and environmentally friendly process.

As indicated in Figure 3.2, the microwave oven is connected to a pressure control system, which is also connected to a reaction vessel through a pressure sensing tube. Therefore, the pressure in the reaction vessel can be monitored and controlled during the reaction. The microwave system can be programmed with different pressure, power and time periods. Up to 200 psi pressure and 900 Watts of power can be used for a reaction. The Teflon liner of the reaction vessel can withstand temperatures up to 200°C.

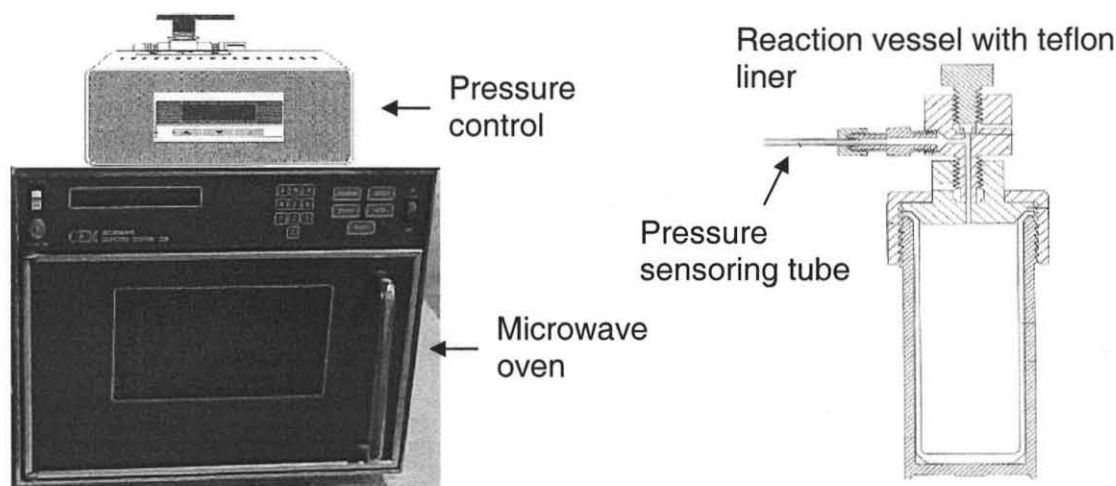


Figure 3.2 Photograph of the microwave system used in this research.

3.2.2 Basics of Microwave-Induced Chemistry

Microwave radiation has wavelengths between 0.01 and 1 meter, corresponding to frequencies between 30 and 0.3 GHz. Typically, the wavelength at which industrial and domestic microwave ovens intended for heating operates is regulated at 12.2 cm, corresponding to a frequency of 2.450 GHz [84]. As an alternative to conventional conductive heating, microwave irradiation is becoming an increasingly popular method for carrying out chemical reactions.

The irradiation/heating generated by microwaves is direct energy, which is absorbed solely and uniformly by the sample. Therefore, very little heat is wasted relative to conventional thermal methods. The direct heating means that lag-times in the heating regimes are very small. This is the main reason why microwave heating is fast and efficient. Two principal microwave heating mechanisms exist: The dipolar polarization mechanism and the conduction mechanism.

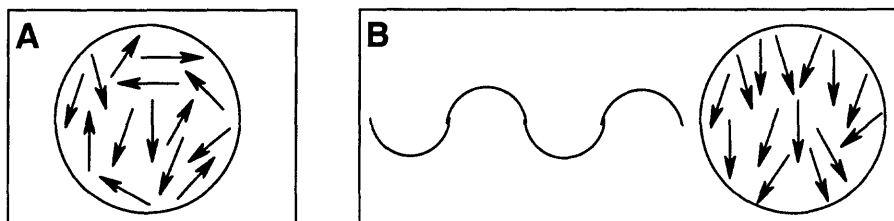


Figure 3.3 Schematic depiction of the dipolar polarization mechanism.

The dipolar polarization mechanism shown in Figure 3.3 is responsible for the majority of microwave heating effects observed in solvent systems. It refers to the alignment of molecules that have permanent or induced dipoles, with the electric field component of the radiation. In substances such as water, the different electronegativities of individual atoms results in the existence of a permanent electric dipole on the molecule

[85]. The dipole is sensitive to external electric fields, and will attempt to align itself with them by rotation. This alignment is rapid for a free molecule in the gas phase or in dilute solution. For instance, gas molecules are spaced far apart and their alignment with the applied field is much faster than molecules in pure liquids or in a solid, in which the instantaneous alignment is prohibited by the presence of other molecules. The ability of molecules in a liquid solution to align with the applied electric field varies with different frequencies and the viscosity of the liquid solvent [84]. Under low frequency irradiation, the dipole will rotate in-phase with the electric field. Some energy is gained by the molecule by this process and some is also lost in collisions, but the overall heating effect is small. Under the influence of a high frequency electric field, on the other hand, the dipoles do not have sufficient time to respond to the field, and so do not rotate. Since no motion is induced in the molecules, no energy transfer takes place, and therefore no heating occurs [85].

The microwave radiation frequency region is in between these two extremes. The frequency of the applied microwave irradiation is low enough so that the molecules have time to respond to the alternating electric field and therefore rotate. Alternatively, the frequency is not high enough for the rotation to precisely follow the field. As the dipole reorientates to align with the electric field, the field is already changing and a phase difference exists between the reorientation of the field and that of the dipole. This phase difference causes energy to be lost from the dipole by molecular friction and collisions, giving rise to the dielectric heating [84].

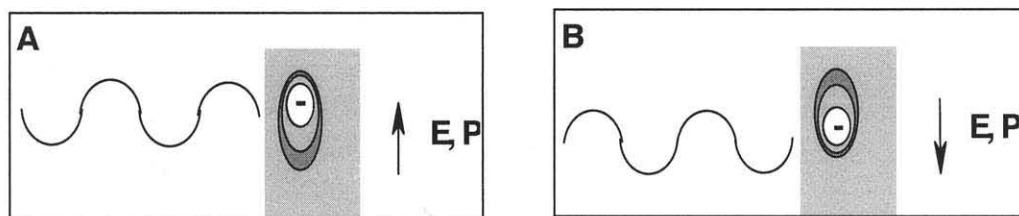


Figure 3.4 Schematic depiction of the conduction mechanism.

The conduction mechanism (Figure 3.4) is involved when an electrical conductor is irradiated with microwave radiation. The charge carriers (electrons or ions) move through the material under the influence of the electric field, resulting in a polarization. The induced currents will cause heating in the sample due to the electrical resistance of the sample being irradiated. The conduction mechanism is associated with a much stronger interaction than the dipolar mechanism with regard to heat-generating capacity. If the sample is a metal and is strongly conducting, most of the microwave energy does not penetrate the surface of the material and is reflected. Colossal surface voltages are produced in conducting sample resulting in arcing that is observed from the metals under microwave radiation [86].

3.3 Applications of Single Wall Carbon Nanotubes

As pointed out earlier, SWNTs have the potential of being utilized for hydrogen storage and as electrodes in conventional proton exchange membrane (PEM)- and bio-fuel cells, and as reinforcing fillers in ceramic and polymer composites.

For hydrogen storage, self-assembled sheets of pristine and modified SWNTs were used in this research as the working electrode for electrochemical hydrogen adsorption/storage in a three-electrode cell in 6M aqueous KOH or HNO₃ solution.

Hydrogen adsorption studies on pristine SWNTs, as well as SWNTs functionalized with electrodeposited nanoparticles of magnesium (Mg) and cobalt (Co) as well as electrochemically grown nitrogen-containing conducting polymer, PANi (polyaniline), have been performed. The metals and PANi can function as catalytic centers for hydrogen adsorption. Up to approximately 3 wt% of weakly chemisorbed hydrogen (uncorrected for possible water uptake via nanocapillarity) was measured from both pristine and modified SWNT samples, as will be discussed in Chapter 6..

Vertically oriented SWNTs were functionalized with enzymes and used for biofuel cells and inversely for biosensor applications. Glucose oxidase was used for this study. It was first attached to the tips of the oriented nanotubes by an electrochemically-induced reaction. Then, the functionalized nanotubes used as electrode was tested in glucose solution as a biofuel cell and biosensor. More details will be provided in Chapter 6.

Single wall carbon nanotube and silicon carbide (SWNT-SiC) ceramic nanocomposite has been synthesized using microwaves. The synthesis temperature used is much lower than in other methods reported in the literature. Our new method could prevent SWNTs from being damaged since the processing temperature is much lower than the high sintering temperatures used by other groups to prepare ceramic-nanotube composites. *In-situ* polymerized polymethyl methacrylate, (PMMA)-SWNT nanocomposite was also synthesized in supercritical carbon dioxide. Very uniform attachment/coating of the PMMA onto SWNTs was obtained.

3.4 Characterization

Various characterization techniques have been used in this research. For example, for pristine or as-prepared SWNTs, Raman spectroscopy, scanning electron microscopy (SEM) and transmission electron microscopy (TEM), were typically used for their characterization. Micro-Raman experiments were carried out using a Horiba/Jobin Yvon LabRaman system with a scanning stage attachment, cooled CCD (charge coupled device) detection and 632.8 nm excitation. Micro-Raman data reported were always checked at various regions of the sample. The TEM images were recorded using a TOPCON 200kV Ultra-High Resolution Transmission Electron Microscope or LEO 922 Omega[®] EF-TEM. SEM imaging was carried out using a LEO 1530 instrument.

After functionalization with different chemical groups, SWNTs were also analyzed using transmission fourier transform infrared (FTIR) spectroscopy, attenuated total reflectance-FTIR (ATR-FTIR), nuclear magnetic resonance (NMR), ultraviolet-visible-near infrared (UV-Vis-near IR) spectroscopy, energy dispersion X-ray (EDX), thin film X-ray diffraction (XRD) and differential thermal calorimetry (DSC). The FTIR measurements were performed using a Perkin Elmer instrument, and the ATR-FTIR was carried out using a Thermo Electric Corp. Nicolet Model 470 spectrometer. The accessory attachment used was a PIKE Technologies Single Reflection HATR instrument. The UV-vis-NIR spectra were obtained using a Hewlett Packard, Model 8453 UV-Visible spectrophotometer. Proton nuclear magnetic resonance (NMR) data were acquired with a Varian INOVA 500 MHz NMR Spectrometer. Measurements of energy dispersion X-ray (EDX) were carried out using a LEO 1530 instrument. Thin film X-ray

diffraction (XRD) was done on Philips X'Pert MRD instrument equipped with an Eulerian Cradle, and with a Cu point source and Ni filter.

For hydrogen uptake characterization a sample was carefully measured using the Prompt Gamma technique with the neutron source at the National Institute of Standards and Technology (NIST); most other samples were characterized by thermogravimetric analysis (TGA). For electrochemical nitration, the TGA was performed with a Universal V3.7A instrument and differential thermal analysis (DTA) combined with TGA was carried out with a Perkin Elmer Pyris Diamond TGA/DTA instrument. Cyclic voltammograms were measured using computer-controlled Princeton Applied Research and Elchema potentiostat-galvanostat instruments. The performance of biofuel cells fabricated was tested using a computerized fuel cell testing stand (GlobeTech, Inc. GT120). Vickers hardness measurements were conducted on nanocomposites synthesized using a LECO micro-hardness tester (LM 700, LECO Corp.).

CHAPTER 4

SYNTHESIS OF SINGLE WALL CARBON NANOTUBES

4.1 Introduction

Both bulk and oriented synthesis of SWNTs have been carried out, but most of the effort has been devoted to oriented synthesis, since oriented (or patterned) SWNT arrays are needed for devices, such as sensors, transistors and micro fuel cells. Oriented growth of SWNTs is a challenging task and has been successfully achieved by only one other group [87]. In this work we have optimized and improved the oriented growth process. The bulk synthesis technique is necessary for obtaining large quantities of pure SWNTs for various large-scale nanocomposite and nanowire applications, and is the focus of research by other members of the group. In order to achieve scaled up growth it is necessary to obtain insights into the growth mechanism and determine the important growth parameters.

Uniform and proper nanometer size of the catalyst particles, along with their dense distribution on smooth surfaces is critical for the vertically oriented growth of SWNTs [87-90]. Two catalyst deposition approaches were employed for the aligned synthesis of SWNTs. These include dip-coating and spin-coating. Dip-coating involves dipping the substrate into the catalyst suspension in chloroform and the subsequent pulling out of the substrate. For spin-coating, a drop of catalyst and polyvinylpyrrolidone (PVP) solution mixture was spin coated onto the substrate. Vertically oriented SWNTs were obtained from both catalyst deposition methods, but much better vertical alignment of SWNTs has been achieved from a polymer (poly-vinyl pyrrolidone, PVP) chelated catalyst precursor. In this approach, uniform size and dense distribution of catalyst

particles on a silicon wafer were obtained upon burning and removing the polymer from the spin coated catalyst precursor.

Magnesium oxide (MgO) was used as support for metallic cobalt (Co) catalyst and molybdenum (Mo) promoter for bulk synthesis. Clean SWNTs were obtained after the removal of the catalysts and MgO support using dilute acid treatment.

4.2 Experimental Section

Bimetallic cobalt (Co): molybdenum (Mo) with 1:1 weight ratio or 1.6 :1 in atomic weight ratio was used as catalyst/promoter for the oriented growth of SWNTs. The catalyst/promoter precursor acetates were deposited by dip or spin coating techniques. The dip-coating solution was prepared by suspending and sonicating a mixture of Co and Mo acetates in chloroform containing 0.02 wt% of metals to total solution. The dip coating process involved immersing a silicon wafer in the mixture and slowly pulling it out after 5 to 10 minutes. The spin-coating precursor was prepared using 0.05 wt% of each metal to total solution with 1 wt% of polyvinyl pyrrolidone (PVP) in 90% ethanol. To prepare the catalyst/promoter precursor solution, cobalt nitrate and ammonium heptamolybdate were first dissolved in water. PVP was then added and dissolved in the clear cobalt and molybdate salt solution. After that, nine times of ethanol to water in volume ratio was added to the solution. The solution obtained was then spin-coated onto a Si wafer at a spinning speed of 3000 rpm. After removing the PVP polymer by heating in air to 800°C at a heating rate of 5°C/min. and holding at 800°C for 2 hours, the catalyst/promoter-coated substrate was ready for SWNT growth.

The same SWNT growth conditions were employed for both dip- and spin-coated catalyst/promoter precursors. Specifically, the CVD system (open to air) was brought to 800 °C and then maintained at 800°C for 30 minutes under flowing of hydrogen (100 sccm flow rate at 1 atm.). At the same temperature, SWNT growth was carried out for 20 minutes using ethanol, transported by argon (300 sccm flow rate at 1 atm.), as the carbon source.

The bimetallic Co and Mo catalyst/promoter system supported on MgO was also employed for bulk synthesis of SWNTs. The catalyst/promoter to MgO support was optimized at the atomic ratio of 0.016Mo: 0.004Co: 0.98%MgO. For preparing the catalyst, ammonium heptamolybdate tetrahydrate, cobalt nitrate, magnesium nitrate together with citric acid (30 to 40% to the weight of magnesium nitrate) were dissolved in distilled water. Then, the solution was placed in a quartz boat and covered with aluminum foil, and introduced to a pre-heated furnace at 550 °C and kept there for about 5 minutes. After cooling, the resulting solid was ground into an uniform powder and used as the catalyst/promoter precursor for nanotube synthesis. For making bulk carbon nanotubes, a small amount of the catalyst/promoter precursor powder was placed in a quartz boat covered by a sheet of carbon paper, and the boat was placed in a quartz tube in a horizontal furnace. The furnace was brought to 700°C under flowing hydrogen and held at that temperature for 30 minutes to reduce the catalyst/promoter precursor oxides to metals. After the reduction process, the carbon source, carbon monoxide (CO), was introduced to replace the hydrogen for SWNT synthesis at the same temperature. The synthesis process was carried out for 15 minutes before the system was cooled down

under flowing argon. The catalyst/promoter and MgO from the product were removed using 4M hydrochloric acid by repeated dissolution and filtration (2 to 3 cycles).

All chemicals used for the experiments were purchased from Sigma Aldrich. Carbon monoxide was bought from Spectra Gases Inc (research grade). The SWNTs synthesized by both methods were characterized using TEM, SEM and micro-Raman spectroscopy.

4.3 Results and Discussion

Carbon nanotubes obtained using bulk synthesis showed similar features for each batch. The promoter and catalyst (Mo and Co) and support (MgO) were easily removed by dilute acid treatment. The SEM images in Figure 4.1a obtained from purified SWNTs showed nanotube bundles that were many micrometers in length. Typical micro-Raman spectra (Figure 4.1b) indicated from the low frequency radial breathing mode (RBM) frequencies that the individual nanotube diameters ranged from 0.7 to 1.2 nm as calculated using Equations 1.1 and 1.2 in Chapter 1.

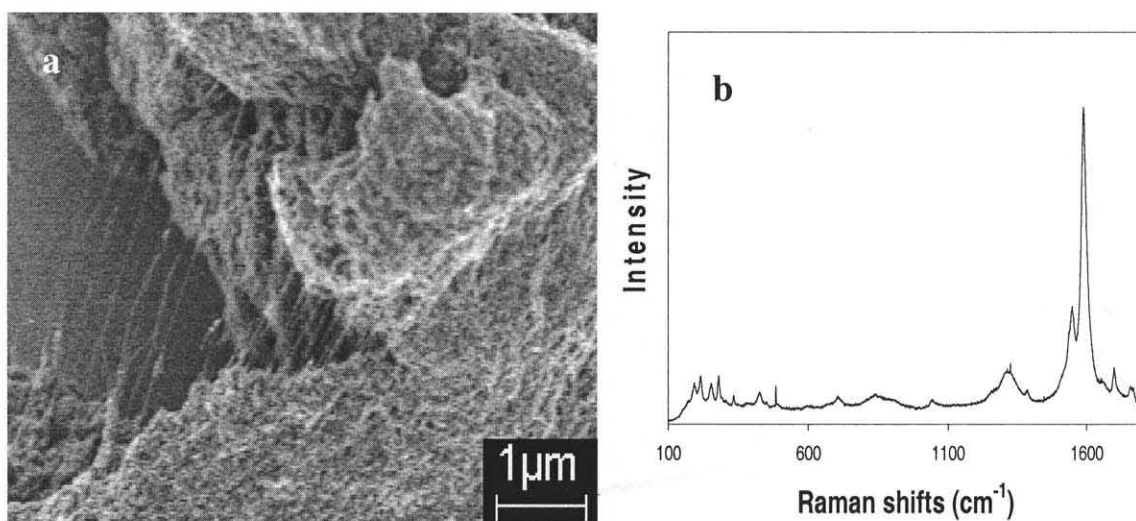


Figure 4.1 Purified SWNTs obtained from bulk synthesis: (a) SEM image and (b) Raman spectrum excited with 632.8 nm laser radiation.

For oriented synthesis ethanol was chosen as the carbon source due to the fact that the OH radicals formed on decomposition etches away amorphous carbon and thus reduces the formation of disordered carbon on the nanotube sidewalls and on the catalyst support [91]. 0.02 wt% each of Co and Mo in chloroform was found to be the best dip-coating catalyst/promoter precursor composition for the growth of vertically oriented SWNTs. Figure 4.2 shows a typical SEM image of the oriented SWNTs obtained from the dip-coating method. The top half of the image on the right is a tilted cross-sectional view from the edge of a film, which shows the vertical alignment of the SWNTs. The bottom half of the image is from the top of the aligned SWNTs. The inset on the left of the figure is a magnified image of the aligned SWNTs.

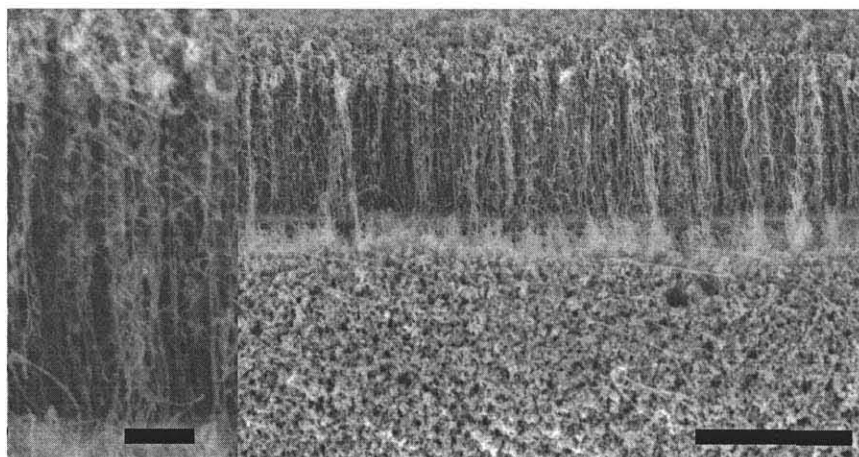


Figure 4.2 (Right – top half) SEM image from the edge of vertically aligned SWNT film on silicon obtained using the dip-coating method for depositing the catalyst/promoter precursors. (Right – bottom half) SEM image from the top of the SWNT film. Scale bar for both images = 2 μm . (Inset – left) Magnified image of the aligned nanotubes. Scale bar = 200 nm.

A high degree of vertical orientation of SWNTs on Si was obtained with 0.05 wt% each of Mo and Co together with 1 wt% of polyvinyl pyrrolidone (PVP) in 90% ethanol of catalyst/promoter precursors. Figure 4.3a shows a tilted view SEM image of

the vertically aligned SWNTs grown using this catalyst/promoter precursor. The image in Figure 4.3b taken directly from the top of the aligned nanotubes shows densely packed SWNTs. A higher magnification SEM image of the aligned SWNTs is shown in Figure 4.3c. A typical TEM image (Figure 4.3d) clearly shows that a large fraction of the aligned SWNTs formed are individual tubes rather than bundles of SWNTs that have been typically observed in previous work [87-90]. Moreover, very little amorphous carbon and double-wall or multiwall carbon nanotubes were found.

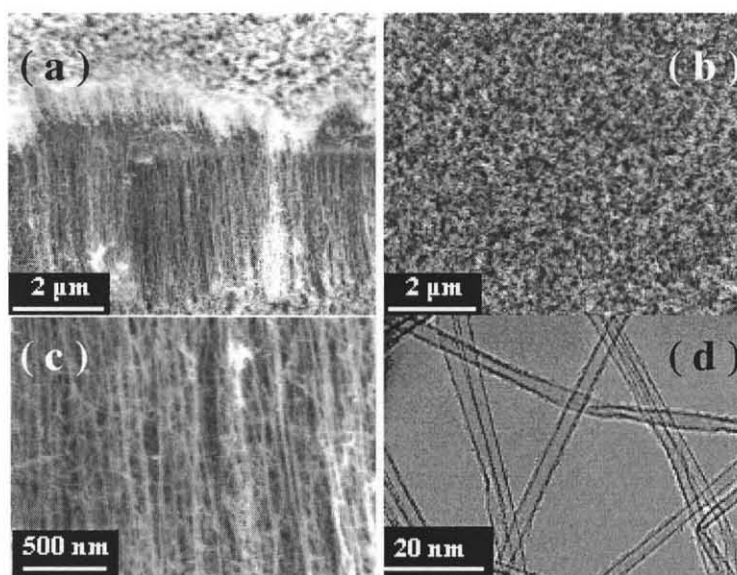


Figure 4.3 Vertically aligned SWNTs on Si obtained from polyvinyl pyrrolidone (PVP) supported catalyst/promoter: (a) tilted view (about 30°) of the aligned SWNTs at an edge; (b) Top view of the vertically aligned SWNTs; (c) Magnified view of the aligned SWNTs shown in (a); and (d) TEM image taken from a sample of the aligned SWNTs.

Raman spectra taken from the aligned SWNT samples using 632.8nm excitation were found to be consistent with the formation of SWNTs using both of the two catalyst deposition methods. The radial breathing mode (RBM) spectrum (Figure 4.4a) indicates an average SWNT diameter of 1.3 nm based on Equation 1.1 (Chapter 1). The average diameter is consistent with the values obtained from the TEM images. The intensity of

the defect/disorder mode at 1323 cm^{-1} in the high frequency region of the Raman spectrum (Figure 4.4b), however, is relatively high. This is probably because the tube-ends are more exclusively sampled in the back-scattering geometry used in these measurements.

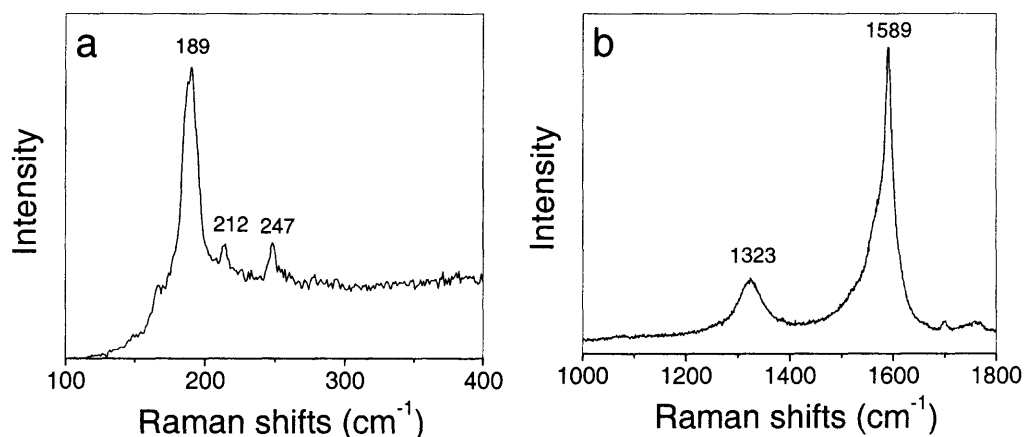


Figure 4.4 Raman spectra of the vertically aligned SWNTs in: (a) the radial breathing mode frequency region; and (b) the defect/disorder mode and carbon-carbon tangential mode frequency region.

Parameters, such as catalyst/promoter particle density, size, distribution and reactivity are very important for the formation of well-aligned, vertically grown SWNTs. Immobilization by the polymer PVP leads to uniform, nanometer size catalyst/promoter particles (Figure 4.5) which in turn results in more uniform SWNT alignment.

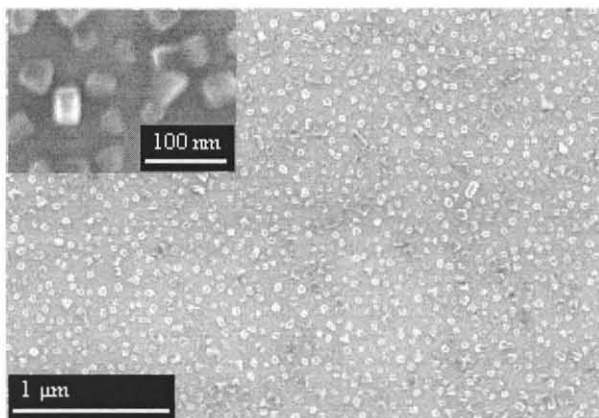


Figure 4.5 SEM image of catalyst/promoter particles obtained from the spin coating procedure discussed in the text, after burning away the PVP polymer. The inset is a magnified image of some of the particles.

As metal ion chelation reagents, polymers have been widely used in water purification for decades [92-94]. Here, PVP was chosen to form a complex with the catalyst/promoter metal ions because PVP is water-soluble and has multiple chelating sites, such as N, O and C=O. All the metal binding sites are available to form a complex with metal ions when PVP is in solution. For example, free electron pairs on the nitrogen atoms can bond with cations as well as oxygen atoms. Additionally, the C=O group can also bond to transition metal ions through π -complexation. Most likely the metal ions are bound to several different binding groups from the same PVP chain or from different chains, via inter- or intra-molecular complexation involving the so-called “bridge model” [92,95]. Our experimental data suggest that the binding capacity of PVP to Co and Mo cations is extremely strong. Specifically, 1 wt% of PVP can help dissolve 0.05 wt% of Co and Mo in their corresponding salts as mentioned above (the solution is a little milky but no precipitation is observed as shown in Figure 4.5B). As we mentioned in the experimental section, the Co and Mo salts were first dissolved in denionized (DI) water, and this was followed by the addition of polymer and then of ethanol. However, without

the addition of PVP, precipitates were immediately observed when ethanol was added to the Co and Mo precursor salt aqueous solution, as evident in Figure 4.5C. When the PVP content in the solution is increased, the solubility of the Co and Mo salts is also increased. The photograph in Figure 4.5A shows a clear solution of 2 wt% PVP with the same metal concentration as above.

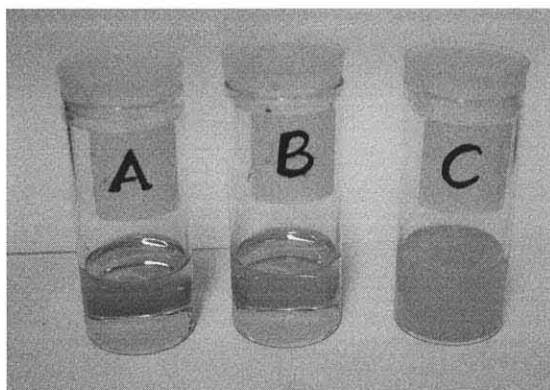


Figure 4.6 Photographs of: (A) clear solution of 2 wt% (or more) PVP and 0.05 wt% of Co and Mo metal content in 90% ethanol; (B) solution of 1 wt% PVP and same metal concentration as in (A); and (C) 0.05 wt % of Co and Mo in 90% ethanol with no PVP added.

PVP plays dual roles in our experiment. It first increases the solubility of the metal salts in solution, so higher concentrations of catalyst/promoter in solution can be obtained for the deposition of dense coatings, where vertical alignment of SWNTs occurs spontaneously. After spin coating, the catalyst precursor forms a smooth and continuous film, which is about 50 nm in thickness (film thicknesses increase with increasing amounts of PVP). PVP also functions as the medium for the separation and support of the catalyst/promoter particles in the coating so that uniform and extremely closely packed catalyst particles can be obtained after the removal of the polymer by burning in air. On the other hand, the amount of PVP in the solution has to be optimal. When it is more than the necessary amount, coarsening and agglomeration of the catalyst/promoter particles

occur during the burning process resulting in inhomogeneous growth of SWNTs as shown in Figure 4.6.

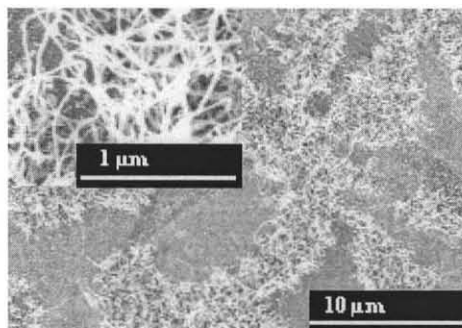


Figure 4.7 SEM image of unevenly distributed SWNTs synthesized from the 0.05wt% of Mo and Co and 2 wt% (or more) of PVP in 90% ethanol catalyst precursor. The inset is a representative magnified image of the SWNTs produced.

In summary, both bulk and oriented thin film growth of SWNTs by chemical vapor deposition (CVD) have been demonstrated, and are discussed in this chapter. The focus of this research however was in optimizing vertically oriented thin film growth of SWNTs on substrates, such as silicon and quartz. The understanding and optimization of vertically oriented growth is key to developing specific nanotube applications some of which will be discussed in Chapter 6.

CHAPTER 5

FUNCTIONALIZATION OF SINGLE WALL CARBON NANOTUBES

5.1 Introduction

As-prepared or pristine single wall carbon nanotubes (SWNTs) are difficult to study and use in applications because they exist in bundles from which it is difficult to separate the individual SWNTs. Pristine SWNTs are not soluble in any solvent, are chemically inert and have poor interfacial binding with other materials. This results in greatly limiting the applications of SWNTs. Functionalization can overcome many of these obstacles. With selected functional groups, the SWNTs can be rendered soluble either in water or in organic solvents. This will lead to easier processability of the nanotubes, and the functional groups will also improve their interfacial binding to other polymer, ceramic or metal matrices. Furthermore, the functionalization process can result in debundled SWNTs, which are needed for many applications as well as for studies of the fundamental properties of SWNTs. Additionally, nanotubes functionalized with biomolecules like enzymes provide SWNTs suitable for biological and biosensing applications.

Three approaches were used in this work for the functionalization of SWNTs. These include conventional heating, refluxing and stirring reaction techniques, electrochemically-induced reaction methods, and a newly developed microwave radiation assisted reaction approach. Enzymes and different amines have been attached to SWNTs using conventional chemical reaction techniques, and microwave radiation assisted amidation with amines, 1,3 dipolar cycloaddition with amino acids and aldehydes, and nitration of SWNTs have also been successfully carried out. Additionally,

electrochemical nitration of self-assembled nanotube sheets has also been carried out. These three functionalization approaches are separately presented and discussed below.

5.2 Functionalization of Single Wall Carbon Nanotubes with Amines and Enzymes

Successful functionalization of both single wall (SWNT) and multiple wall (MWNT) carbon nanotubes [43-51,96-101], including non-covalent wrapping or adsorption [43,44] and covalent tethering [46-51, 96-101], has been reported in the literature.

Functionalization of SWNTs with enzymes has been achieved by the initial acylation of SWNTs followed by amidation with the desired amine or enzyme. To the best of my knowledge this is the first report of functionalization involving bonding of the enzyme to the SWNT sidewall. The two-step relatively simple chemical method employs mild conditions and results in tethering of the organic functionality to the nanotube. The two enzymes tethered to the SWNTs were porcine pancrease lipase (PPL) and amino lipase (AK) [see Appendix A]. The same method was also employed to chemically functionalize SWNTs with various amines, which include three primary amines (*cis*-Myrtanlyamine, 2, 4-dinitroaniline, 2, 6 –dinitroaniline) and two secondary amines (N-decyl-2, 4, 6-trinitroaniline and N- (3-morpholinopropyl)-2, 4, 6-trinitroaniline).

Linkage of chiral molecules and enzymes to SWNTs opens up the potential for applications of carbon nanotubes in biological fields, and in biosensor or chemically modulated nanoelectronic devices. Tethering to nitrated molecules also opens up the possibility of using SWNTs as nanoscale energetic materials. In this study the chemical moieties on the sidewall of the carbon nanotubes were identified by attenuated total reflectance Fourier Transform-Infrared (ATR-FTIR), Raman and ultraviolet-visible (UV-

Vis) spectroscopy, whereas field-emission scanning electron microscope (FE-SEM) imaging provided insights into the morphology of the functional nanotubes obtained.

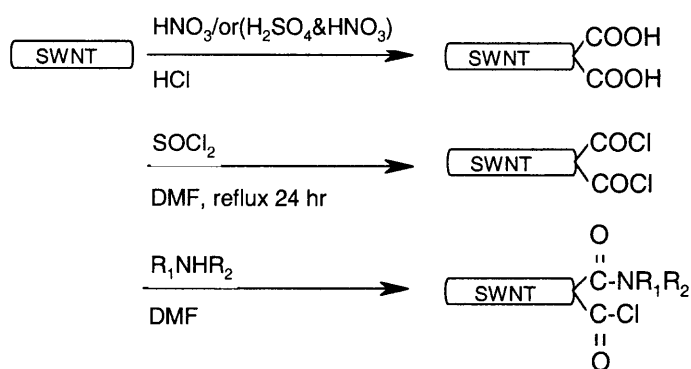
The SWNTs used were prepared either by high pressure, chemical vapor deposition, CVD (HiPCO, obtained from Carbon Nanotechnologies Inc) [102] or by the atmospheric pressure CO-CVD growth technique developed in our laboratory [103]. All other chemicals were purchased from Sigma-Aldrich. A general reaction sequence shown in Scheme 5.1 can be described as follows:

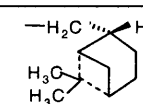
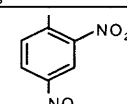
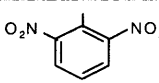
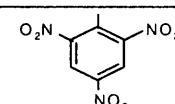
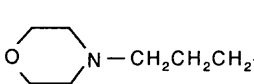
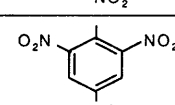
(1) *Carboxylation*: In a typical experiment pristine SWNTs were refluxed in 4 M HNO₃ for 24 hours and filtered through a 10-micrometer pore size PTFE filter paper. After filtration, the refluxed SWNTs were exposed to 1 M HCl and sonicated for half an hour to generate -COOH groups (identified by FTIR spectroscopy) on the sidewalls and tube-ends by a sequence of reactions that are not well-understood. Alternatively, pristine SWNT powder is sonicated in a 3:1 mixture of concentrated H₂SO₄ and HNO₃ at room temperature for 1 to 2 hours, followed by exposure to 1 M HCl and sonication in HCl solution for about 30 minutes to form carboxylated SWNTs. The functionalized SWNTs were then filtered, washed with deionized (DI) water and finally dried in air.

(2) *Acylation*: The carboxylated nanotubes (6~10 mg) were stirred in 15 ml of a 20:1 mixture of thionyl chloride and DMF (N, N-dimethyl formamide), at 70°C for 24 hours to form acyl chlorinated SWNTs. After the acyl chlorination, the SWNTs were filtered, washed with anhydrous THF, and dried under vacuum at room temperature for ~ 20 min.

(3) *Amidation*: SWNTs functionalized with acyl chloride groups were reacted with the desired amines (in 50 % excess) using DMF as solvent at 110°C. All reactions were carried out for 3 days. The excess amine was washed first with DMF, followed by

anhydrous tetrahydrofuran (THF) and the SWNTs were then separated by filtration. In the case of the enzyme PPL the reaction temperature was kept at 37°C, while the reaction with the enzyme AK was carried out at 50°C. Also, when DMF was employed as solvent, the reactions with the enzymes were continued for five days. The excess enzymes were washed away by extensive washing with dimethylformamide (DMF), phosphate buffer (pH 7.4) and deionized water and finally the product was dried overnight under vacuum.



Compound	R ₁	R ₂
cis-Myrtylamine	-H	
2, 4-dinitroaniline	-H	
2, 6-dinitroaniline	-H	
N-decyl-2, 4, 6-trinitroaniline	-CH ₂ (CH ₂) ₈ CH ₃	
N-(3morpholinopropyl)-2,4,6-trinitroaniline		
Porcine pancrease lipase (PPL)		
Amino lipase (AK)		

Scheme 5.1 Amines, nitroanilines and enzymes used to functionalize SWNTs. The exact functional groups of R₁ and R₂ for different functionalizations are listed in the table. For enzyme PPL and AK, the R₁ and R₂ groups have not been determined.

Figure 5.1 (a-e) shows the ATR-FTIR spectra of SWNTs grafted with the acyl chloride group and SWNTs functionalized with two amines and two enzymes, respectively shown in Scheme 5.1. ATR-FTIR was carried out using instrumentation described in Chapter 3 – Section 3.4. In spectrum (a), which is for SWNT-COCl, the peak at 1710 cm^{-1} is assigned to the C=O stretching vibration of the COCl group, while the broad peak at 1530 cm^{-1} can be assigned to the stretching of the nanotube C=C bond located near the COCl group. Spectra (b) and (c), show the infrared-active vibrational modes of SWNTs functionalized with *cis*-Myrtanlyamine and N-(3-morpholinopropyl)-2, 4, 6-trinitroiline, respectively. The C=O stretching frequencies of the amide bond formed by the functionalization reaction appear at 1650 cm^{-1} and 1640 cm^{-1} . Peaks at 2910 cm^{-1} , 2860 cm^{-1} and 2850 cm^{-1} can be clearly assigned to the C-H stretching vibrations of the attached amines. The line at 1430 cm^{-1} can be assigned to N-H or C-H deformation modes. Peaks at 1710 cm^{-1} in spectra (b) and (c) are due to the C=O stretching mode of unreacted carboxyl groups on the SWNTs.

Incomplete amidation is perhaps due to steric hindrance by the rigid ring structures of the R_2 groups on the amines shown in Scheme 1. A steric effect of the ring from the attached amine can partially shield the COCl group nearby from chemical attack. This is especially true for SWNTs functionalized by COCl, where most of the COCl groups are crowded at the tube ends. Once some of the COCl groups are attached to the nonflexible ring structure of the amines, the steric effect will be created and will prevent further reaction. Gu et al [104] have also reported similarly incomplete reactions for SWNTs. However, when the amino group is attached to a flexible chain compound, the steric hindrance problem is less serious. For example, in the case of enzymes with

molecular weights as high as 30k dalton (for AK) and 50k dalton (for PPL), a greater degree of amidation is seen even under milder conditions when reacted with SWNT-COCl. Spectra (d) and (e) in Figure 1 confirm these linkages for SWNT-AK and SWNT-PPL respectively. Peaks at 3270 cm^{-1} in (d) and (e) can be assigned to N-H and O-H stretching vibrations from the enzymes tethered to the SWNTs. Peaks at 2960 cm^{-1} , 2920 cm^{-1} and 2860 cm^{-1} in spectrum (d) and at 2920 cm^{-1} in (e) correspond to different C-H bond stretching vibrations associated with the enzyme. The newly formed amide bond of the two enzyme functionalized SWNTs are slightly downshifted (observed at 1630 cm^{-1} for both of them relative to values of 1640 cm^{-1} and 1650 cm^{-1} for the amines), which is due to coupling with some of the functional groups from the enzyme. Small peaks at 1730 cm^{-1} and 1740 cm^{-1} belong to the C=O stretching vibration of COOH groups, which are converted from unreacted COCl group by hydrolysis during the purification process. As mentioned earlier, the carboxylation of SWNTs is achieved by two different methods, but there is no obvious difference in the ATR-FTIR spectra of SWNT-(COCl)_x generated using SWNT-(COOH)_x samples prepared by the two methods.

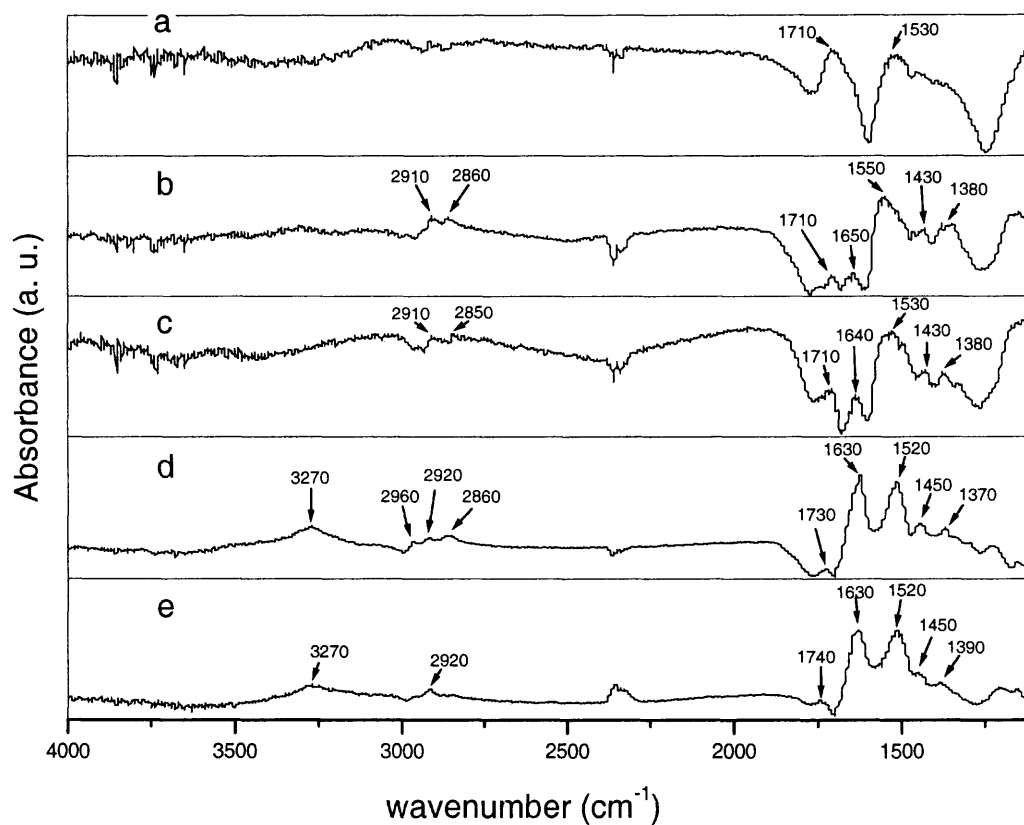


Figure 5.1 ATR-FTIR spectra of (a) SWNT-COCl, (b) SWNT-*cis*-Myrtanylamine, (c) SWNT- N- (3-morpholinopropyl)-2, 4, 6-trinitroaniline, (d) SWNT-AK, and (e) SWNT-PPL.

The Raman measurements were performed using instrumentation described in Chapter 3 – Section 3.4. and 632.8 nm excitation. The Raman spectra of the five amine functionalized SWNTs are very similar since due to resonance-enhancement only the Raman lines of SWNTs are observed. Therefore, a representative spectrum of *cis*-Myrtanylamine functionalized SWNTs along with the spectra of pristine SWNTs and two enzyme functionalized SWNTs are shown in Figure 5.2

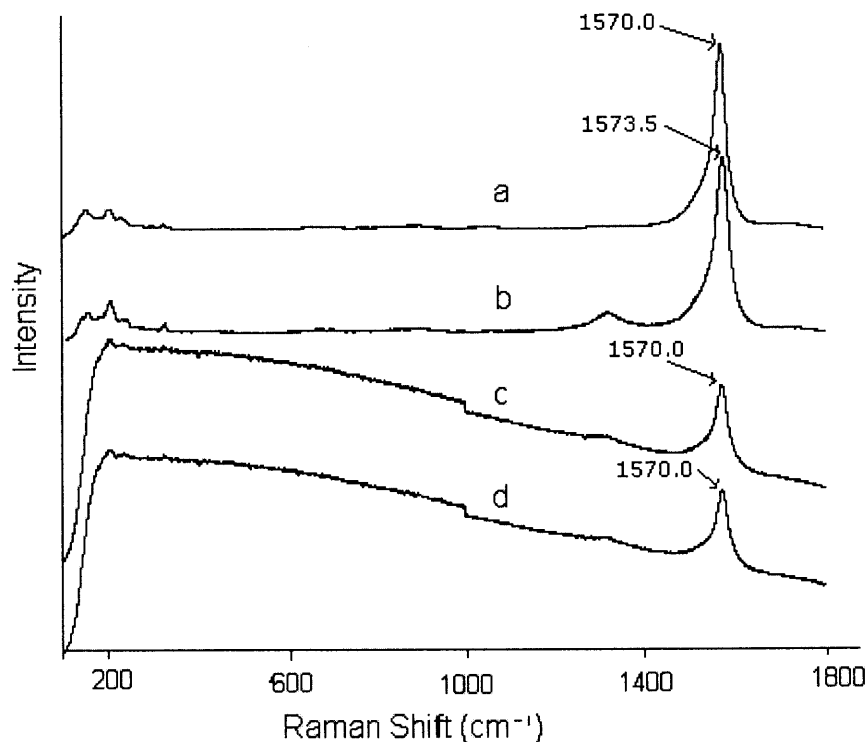


Figure 5.2 Raman spectra of pristine SWNTs sample (a), *cis*-Myrtanlyamine functionalized SWNTs (b), SWNT-AK (c), and SWNT-PPL (d).

As shown in Figure 5.2(a) and (b), the Raman spectrum of *cis*-Myrtanlyamine functionalized SWNTs is very similar to that of pristine SWNTs except for a small upshift of the tangential C=C line in *cis*-Myrtanlyamine-SWNT and an increase in intensity of the disorder mode peak at 1320 cm^{-1} caused by an increase in defects created during the functionalization process. The Raman spectra of SWNT-AK (spectrum c) and SWNT-PPL (spectrum d) show strong luminescence similar to that reported earlier after functionalization of SWNTs with large molecules [105]. No change in frequency of the C=C tangential stretching mode and some increase in the defect mode intensity relative to the spectrum of the pristine SWNTs are observed.

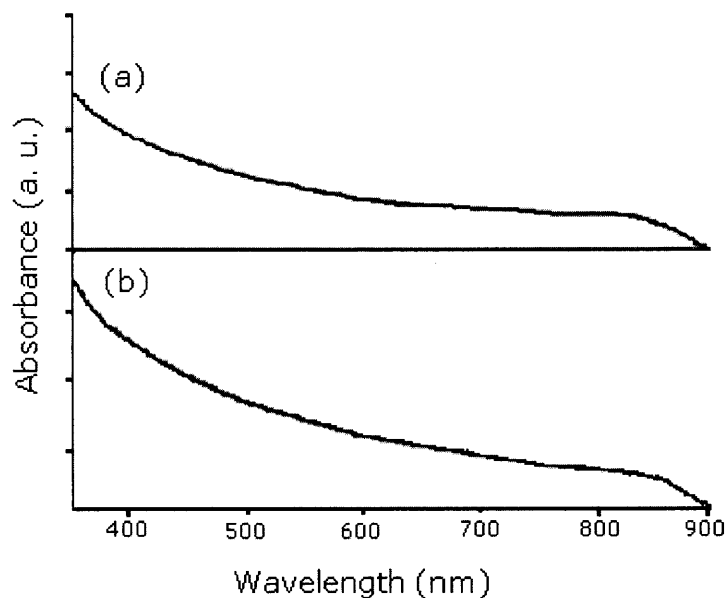


Figure 5.3 UV-vis absorption spectra of (a) SWNT-PPL and (b) SWNT-AK in aqueous solution.

The featureless UV-vis absorption spectra of the enzyme functionalized samples taken in weak aqueous solutions are similar to the observations in an earlier study by Huang et al [105]. This observation of featureless spectra in the UV-visible region indicates a disruption in the one-dimensional electronic structure of the SWNTs due to bond formation (Figure 5.3) [105-107].

In order to observe the morphology of the functionalized carbon nanotubes, FE-SEM imaging of the samples were carried out and compared with those of the pristine SWNTs. A representative image of *cis*-Myrtanylamine functionalized SWNTs, along with an image of pristine SWNTs are shown in Figure 5.4. Also shown are the images of SWNTs functionalized with other enzymes.

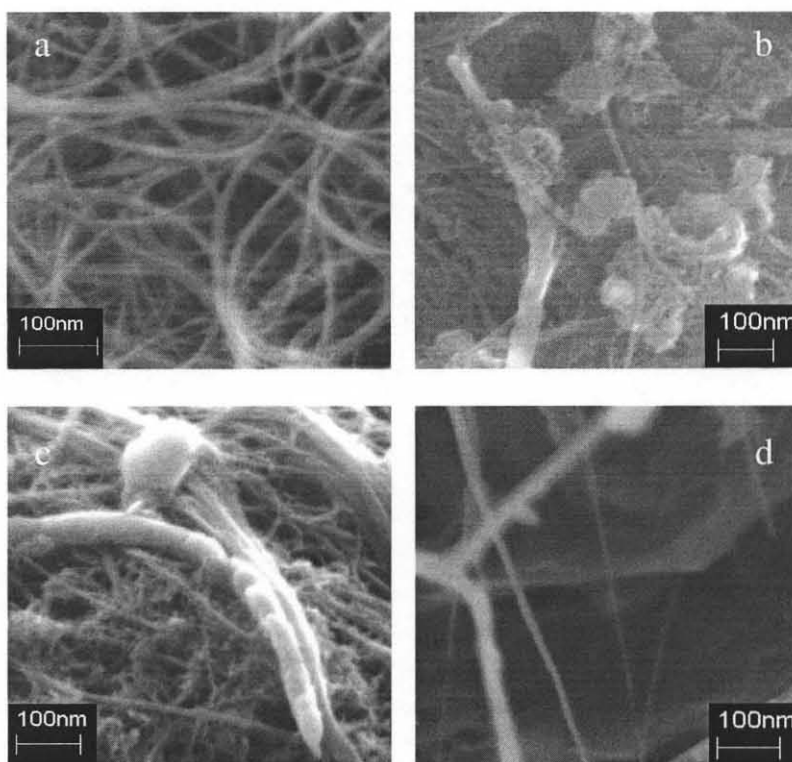


Figure 5.4 FE-SEM images of (a) pristine SWNTs, (b) cis-Myrtanylamine functionalized SWNTs, (c) AK functionalized SWNTs and (d) PPL functionalized SWNTs.

Images (a), (b) and (c) were obtained from powders dispersed on conducting tape, whereas image (d) was obtained after evaporating a drop of an aqueous suspension of the sample on a gold substrate. Image (a) is from purified pristine HiPCO SWNTs. Trace amounts of iron catalyst are evident but the image shows large amounts of pristine nanotube bundles. After functionalization the created defects and covalently attached amines causes the electrical conductivity of the functionalized nanotube bundles to be reduced. This causes partial blurring of the images of the functionalized SWNTs resulting in reduction of the contrast and resolution. Feng et al. [104] have observed similar features on functionalized SWNTs. Ribbon-, bamboo- and cotton- like features on the SWNTs are seen in the images of the functionalized nanotubes, consistent with wrapping

and functionalization of the tubes by the enzymes. The wrapping process can occur on individual tubes or might involve an entire bundle.

In conclusion, functionalization of SWNTs with various primary and secondary amines, as well as with two different enzymes was demonstrated. These molecules attach via bonding to the tube ends or the sidewalls of the SWNTs as shown by FTIR data, resulting in some modification of their 1D electronic properties.

5.3 Microwave-Induced Rapid Chemical Functionalization of Single Wall Carbon Nanotubes

The SWNTs usually aggregate into bundles (or ropes of tubes) that are held together by weak van der Waals forces as discussed in Chapter 1. These bundles can contain from a few to up to several tens of tubes arranged in a hexagonal lattice [108]. In addition, as-prepared SWNT sidewalls are usually defect-free and therefore rather inert to chemical attack.

For the chemical functionalization of SWNTs, much of the effort so far has involved the use of typical chemical techniques, such as refluxing and sonication. SWNTs are usually treated in different solvents using a combination of refluxing, heating and stirring. Many of these reactions need to be carried out over long periods of time. For example, for carboxylation, SWNTs are often refluxed in conc. HNO_3 for 10 to 50 hrs. Further functionalization, such as acyl chlorination and amidation [104,109], diimide-activated amidation [54] and 1, 3-dipolar cycloaddition [55,56] require additional days of reaction time. Consequently, if functionalized SWNTs are to find their way into applications, there is an urgent need to develop techniques for rapid (of the order of minutes to hours) chemical functionalization.

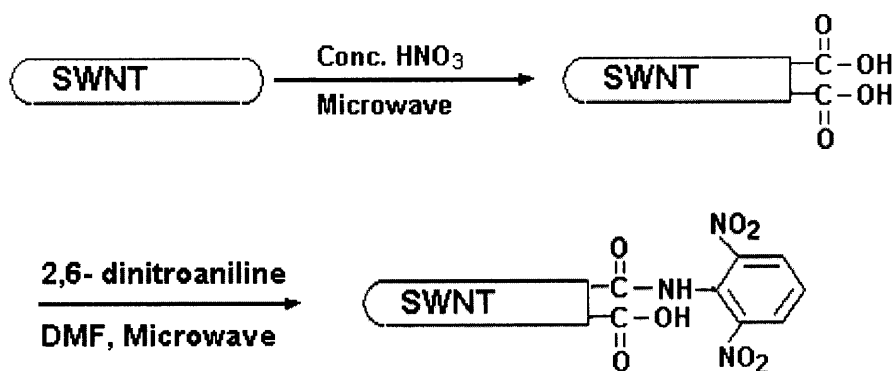
Chemistry under microwave radiation is known to involve a different, faster and more efficient mechanism [110-112] than that under conventional chemical processing conditions. Microwave processing also reduces the need for solvents, thus it is eco-friendly. It has been exploited in a variety of organic syntheses involving heterocyclic [113] and organometallic [114] compounds, and in combinatorial chemistry [115,116]. Some of the reported advantages are high yields, and rapid reaction under controlled temperature and pressure (especially in a closed system), and high purity products due to the short residence times involved. Additionally, the chemical activation parameters are modified due to further polarization of the dipoles under microwave radiation. For example, it has been reported by Lewis [117] that during imidization of polyamic acid, the apparent activation energy is reduced from 105 to 57 KJ/mol.

In the work discussed in this chapter three types of SWNT functionalizations – amidation, 1,3-dipolar cycloaddition, and extensive nitration – have been successfully carried out under microwave radiation within minutes. The experiments were carried out in a CEM Model 205 microwave oven with a 100 ml reaction chamber, which was lined with Teflon PFA[®] and fitted with a 0~200 psi pressure controller.

5.3.1 Amidation

The amidation reaction is illustrated in Scheme 5.2 below. The first step is the generation of carboxylic acid groups on the SWNT sidewalls and tube ends. In a typical reaction, 6 to 10 mg of pristine SWNTs (prepared by the HiPCO process and obtained from Carbon Nanotechnologies Inc.) were loaded into an extraction vessel along with 20 ml of 70% HNO₃. The microwave power was set to 75% of a total of 900 watts, the pressure was set

at 125 psi, and the reaction was carried out for 10 to 15 minutes. After cooling to room temperature, the reacted mixture was filtered, washed with de-ionized (DI) water and dried. About 5 mg of this carboxylic acid grafted SWNT sample was used to react with 2, 6-dinitroaniline. For the amidation reaction, 20 ml of *N,N*-Dimethylformamide (DMF) was used as the solvent, 15 to 20 mg of 2,6-dinitroaniline was added, and all other conditions remained the same as before. The reaction was carried out for 15 to 20 minutes. Once cooled, the mixture was filtered, washed with DMF and finally with anhydrous tetrahydrofuran (THF). After vacuum drying at room temperature for a few hours, the sample in powder form was analyzed by FTIR and Raman spectroscopy.



Scheme 5.2 Model microwave induced reaction of amidation of SWNTs

The typical chemical approach to amidation of SWNTs involves carboxylation, acyl chlorination, and then amidation [50,104,109]. It involves three steps and a typical reaction time is between 3 to 5 days. The amidation of SWNTs using microwaves is a two-step process (as shown in Scheme 5.2), and the total reaction time is between 20 to 30 minutes. SWNTs functionalized by the microwave induced amidation process were characterized by FTIR and Raman spectroscopy. Figure 5.5 (a,b and c) shows the FTIR spectra of pristine SWNT, HNO_3 treated SWNT and 2, 6-dinitroaniline functionalized

SWNTs, respectively. In Figure 5.5(a), the peak at 1580 cm^{-1} is assigned to the C=C stretching mode associated with SWNT sidewall defects generated during synthesis. The line at 1626 cm^{-1} in all the spectra shown in Figure 5.5 is assigned to the bending mode of traces of water in the KBr used for making the pellet for infrared spectroscopy. The line at 1730 cm^{-1} is clearly assigned to the C=O stretching mode in the HNO_3 -treated SWNT and indicate successful generation of $-\text{COOH}$ groups on the nanotubes (Figure 5.5b). The sharp peak at 1384 cm^{-1} is likely to be associated with the nitro group formed during the high pressure HNO_3 treatment under microwave conditions; alternatively, it can be assigned to surface KNO_3 formed by reaction of KBr with the nitro groups on the SWNTs. After the reaction with 2, 6-dinitroaniline, the amide linkage formed at the C=O bond site, is associated with the line observed at 1650 cm^{-1} (Figure 5.5). The observation of the line at 1730 cm^{-1} in Figure 5.5 indicates incomplete reaction with $-\text{COOH}$ due to steric hindrance of the rigid ring of the attached amine [104].

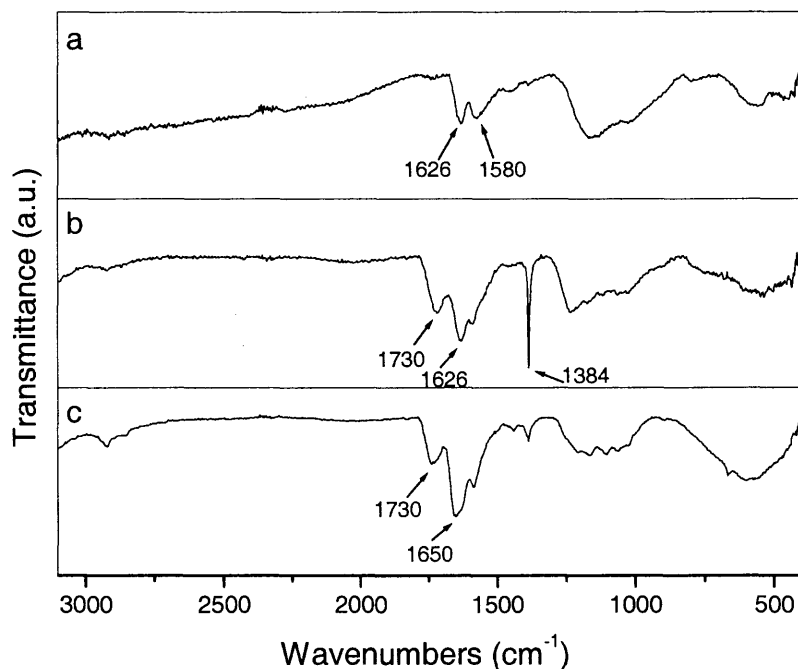


Figure 5.5 FTIR spectra of samples from the microwave-induced amidation reaction of SWNTs: (a) pristine SWNTs; (b) HNO₃ reacted SWNTs; and (c) 2, 6-dinitroaniline functionalized SWNTs.

The Raman spectrum of the functionalized SWNTs [Figure 5.6(c)] showed significant fluorescence background relative to that observed in the spectrum of the pristine and nitric acid treated SWNTs [Figure 5.6 (a) and (b)] due to the tethering of the photoluminescent amine molecules on the SWNT structure. Several other groups have been reported similar observations [54,118,119]. The observed increase in intensity of the defect mode at 1330 cm⁻¹ is attributed to increased sp³ -hybridized defects on the sidewalls induced by the functionalization process[120,121]. Similar to the Raman spectra of enzyme functionalized SWNTs, the Raman spectra of the functionalized nanotubes arise only from SWNTs due to resonance-Raman scattering.

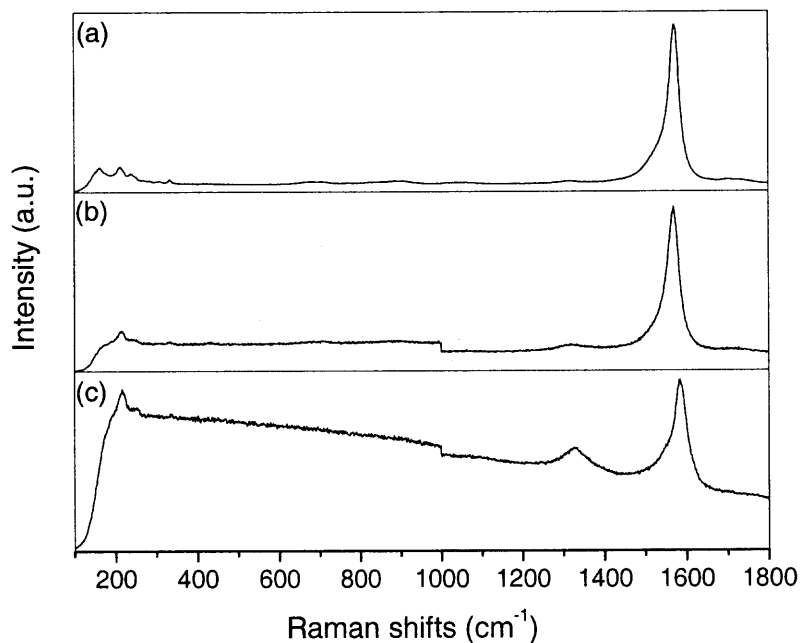
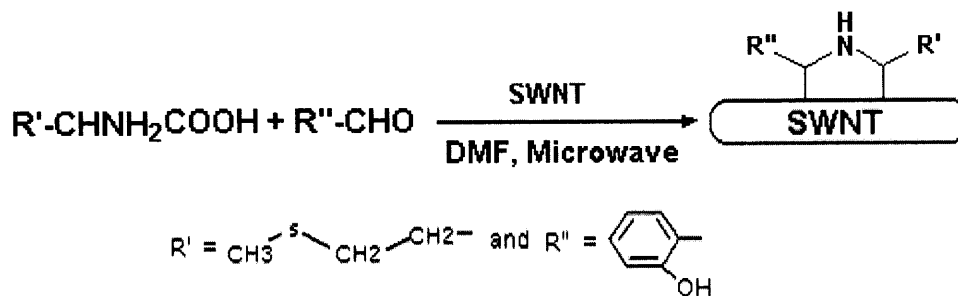


Figure 5.6 Raman spectra of samples from the microwave-induced amidation of SWNTs: (a) pristine SWNTs; (b) nitric acid treated SWNTs; (c) 2, 6-dinitroaniline functionalized SWNTs. The Raman spectra were measured using identical spectral and excitation parameters except for a factor of 2 lower averaging time for spectrum (c).

5.3.2 1,3-Dipolar Cycloaddition

The 1, 3-dipolar cycloaddition reaction of SWNTs together with an α -amino acid and an aldehyde is shown in Scheme 5.3 below.



Scheme 5.3 Model microwave induced:1,3-dipolar cycloaddition reaction on SWNTs.

In a typical reaction, about 10 mg of pristine SWNTs and 70 mg of salicylaldehyde were suspended in 20 ml DMF. Then, the mixture was reacted in the microwave reactor for 5 minutes at 90% microwave power, and at a pressure of 160 psi. After cooling, 2 ml of methionine suspension (70 mg in 4 ml DMF) was added to the reaction vessel. The reaction was then carried out for 5 minutes at the same power and pressure levels. The reaction vessel was cooled, the other half of the methionine suspension was added, and the reaction was carried out for another 5 minutes under the same conditions. The reacted mixture was filtered, and the organic phase was evaporated under vacuum. The resulting dark brown oil was extracted with a two-phase mixture of $\text{CHCl}_3/\text{H}_2\text{O}$. The organic phase was washed with water and dried over Na_2SO_4 . It was evaporated, washed with ethyl ether, and yielded about 7 mg of dark brown solid. The solid obtained was characterized using FTIR, proton NMR, and UV-vis-NIR spectroscopy and by SEM imaging.

Just like the amidation reaction, the 1, 3-dipolar cycloaddition of SWNTs is a tedious and time-consuming process when carried out by conventional chemical methods. Literature reports show that it takes as long as five days to complete this reaction [55]. As mentioned in the experimental section, the microwave-induced reaction time requires only between 20 to 30 minutes. The final product comprising of 1, 3-dipolar cycloaddition reacted SWNTs is very soluble in CHCl_3 , CH_2Cl_2 and dimethylformamide (DMF). The FTIR spectra of the functionalized product together with that of L-methionine and salicylaldehyde, are shown in Figure 5.7. The functionalized SWNTs (Figure 5.7c) clearly show the absence of the lines due to the aldehyde C-H stretching modes at frequencies of 2749 cm^{-1} and 2845 cm^{-1} , which were present in the spectrum of

the starting aldehyde (Figure 5.7b). As shown in Scheme 5.2(b), the aldehyde group is likely to be removed by the functionalization process. Therefore, the absence of the aliphatic C-H stretching peaks in Figure 5.7c would indicate that the reaction had occurred. The aromatic C-H stretching frequency in Figure 5.7c at 3052 cm^{-1} is slightly shifted to lower frequencies relative to its position at 3060 cm^{-1} in the spectrum for the aldehyde shown in Figure 5.7b. The lines at frequencies of 2917 cm^{-1} and 2849 cm^{-1} in Figure 5.7c are associated with the attached amino acid. Note that these peaks are absent in the FTIR spectrum of pristine SWNTs shown in Figure 5.5a. This also showed that functionalization of the SWNTs had taken place.

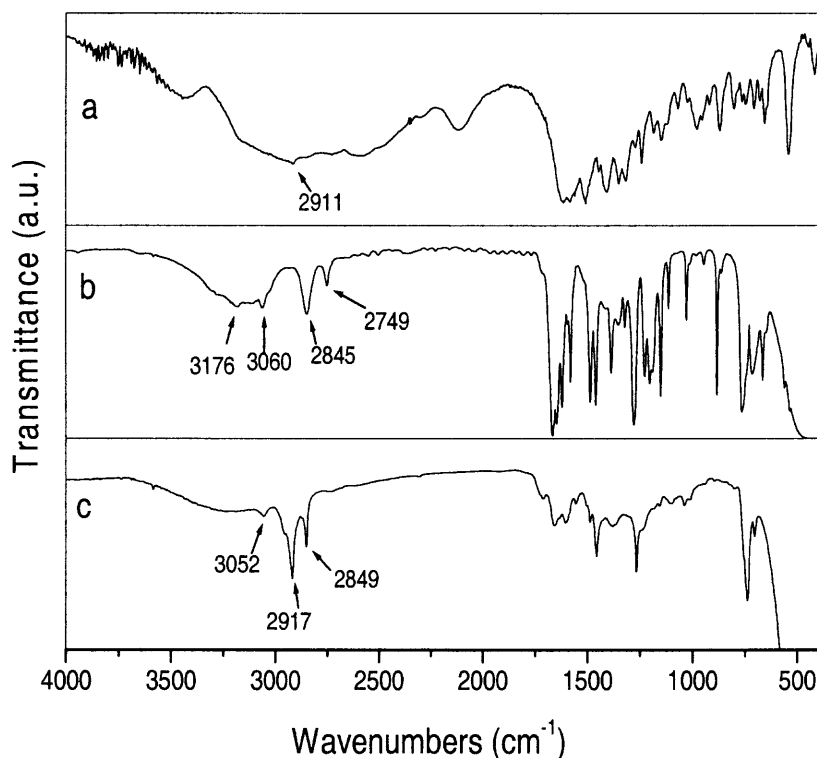


Figure 5.7 FTIR spectra of samples from the microwave-induced 1,3-dipolar cycloaddition of SWNTs: (a) L-methionine; (b) salicylaldehyde; and (c) final product from the 1,3-dipolar cycloaddition reaction.

Proton NMR measurements were performed on CDCl_3 solutions of the 1, 3-dipolar cycloaddition product, and the spectrum was found to be consistent with the

proposed functionalized SWNT structure shown in Scheme 5.3. The aromatic-H from salicylaldehyde was still observed, but the aldehyde proton line at 9.9 ppm was replaced by a new peak at 1.9 ppm. Likewise, the peak for the proton that is in the alpha position relative to the COOH group in methionine shifted slightly from 3.84 ppm to 3.80 ppm in the product. These observations also support the analysis of the FTIR data discussed above.

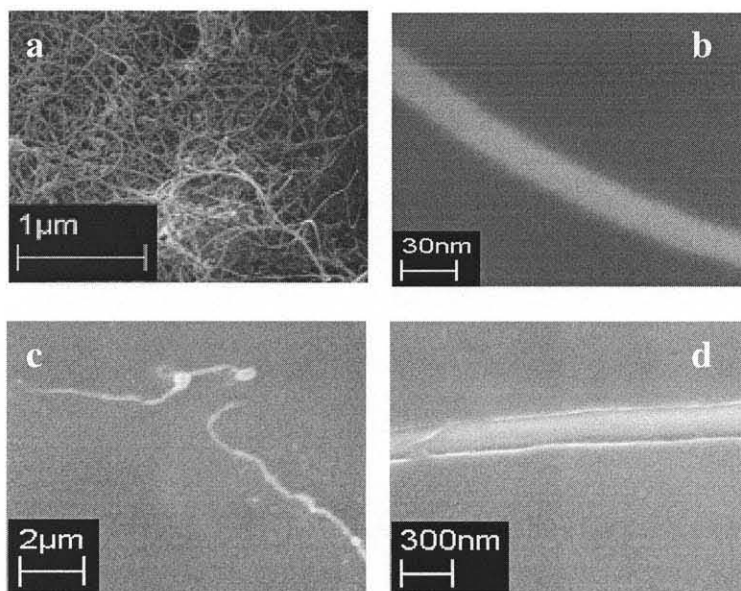


Figure 5.8 SEM images of samples used in the microwave-induced 1,3 cycloaddition reaction on the SWNTs: (a) pristine SWNT bundles; (b) individual bundle of pristine SWNTs; (c) SWNT bundles dispersed in chloroform after functionalization; (d) single SWNT bundle after functionalization. Note increase in diameter. Images (a) and (b) were taken with the sample in powder form, whereas (c) and (d) were obtained from the film formed after evaporating a drop of a solution of the reaction product in chloroform on a glass substrate.

SEM images of pristine SWNTs and their 1,3-dipolar cycloaddition functionalized products, which were taken to observe the morphology of the functionalized nanotubes, are presented in Figure 5.8. As shown in Figure 5.8a, the pristine SWNTs exist as bundles. Figure 5.8b shows a typical bundle of 20 to 30 nm in

diameter. Figure 5.8 c and d show the SWNTs after functionalization. The images were obtained on a film formed by evaporating a drop of the chloroform solution of the functionalized product. Although the cylindrical shape of the SWNTs is still intact, the attachment of the functional groups roughened the tube surface, and the diameter increased tenfold due to the molecules tethered to the sidewalls. The presence of only two SWNT bundles in the low magnification image in Figure 5.8c shows that the number density of individual SWNT bundles relative to that in the pristine sample had decreased as a result of untangling of the tube bundles due to functionalization and dispersion in the solvent.

Ultraviolet (UV) absorption spectra provided further evidence for 1,3 dipolar cycloaddition functionalization of the SWNTs by microwaves. The UV spectrum of the starting mixture taken as a fine suspension/solution in chloroform (CHCl_3) in the same ratio as in the reaction showed two broad absorption bands at about 250 and 330 nm. After the reaction, the bands shifted by 5 to 10 nm to shorter wavelengths. This blue-shift indicates a change in the electronic states of salicylaldehyde and methionine in the starting mixture resulting from interaction with the SWNT structure [122] and in agreement with observations reported in a previous study [55].

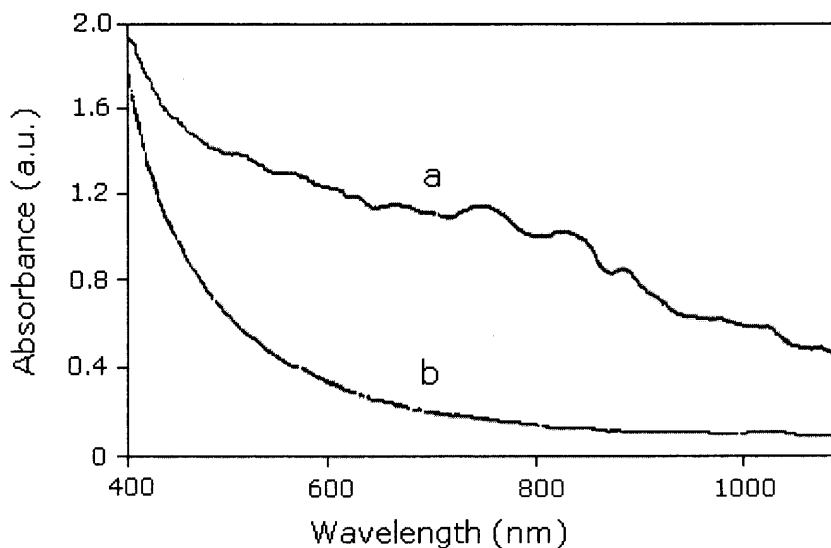


Figure 5.9 Vis-NIR spectra of (a) pristine SWNTs suspended in DMF; (b) final product from the microwave induced 1, 3-dipolar cycloaddition of SWNTs in DMF.

Spectra measured in the visible-near IR (NIR) region are shown in Figure 5.9. Figure 5.9a shows the spectrum of a relatively concentrated suspension of pristine SWNTs in DMF, whereas Figure 5.9b shows the spectrum of the final product of 1,3-dipolar cycloaddition of SWNTs in DMF solution. In case of the pristine SWNTs (Figure 5.9a), the optical transitions across the van Hove singularities in the 1D electronic-density-of-states are clearly seen around 740, 820, and 890 nm (45, 46). For the functionalized SWNTs, the van Hove absorption bands disappeared (Figure 5.9b), indicating a substantial change in the dimensionality of the electronic states of the SWNT structure similar to observations made in previous studies (123,124).

5.3.3 Preparation and Characterization of Rapidly Functionalized Highly Water-Soluble SWNTs

Solubility of carbon nanotubes in water would allow chemical derivatization and manipulation to be easily carried out. Considerable efforts have therefore been made [43,45,46,124-127] to make carbon nanotubes soluble in water and in organic solvents,

but to date only with limited success. Moreover, the solubilities achieved are mostly due to water-soluble macromolecules attached to the nanotubes [43,124,125]. Here an environmentally friendly, microwave-induced method to prepare highly water-soluble single-walled nanotubes (SWNTs) in about three minutes, using a closed vessel reactor, is discussed. Solubilities of more than 10 mg of nanotubes per milliliter of water and ethanol were obtained, which is about tens to thousand times higher than what has been previously reported [43,45,46,124-126]. The solutions were free of suspended nanotubes as determined by light scattering measurements, and for the first time the Raman spectrum of SWNTs was obtained from its solution phase. This relatively simple microwave technique to produce highly water-soluble nanotubes will enable processing of nanotubes in bulk quantities and hasten real-world applications of this unique material.

The SWNTs used for these experiments were those obtained from Carbon Nanaotechnologies Inc and the other chemicals used were purchased from Sigma Aldrich. In a typical reaction, 10 to 20 mg of SWNTs were added to 20 ml of a mixture of 1:1 nitric acid (70%) and sulfuric acid (97%) in the reaction chamber. The reaction vessel was then subjected to microwave radiation. The microwave power was set at 50% of a total of 900 watts, and the pressure was set at 20 psi. The microwave-induced reaction was carried out for 1, 2, 3, 5, 10 and 20 minutes respectively. Three minutes was found to be the optimum reaction time. At this point, the functionalized SWNTs became highly water soluble, and no nanotubes were lost. After the reaction, the reacted mixture was diluted with de-ionized (DI) water. Then the mixture was filtered through a 10 μ m polytetrafluoroethylene (PTFE) membrane paper, and the filtrant was transferred to a dialysis bag (nominal MWCO 12,000-14,000). When the pH reached 7, the diluted

mixture was removed and concentrated in a vacuum evaporator. The resulting black SWNT solids were used for testing solubility and for characterization. The spectra shown are from nanotubes that were reacted for 3 minutes.

Functionalized SWNTs obtained after three minutes of microwave treatment were found to have solubilities of more than 10 mg of SWNTs per milliliter of DI water and ethanol under ambient conditions, and significantly higher solubilities were obtained in acidic water. Photographs of aqueous solutions of different concentrations of functionalized SWNTs produced by this method are shown in Figure 5.10

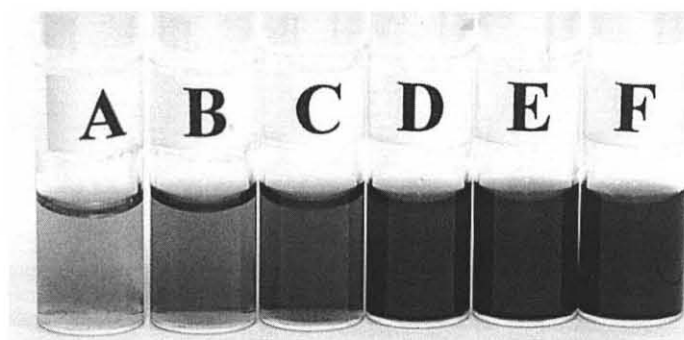


Figure 5.10 Photographs of nitrated SWNT solutions of different concentrations in DI water: (A) 0.05mg/ml, (B) 0.1 mg/ml, (C) 0.2 mg/ml, (D) 0.3 mg/ml, (E) 0.5 mg/ml and (F) 2mg/ml.

Laser light scattering particle size measurements of the aqueous solutions of microwave functionalized SWNTs were compared with measurements made on an aqueous suspension of pristine SWNTs. The suspension prepared by sonication of a mixture of 0.1 weight % and 0.5 weight % of the surfactant Triton-X showed particle sizes ranging from 100 nm to 600 nm with a peak at 300 nm at detection angles of 62.2 and 90 degrees. In contrast, a typical aqueous solution of microwave functionalized SWNTs (0.5 mg/ml) did not show the existence of particles in the 3 to 800 nm size range, clearly indicating that these nanotubes dissolve in water.

SWNTs deposited from aqueous solution show scanning electron microscope (SEM) and transmission electron microscope (TEM) images displayed in Figure 5.11 A and B, respectively. The SEM images indicate clear alignment of the depositing nanotubes resulting from capillary forces during evaporation of water molecules from the solution.. Alignment of the carbon nanotubes is seen each time after evaporation of a drop of the solution. The TEM image shows extensive debundling of the SWNT ropes or bundles, but no indication of structural modification of the sidewalls can be seen at this magnification level.

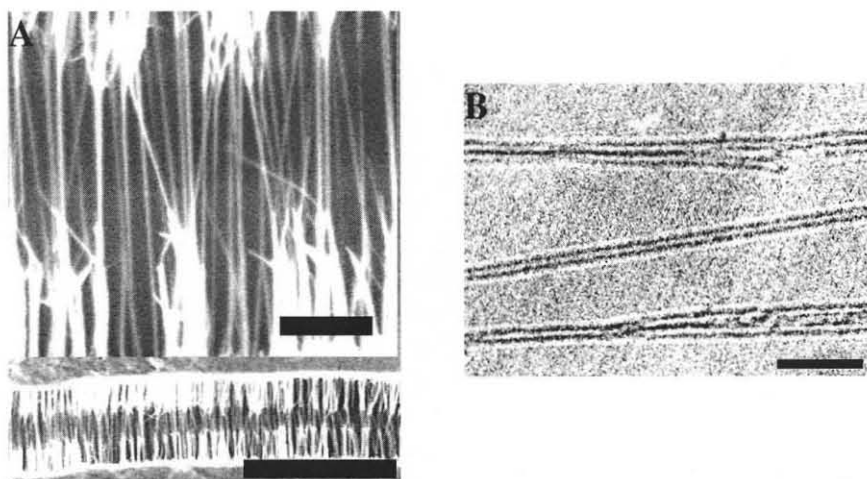


Figure 5.11 SEM and TEM images of microwave nitrated SWNTs deposited from aqueous solution: (A) Bottom: Lower magnification SEM image showing alignment of the nitrated SWNTs, scale bar = 2 μm ; Top: Higher magnification image of the aligned SWNTs, scale bar = 200 nm. (B) TEM image of debundled nitrated SWNTs, scale bar = 10 nm.

In order to characterize the chemical groups formed on the nanotube sidewalls and tube ends after microwave treatment, the author measured the Fourier-Transform infrared (FTIR) and Raman spectra of the functionalized SWNTs, which are shown in Figure 5.12. The FTIR spectrum of the pristine nanotubes (Figure 5.12a, left panel) is featureless because infrared active absorptions in pristine SWNTs are weak. After three minutes of microwave treatment, infrared lines at 1355 cm^{-1} and 1637 cm^{-1} , attributed to

the symmetric and asymmetric stretching modes, respectively, of $-\text{NO}_2$ groups, are observed, indicating strong nitration of the SWNTs. The lower frequency infrared lines at 1200 and 1048 cm^{-1} are likely to be associated with a largely C-N stretching mode with some mixed character [54]. The line at a frequency of 1719 cm^{-1} is due to the C=O stretching mode associated with the formation of $-\text{COOH}$ groups on the SWNTs, whereas the strong and broad line centered at 3422 cm^{-1} is associated with the $-\text{OH}$ stretching mode of the $-\text{COOH}$ group.

In the Raman spectrum of pristine SWNTs (Figure 5.12a, right panel), SWNTs of three different diameters are indicated by the peaks at 189 cm^{-1} , 213 cm^{-1} and 252 cm^{-1} (corresponding to 1.3nm, 1.2 nm and 1.0 nm respectively) due to the SWNT radial breathing modes (RBMs). The strong tangential C-C mode is seen at 1578 cm^{-1} , and a weak line due to defects and disorder on the SWNT framework is observed at 1299 cm^{-1} . After three minutes of nitration, only the RBM line at 189 cm^{-1} associated with larger diameter SWNTs, is observed (Figure 5.12b, right), suggesting that the smaller diameter SWNTs were the first to be functionalized. Compared to the Raman spectrum of pristine SWNTs there is a 2 cm^{-1} up-shift of the tangential mode frequency of the reacted SWNTs probably due to the attachment of electronegative groups, such as $-\text{COOH}$ and $-\text{NO}_2$ to the SWNT backbone. Furthermore, the broad line in the defect mode region of the spectrum broadens, shifts up in frequency and dramatically increases in intensity. This is due to the extensive nitration and carboxylation of the sidewalls and tube-ends resulting in sp^3 hybridization and disorder on the nanotube framework [48,121]. Part of the broadening and up-shift can also be attributed to the appearance of the symmetric stretching mode of the $-\text{NO}_2$ groups in the Raman spectrum. Figure 5.12c (right panel)

shows the Raman spectrum of the functionalized SWNTs in aqueous solution – the first time such a spectrum has been obtained for SWNTs. Probably because of water molecules adsorbed around the tubes, RBM modes are not observed and the tangential mode frequency is shifted up in value by 15 cm^{-1} relative to that of the functionalized solid.

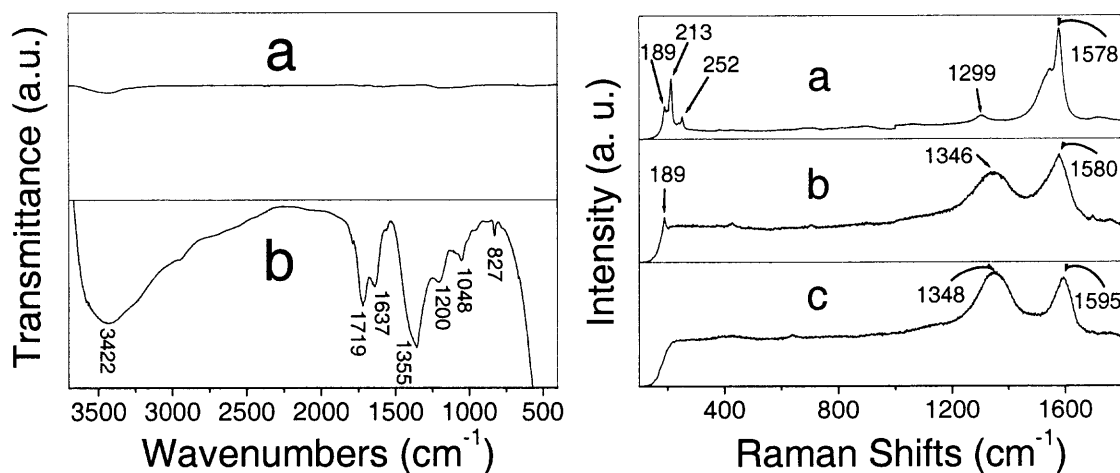


Figure 5.12 FTIR and Raman spectra (excited by 632.8 nm radiation) of the functionalized SWNTs: (Left panel) FTIR spectra of: (a) pristine SWNTs; (b) microwave nitrated SWNTs. (Right panel) Raman spectrum of: (a) pristine SWNTs, (b) microwave nitrated SWNTs in solid phase, and (c) microwave nitrated SWNTs in aqueous solution.

Further characterization of the functionalized SWNT aqueous solutions were performed using visible-near infrared (vis-NIR) absorption spectroscopic measurements of the solutions and comparing a typical spectrum to that taken from a suspension of pristine SWNTs in dimethylformamide (DMF) (Figure 5.13 left panel). Inter-band transition absorptions associated with the van Hove singularities in quasi-one dimensional pristine SWNTs are clearly seen at 740, 820 and 890 nm in spectrum of the pristine SWNTs shown on the left panel of Figure 5.13 (spectrum a). The corresponding spectrum of the microwave nitrated solution is featureless, indicating a loss of the quasi-one dimensional SWNT structure due to extensive functionalization of the sidewalls. The

degree of nitration and carboxylation of the SWNT structure indicated by the infrared and Raman data was quantified by thermogravimetric analysis (TGA) measurements on pristine and microwave functionalized SWNTs performed under dry nitrogen at a heating rate of 10°C per minute from 30° to 500°C. The TGA traces shown in right panel of Figure 5.13 indicate that compared to pristine SWNTs, the functionalized SWNTs lose about 50% of their weight due to dissociation of the $-\text{NO}_2$ and $-\text{COOH}$ groups from the nanotube sidewalls and tube ends. It is estimated that approximately every four carbons on the SWNT structure is functionalized by the microwave process.

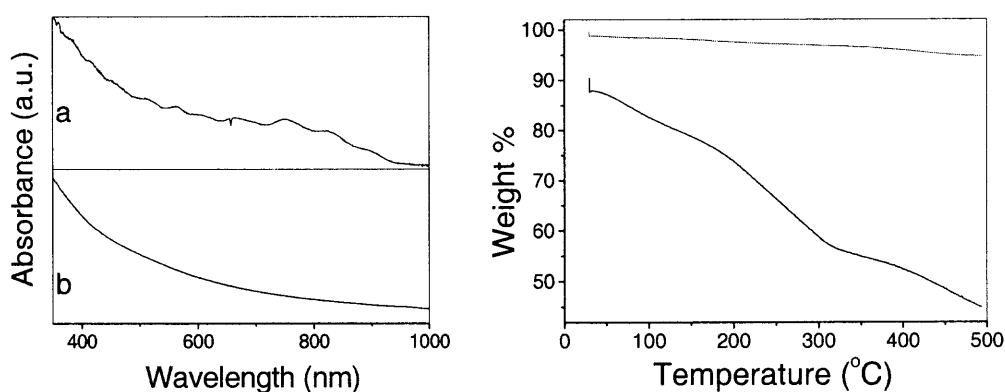


Figure 5.13 Visible-near infrared (vis-NIR) spectra and thermogravimetric analysis (TGA) data under pure nitrogen at a heating rate of 10°C per minute for pristine and microwave functionalized SWNTs: (Left panel) Vis-NIR spectra of: (a) Pristine SWNTs suspended in dimethylformamide, (b) Aqueous solution of microwave reacted nanotubes. (Right panel) TGA of: (red) pristine SWNT powder and, (black) microwave functionalized SWNTs.

In summary, the results obtained are of great relevance to the chemical and physical manipulation of carbon nanotubes in nanotechnology. The high water and alcohol solubility will enable SWNTs to be more easily processed in operations involving chemical reactions, physical blending, or thin film formation. Moreover, their alignment

during deposition from solution will facilitate the creation of novel nanoelectronic device architectures.

5.4 Electrochemical Nitration of Single Wall Carbon Nanotubes

Electrochemical reactions are important because they can be carried out selectively on device structures and are likely to become increasingly important. Moreover, electrochemical processing is relatively simple and clean.

A relatively facile and scalable electrochemical strategy was developed for the direct functionalization of SWNTs with nitro-groups. Nitrated SWNTs are capable of hydrogen bonding to organic polymers to form nanocomposites with enhanced mechanical strength. Similar electrochemical approaches using a nanotube electrode have also been used to electrochemically physisorb or chemisorb hydrogen [129,130] and to functionalize SWNTs with an organic salt [48]. However, this is the first time to the best of our knowledge that direct chemical functionalization has been electrochemically induced, raising the possibility of wider use of electrochemical techniques for the controlled functionalization of carbon nanotubes.

The SWNTs used in this study were synthesized by pulsed laser ablation at Rice University by Tubes@Rice of Houston or by carbon arc techniques (by Carbolex Inc). The as-received nanotubes were purified in 2.6 M nitric acid solution by refluxing for 45 hours to remove amorphous carbon formed during synthesis and the Co/Ni catalyst used. This was followed by washing in de-ionized water and centrifugation to obtain agglomerated SWNTs, which were de-agglomerated and suspended in water by sonication in the presence of Triton X-100 surfactant. The suspension was then vacuum-

filtered through 0.5 to 5 micrometer pore size Teflon-coated membranes. After washing with de-ionized water, a self-assembled, free-standing sheet consisting entirely of SWNT bundles was peeled off the filtration membrane. Prior to use the SWNT sheets were annealed for 2 hours at 120°C, 1 hour at 300°C and 30 minutes at 800°C in flowing argon, to remove water, remnants of the surfactant and functional groups formed during the acid reflux. Scanning and transmission electron microscopy showed that the SWNT sheets comprise essentially of bundled SWNTs with extremely small amounts of left over catalyst as indicated by electron paramagnetic resonance measurements. Raman spectroscopy in the low frequency radial breathing mode region showed an average individual tube diameter of 1.5 nm (9,9) and (10,10) individual arm-chair SWNTs. The average diameter of individual tubes within bundles is consistent with the images obtained by transmission electron microscopy.

An electrochemical cell filled with 6M aqueous solution of KNO_2 as electrolyte was used for the nitration experiments (see Figure 6.1 for schematic of a similar electrochemical cell). A freestanding SWNT sheet was used as the working electrode (anode), nickel or platinum foil was used as the counter electrode, and a saturated calomel electrode (SCE) as the standard electrode. Experiments were carried out for 3 to 10 hours under a positively charging potential using a computer-controlled 273 EG&G Princeton Applied Research potentiostat-galvanostat.

The micro-Raman data reported were checked at about 20 spots in different regions of the sample. Attenuated-total-reflectance Fourier-transform infrared (ATR-FTIR) spectra were measured directly on the pristine and nitrated SWNT sheets. Thermogravimetric analysis (TGA), differential thermal analysis (DTA) and transmission

electron microscopy (TEM) were also carried out for analysis. The thermoelectric power was measured via the Seebeck voltage generated across contacts at two ends of the sheet, one of which was held at 300 K and the other at a higher temperature.

Electrochemical nitration experiments were carried out using SWNT sheet electrodes annealed as described above. Anodic charging was conducted potentiostatically for 3 to 10 hrs at potentials near 1.0 volt versus SCE. Continuous cyclic voltammogram (CV) sweeps were carried out from -1.0 V to $+1.5$ V at a scan rate of 15 mV/s in 6M KNO_2 with the pH held at 7.4 using a phosphate buffer. As evident in the CV shown in Figure 5.14, two peaks corresponding to the step-wise oxidation of NO_2^- anions followed by their chemisorption to defects and dangling bonds on the SWNT sidewalls and tube ends respectively, are observed. At voltages above $+1.0$ V (versus SCE) decomposition resulting in oxygen evolution causes the voltammogram to become noisy.

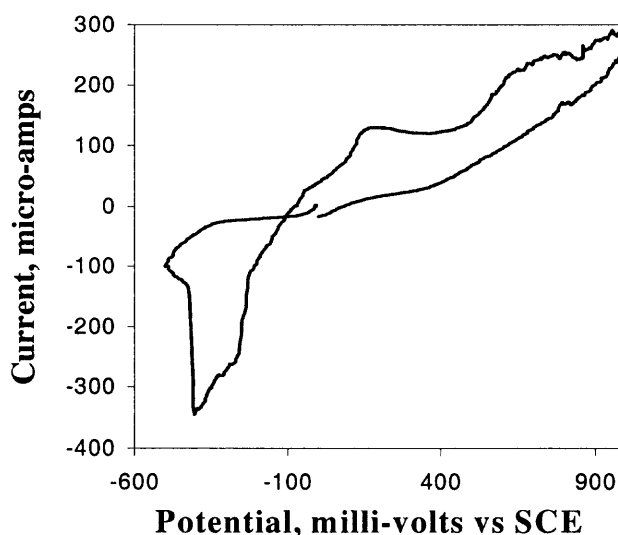


Figure 5.14 The cyclic voltammogram from -600 to $+1000$ mV versus a standard calomel electrode (SCE) of a SWNT nanopaper working electrode and Pt counter electrode in 6M KNO_2 aqueous solution with 0.1M phosphate buffer (pH 7.4). The scan rate is 15 mV/sec.

A representative micro-Raman spectrum excited with 632.8 nm (1.92 eV) laser radiation of the charged nanopaper electrode displayed in Figure 5.15(b) shows important differences compared to the spectrum of the pristine paper in Figure 5.15(a). The spectrum shown in Figure 5.15(b) is closely similar to spectra taken from at least 20 spots across the sample. The overall intensity of the Raman spectrum after charging is reduced by a factor of 6-7, indicating a reduction in resonance enhancement due to the quasi-one dimensional structure of the SWNTs. The decrease in resonance-enhancement may result from an increase in structural dimensionality and disorder due to the formation of functional groups on the sidewalls and tube ends. Moreover, the intense line at 1588 cm^{-1} assigned to the C-C tangential mode in the pristine sample is down-shifted by 3 cm^{-1} after functionalization. This change, though small, is significant and is highly reproducible. In order to understand this downshift, thermopower measurements were performed on the same or similarly charged samples.

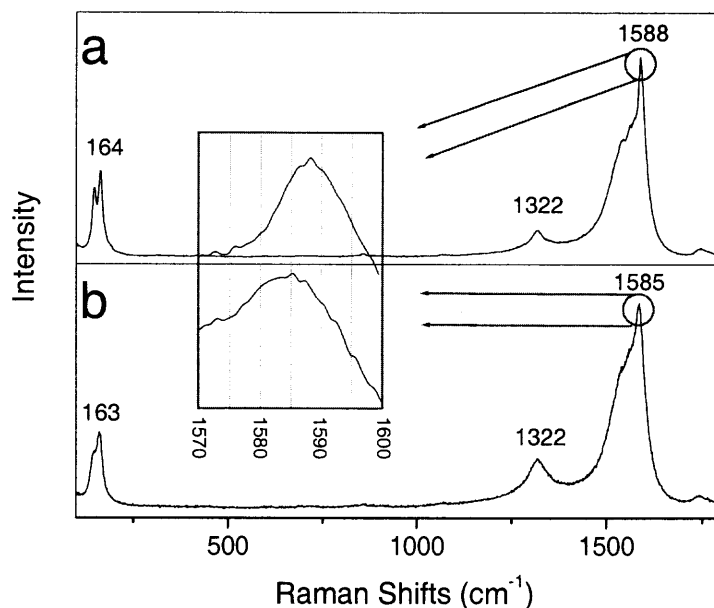


Figure 5.15 Raman spectra excited by 1.92 eV laser radiation of: (a) Pristine SWNT nanopaper sheet, and (b) a SWNT sheet electrochemically charged in 6M KNO_2 at +1.0 V versus SCE.

Pristine SWNTs are uniformly p-doped probably due to the formation of an electron-withdrawing oxygen layer on the tube walls. On electrochemical charging, a 40% reduction in hole carriers is observed, suggesting that electrochemical anodization in 6M KNO_2 results in removal of the oxygen layer followed by release of the negative charges back into the side-walls and tube ends or to the incoming NO_2 radicals to form a C- NO_2 bond. The occurrence of bond formation coupled with charge injection would result in the observed downshift in the tangential mode frequency. There is also an increase in the relative intensity of the broad line centered at 1322 cm^{-1} with electrochemical charging [see Figure 5.15(b)]. This line is largely associated with disorder due to defects on the nanotube sidewalls. However, part of its increased intensity may be due to Raman scattering from the symmetric stretching mode (expected to lie in the $1300\text{-}1380\text{ cm}^{-1}$ frequency range [131]) of the $-\text{NO}_2$ groups formed on

functionalization. This is consistent with TEM images of SWNT bundles from the sheets taken before and after functionalization, shown in Figure 5.16. From the images it is evident that the tube sidewalls are fairly uniform in the pristine tubes [Figure 5.16(a)] and become irregular [Figure 5.16(b)] due to disordering associated with functionalization.

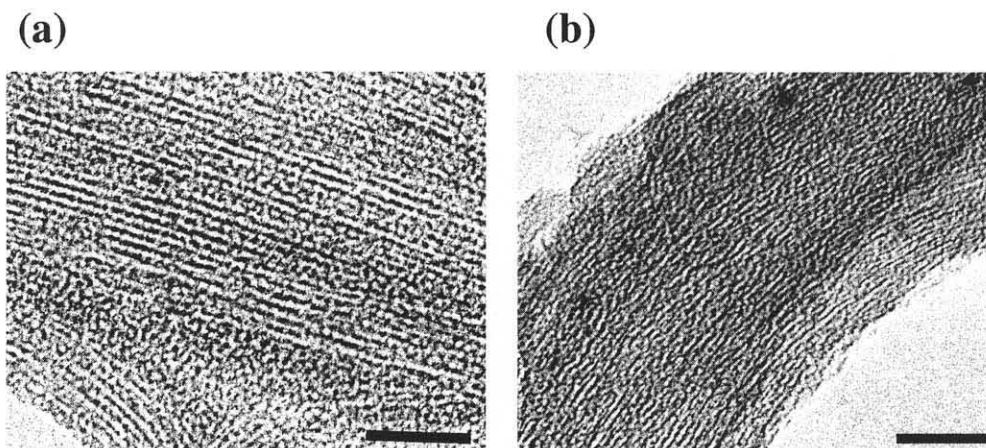


Figure 5.16 (a) TEM image of SWNT bundles taken from a pristine SWNT sheet (scale bar, 20 nm), and (b) TEM image of SWNT bundles taken from an electrochemically functionalized SWNT sheet (scale bar, 20 nm).

Clearer evidence of $-\text{NO}_2$ formation is obtained from the ATR-FTIR spectra. The infrared spectrum in Figure 5.17(a) from the pristine SWNT sample is essentially featureless because of the absence of strong infrared-active modes in SWNTs. Figure 5.17(b) shows the appearance of infrared lines at 1500, 1385, 1330, 1180 and 1100 cm^{-1} in the electrochemically charged sample. The peak at 1500 cm^{-1} can be clearly assigned to the asymmetric stretching mode of $-\text{NO}_2$, where conjugation with the $\text{C}=\text{C}$ carbon nanotube backbone lowers the asymmetric stretching frequency relative to that of unconjugated nitrated compounds [128,131]. The symmetric stretching NO_2 mode is prone to mode mixing and therefore more difficult to assign [128]. Consistent with the Raman spectrum of the charged sample, which shows some increase in intensity near

1322 cm^{-1} [Figure 5.15(b)], the infrared line at 1330 cm^{-1} can be assigned to the symmetric stretching mode of the NO_2 groups formed. The second line in this region of the infrared spectrum at 1385 cm^{-1} can be assigned to the symmetric stretching mode of NO_2 groups attached to tube-end dangling bonds. However, there is no evidence of increased Raman scattering in this region of the spectrum. This is possibly due to the absence of resonance-effects particularly when the functional groups are attached to defects at the tube ends. The higher intensity of the symmetric stretching NO_2 lines in the infrared spectrum relative to the asymmetric stretching line at 1500 cm^{-1} is probably due to Fermi resonance interactions between the two symmetric stretching modes. The lower frequency infrared lines at 1180 and 1100 cm^{-1} can be assigned to C-N stretching modes probably mixed with the NO_2 skeletal modes [128]. These modes are expected to have relatively small Raman cross-sections and are not evident in the Raman spectrum of the charged sample [Figure 5.15(b)]. The appearance of two infrared lines in the 1100 to 1200 cm^{-1} region is also consistent with the possible existence of two attachment sites – one primarily at the tube ends and other on the sidewalls. The presence of two energetically distinct sites on the SWNTs is also indicated by preliminary calculations [132].

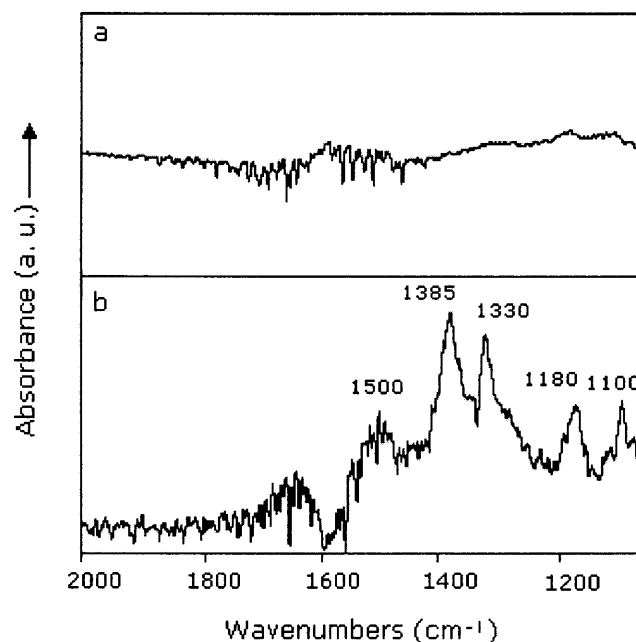


Figure 5.17 ATR-FTIR spectra of: (a) a pristine SWNT sheet, and (b) a SWNT sheet that had been oxidatively charged in 6M KNO_2 at 1.0 V versus SCE.

Additional characterization of the functionalized SWNT sheets was carried out by TGA and DTA techniques for which the data are shown in Figure 5.18. Figure 5.18A shows the DTA data collected at a heating rate of $20^\circ\text{C}/\text{minute}$ for a functionalized sample, and Figure 5.18B shows the TGA data for a pristine and a similarly functionalized sample taken at a slower heating rate. The DTA data show the onset of endothermic dissociation near 425°C associated with the removal of the more strongly bonded $-\text{NO}_2$ groups, probably by C–N bond breaking. The TGA plot for the pristine specimen is essentially flat, whereas weight loss occurs in two steps for the functionalized sample. The observation of two steps in the TGA plot is consistent with the assignment of two binding sites of different bonding strengths based on the FTIR spectra discussed above. A total weight loss of about 25% is observed with an approximately 13% weight loss at high temperature associated with the more strongly bound $-\text{NO}_2$ groups. The latter weight loss can be attributed to the bond breaking

measured by DTA.

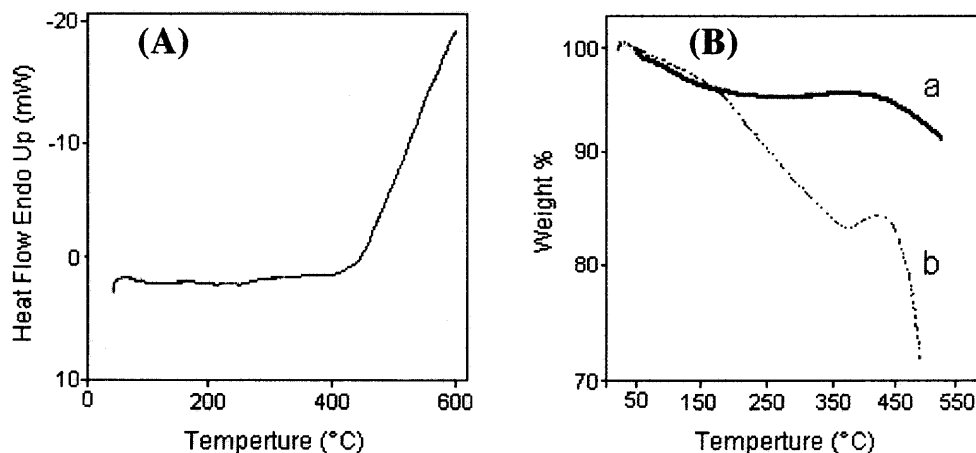


Figure 5.18 (A) DTA data for SWNT nanopaper sheet that was electrochemically charged in 6M KNO_2 at 1.0 V versus SCE. Temperature was increased at a rate of $20^\circ\text{C}/\text{minute}$. (B) TGA data for a pristine SWNT sheet (a) and a SWNT sheet nitrated in 6M KNO_2 at a potential of 1.0 V versus SCE (b). A heating rate of $10^\circ\text{C}/\text{minute}$ was used.

A preliminary investigation of the mechanical properties of nanocomposites prepared with electrochemically nitrated SWNT sheets and chemically nitrated SWNT powder, has been performed [133]. Polyurethane-nitrated SWNT nanocomposites containing 3.8% by weight of SWNTs prepared using a sonication mixing technique and chemically nitrated SWNT powders showed a nearly 47% increase in hardness (and thus a corresponding increase in tensile strength) relative to composites made with the same amount of pristine SWNT powders. Nanocomposite membranes using a solution dipping process with the same polyurethane have been prepared with SWNT sheets used in this study. A factor of 3 increase in hardness was observed for the nanocomposite membranes relative to nanocomposites fabricated using SWNT powders. However, the author did not observe an unambiguous increase in hardness of the nanocomposite sheets prepared with electrochemically nitrated SWNTs relative to the samples prepared from pristine nanotubes. This is likely to be due to higher nitration levels and the formation of $-\text{COOH}$

groups at one of the sites in the chemically nitrated samples, suggesting that optimization of the nitration levels in the SWNT sheets will be required to obtain clear enhancement of the tensile strength.

In conclusion, the author has observed a total of about 25 weight % chemisorption of $-\text{NO}_2$ groups at two sites, by the electrochemical oxidation of a SWNT sheet in 6M KNO_2 solution. An approximately 13 weight % is more strongly bound. Micro-Raman and ATR-FTIR spectroscopy in combination with cyclic voltammetry and thermopower measurements were used to confirm the formation of $-\text{NO}_2$ groups on the SWNTs, and to suggest a qualitative mechanism for the chemisorption process. TEM images and micro-Raman data are consistent with the introduction of disorder on the sidewalls as a result of functionalization.

CHAPTER 6

APPLICATIONS OF SINGLE WALL CARBON NANOTUBES

6.1 Introduction

Single wall carbon nanotubes (SWNTs), with nanometer size, cylindrical and hollow shape, have novel mechanical and electrical properties. Three types of applications of SWNTs based these properties were investigated accordingly. They include applications in hydrogen storage, in the synthesis of ceramic and polymeric composites, and in the fabrication of biofuel cell and biosensor electrodes.

People in the near future will face problems such as shortage of fossil fuels, continuous increase in the world energy needs and environmental pollution. Hydrogen, with the highest energy content per unit weight of any known fuel [66], would be an attractive, clean and efficient energy source of fuel for energy sources such as, proton exchange membrane (PEM) fuel cells. Today, compressed or liquefied hydrogen is used in most cases. This is disadvantageous for safety reasons and the liquefying process is very energy consuming. Extensive efforts have been made to find new hydrogen storage materials. The cylindrical and hollow shape, and nanometer scale diameter of nanotubes suggests that the empty space could be filled with liquid and gas through a capillary effect. In this chapter, the results on electrochemically induced hydrogen storage in pristine as well as in surface-modified SWNTs will be reported and discussed.

The mechanical properties of SWNTs such as their stiffness, elasticity, and high Young's modulus, make them ideal candidates for structural reinforcements in the fabrication of high strength, light-weight, and high performance composites. Both theoretical and experimental works have confirmed that CNTs are one of the stiffest

structures ever made [61]. Theoretical studies have suggested that SWNTs could have a Young's Modulus as high as 1 TPa [81]. Both ceramic and polymeric/SWNT composites have been synthesized in this research and the results will be discussed here. These nanotube-filled ceramic and polymeric composites are expected to be used in many different areas.

With large surface to volume area and the remarkable so-called "ballistic" electrical properties, SWNTs fabricated fuel cell or sensor electrodes have already shown some improvement in sensitivity [97]. In this research, vertically oriented SWNTs grown on conductive Si wafer were functionalized with enzymes for biofuel cell and biosensor applications.

6.2 Electrochemically-Induced Hydrogen Adsorption/Storage in Pure and Functionalized Single Wall Carbon Nanotubes

The vision of hydrogen as a clean and alternative fuel of the future is compelling. Scientists from all over the world have been searching for hydrogen absorbents for decades. The hollow and cylindrical shape, the interstitial sites and nanometer scale diameter of SWNTs suggests that the empty space could be filled with liquid and gas through a capillary effect. The work of Dillon et al indicating 5 to 10 weight % hydrogen storage in bundles of SWNTs in 1997 [69] led to extensive and to date still controversial results [70-76,134,135]. Nützenadel et al reported that 0.39 wt% of hydrogen can be electrochemically stored reversibly in composite electrodes comprising of 0.7 to 1.2 nm SWNTs [70]; Lee et al. predicted theoretically via density-functional calculations that up to 16.7 weight% hydrogen can be inserted in (10,10) SWNTs [71]; and Ye et al. reported

that about 8% of H₂ adsorption can be obtained by high pressure at 80 K on pure SWNT samples [72].

The earlier reports on electrochemical hydrogen adsorption were carried out on SWNTs mixed with metal components, which complicated data interpretation. Here, we report electrochemical hydrogen adsorption/storage in pristine and surface-modified self-assembled SWNT sheets or nanopaper from pure SWNTs obtained via different synthetic routes. The surface modification was performed by paused electrochemical deposition of Co and Mg, and electrochemical deposition of the conducting polymer, polyaniline (PAni). It is expected that Co, Mg and PAni can catalyze hydrogen adsorption on the nanotubes via adsorption at these functionalized sites. Compared with the data from electrochemically hydrogen charged, pristine SWNT sheets, a Mg-functionalized nanopaper sheet charged with hydrogen showed some differences in the Raman spectrum. A Co-functionalized SWNT sheet showed covalent and therefore irreversible C-H bonding after electrochemical charging. Preliminary results indicate hydrogen uptake in PAni functionalized SWNT nanopaper that can be desorbed at temperatures well below 100°C. These results suggest that SWNTs can indeed provide a platform for hydrogen adsorption and storage, particularly if optimized surface tailoring and modification can be performed. Moreover, electrochemical hydrogen adsorption using SWNT electrodes can provide an approach for the reversible storage of humidified hydrogen that can be integrated into a proton exchange membrane fuel cell system. In this chapter hydrogen adsorption results are discussed and quantified by a combination of techniques involving in-situ cyclic voltammetry and ex-situ FTIR spectroscopy, Raman spectroscopy, thermopower measurements, TGA and Prompt-Gamma Activation

Analysis (PGAA) on a sample of pristine SWNT nanopaper that was electrochemically charged with hydrogen.

SWNTs used in this study have been obtained by atmospheric-pressure CO-CVD in our laboratory, high pressure CO-CVD or HiPCO samples obtained from Carbon Nanotechnologies Inc, laser-oven (Tubes@Rice) and arc-grown (Carbolex) SWNTs. The tube diameters from the radial breathing mode Raman spectra ranged from 0.9 to 1.2 nm for the CO-CVD and HiPCO SWNT nanopaper to 1.2-1.3 nm for the laser-oven and arc grown SWNTs. The sample purification and nanopaper self-assembly techniques used were modifications of methods reported in the literature [135].

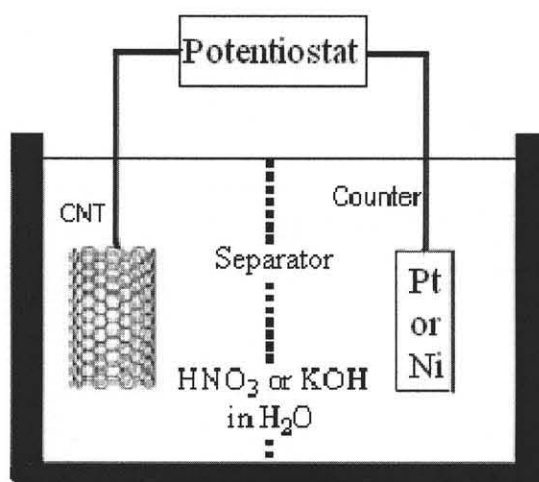


Figure 6.1 Schematic of set-up for electrochemical hydrogen adsorption by electrolysis of water in 6M KOH or 6M HNO₃.

Before hydrogen insertion, the SWNT nanopaper was annealed after slow heat-up to 300°C or 800°C under flowing argon. Scanning and transmission electron microscopy in combination with scanning micro-Raman spectroscopy showed that the nanopaper comprises primarily of bundled SWNTs with small amounts of left over catalyst. Micro-Raman data reported were always checked at various regions of the sample.

Electrochemical charging with hydrogen was carried out using the cell shown schematically in Figure 6.1. A three electrode system in 6M KOH or 6M HNO₃ with a freestanding sheet of nanopaper as the working electrode (cathode), a platinum or nickel foil as the counter electrode and a standard calomel electrode (SCE), was used for the hydrogen adsorption experiments. A computer-controlled 273 EG&G Princeton Applied Research potentiostat-galvanostat was used for charging. The electrochemical deposition of Mg and Co was carried out at the paused potential from -0.7 to -1.0 volts for 20 minutes in 5 mM solution of the corresponding nitrates. The electrochemical deposition of PAn was carried out using a (0.1M) solution of aniline with (0.25 M) oxalic acid as electrolyte. The formation of PAn was confirmed by Raman measurements on the SWNT sample.

Cyclic voltammetry (CV) for pristine and Mg-functionalized nanopaper in 6M KOH for HiPCO, laser-oven and arc-prepared samples showed broad hydrogen charge and discharge peaks at -0.9 and -0.5 volts versus SCE respectively [Figure 6.2(a)]. The CV curve of Co- functionalized nanopaper in 6M HNO₃ showed a number of sharp peaks indicating a relatively complex oxidation-reduction cycle [Figure 6.2(b)]. The CV curve for PAn-functionalized nanopaper showed somewhat broader peaks at -0.5 and -0.3 volts versus SCE [Figure 6.2(c)]. The CV measurements did not show variations dependent on the method used to synthesize the SWNTs.

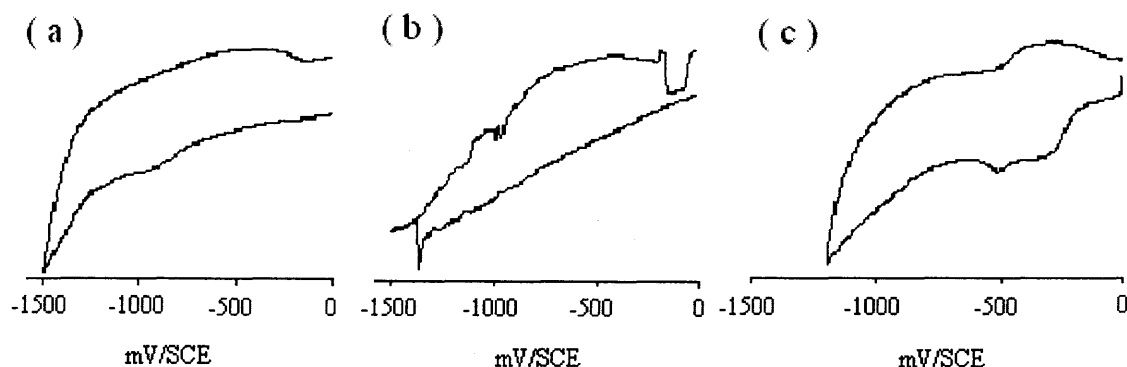


Figure 6.2 Cyclic voltammograms from -1500 to 0 mV versus a standard calomel electrode (SCE) of: (a) pristine or Mg functionalized SWNT sheet in 6M KOH , (b) Co functionalized SWNT sheet in 6M HNO_3 , and (c) SWNT sheet surface coated with polyaniline in 6M KOH . All the scans were carried out at the rate of 10 mV/sec.

Electrochemical hydrogen adsorption on pristine and Mg functionalized SWNT paper was carried out in 6M KOH at about -1.2 volts for 20 hours. For the Co functionalized sample, charging was carried out in 6M HNO_3 at -1.2 volts for the same period of time. TGA measurements on pristine samples, typically showed 2 weight % desorption, with desorption occurring near 125°C . PGAA measurements using neutrons on a similarly treated pristine sample in 6M KOH detected a total hydrogen concentration of 3.2 weight %, but part of this hydrogen may be associated with water adsorbed via nanocapillary effects during the electrochemical insertion process. It must be noted however that pristine SWNT bundles are expected to be hydrophobic. PAN-functionalized SWNT nanopaper showed about 2 weight % desorption at 70°C , which is well below the boiling point of water. This system therefore appears to be very interesting and more detailed studies need to be carried out.

Hydrogen adsorption on the tube walls is complicated by the presence of a surface layer of electron withdrawing oxygen adsorbed on the walls, which gives rise to p-type doping of the semiconducting SWNTs. Thermopower measurements on charged SWNT

nanopaper showed a transition from p- to n- type carriers (an actual change of 63%) due to replacement of the oxygen layer on the tube walls by hydrogen and injection of the electrons back to the SWNT conduction band. Raman data for both pristine nanotube paper and the nanopaper after charging are shown in Figure 6.3. As compared to the tangential mode near 1590 cm^{-1} in the Raman spectrum of the pristine nanopaper, the tangential mode in the charged sample is down-shifted by 4 cm^{-1} , which indicates that charge from the oxygen layer on the tube walls is being injected back into the SWNTs. This is also in the agreement with thermopower measurements, which showed a change from p- to n-doping on electrochemical hydrogen insertion.

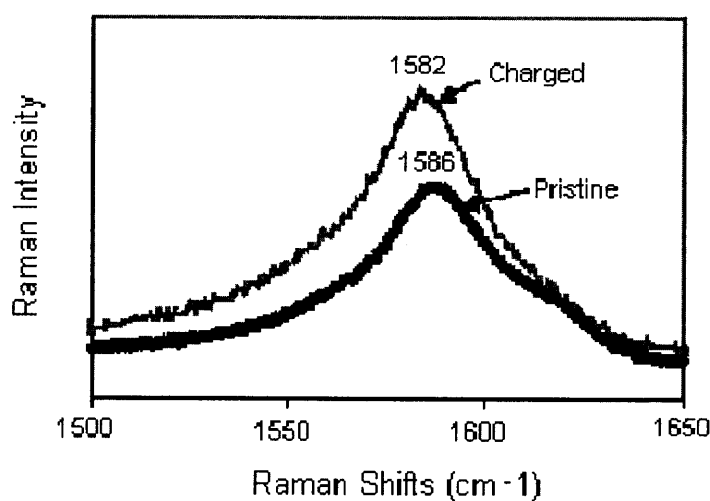


Figure 6.3 Tangential mode Raman line in pristine nanopaper prepared by high pressure CVD and after charging electrochemically for 20 hrs at a potential of -1.2 volts versus SCE in 6M KOH.

The Raman spectrum of Mg-functionalized nanopaper showed downshifts of the C-C tangential mode after charging that are similar to those for similarly charged pristine samples, except for a sizable decrease in the intensity of the tangential mode band envelope (Figure 6.4a), probably due to increased disorder. The TGA measurements (Figure 6.4b) showed a 2 to 2.5% desorption step at about 125°C . The downshift of the

tangential mode frequency in the Raman spectrum and the observed change of thermopower by 60% due to change from p- to n-type carriers, suggests that the hydrogen uptake in the Mg functionalized sample is similar to that in the pristine samples in contrast to previously reported preliminary work [136], which had indicated hydrogen uptake of 4 weight % after a correction for the exposed sample used for the TGA measurement.

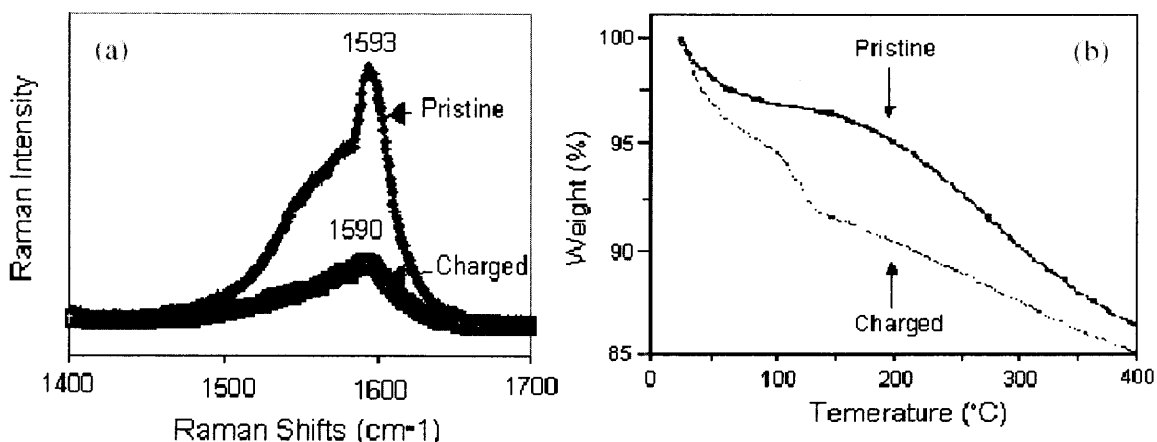


Figure 6.4 (a) Raman spectra of Mg functionalized nanopaper before and after charging in 6M KOH. (b) TGA data from the sample (heating rate 10°C/min)

Cobalt-functionalized samples did not show much difference in the thermopower before and after charging in 6M HNO₃, and there is no desorption step in the TGA data. However, it is interesting to notice that the FTIR (Figure 6.5 right side) spectra of the charged sample clearly shows a C-H bond stretching line, indicating that chemisorption had occurred via the catalytic reduction of the nanotube walls. Moreover, larger downshifts of 11 cm⁻¹ are observed in the Raman data probably due to decrease in the C-C bond length with chemisorption of hydrogen.

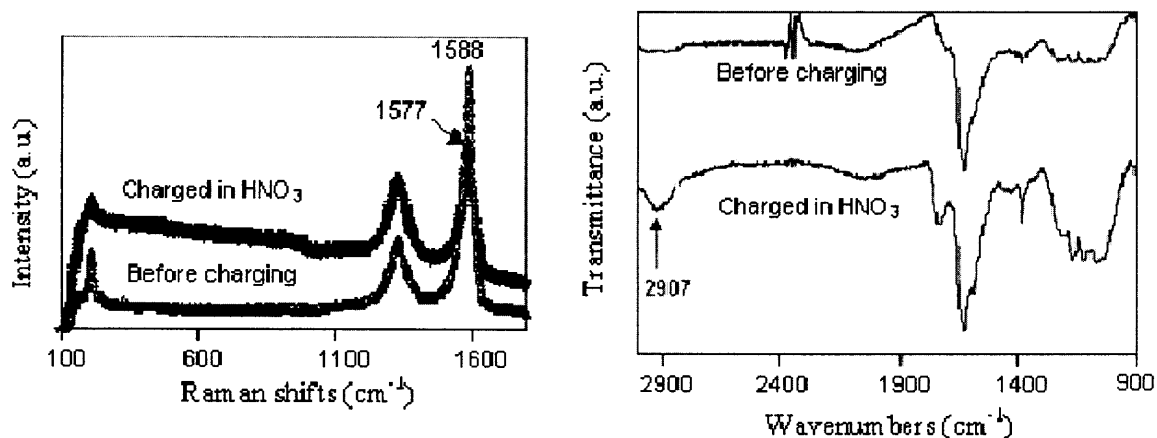


Figure 6.5 Raman spectra of Co functionalized SWNT before and after charging in 6M HNO_3 (left side). FTIR spectra of the sample (right side).

Preliminary results of electrochemical hydrogen insertion in SWNTs with electrochemically formed polyaniline are very interesting. TGA data shown in Figure 6.6c indicates desorption weight loss of 1.5 weight % corresponding to absorption of hydrogen in the charged sample. Desorption occurs at 70°C indicating that it is not associated with water uptake in the sample. The charging was carried out at -0.6 V for about 50 minutes, and as compared to the pristine nanotube sheet of Figure 6.6a, there was about 1.5 % weight loss in the electrochemically charged sample. In addition, the polyaniline functionalized graphite did not indicate any hydrogen desorption in the TGA data shown in Figure 6.6b.

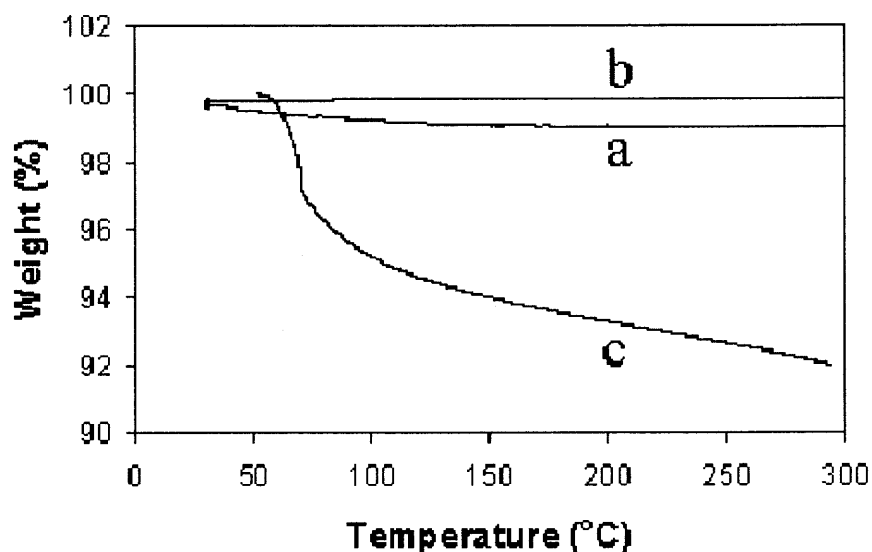


Figure 6.6 The TGA data of: (a) annealed pristine SWNT sheet, (b) polyaniline functionalized carbon paper after electrochemical charging in 6M KOH for 50 minutes, (c) polyaniline functionalized SWNT sheet after charging in 6M KOH for 50 minutes.

In conclusion, the present electrochemically-induced hydrogen adsorption studies indicate 1.5 to 2.5 weight % hydrogen uptake in a range of pristine and functionalized SWNT nanopaper samples and appears to be independent of the method used to prepare the SWNTs. The results suggest that hydrogen storage in single wall carbon nanotubes is a potentially viable technology, but more work is needed to understand the electrochemical hydrogen uptake mechanism. This is being addressed in our group by in-situ Raman spectroscopic measurements coupled with more detailed investigation of the PAn-SWNT system.

6.3 Single Wall Carbon Nanotubes Reinforced Ceramic and Polymer Composites

6.3.1 Rapid, Low Temperature Microwave Synthesis of Novel Carbon Nanotube-Silicon Carbide Composite

Single wall carbon nanotubes (SWNTs) have excellent mechanical, thermal and electrical properties. It has therefore been postulated that ceramic and polymer nanocomposites containing SWNTs will lead to significant enhancement of these properties [81,137]. Desirable properties for ceramic composites include mechanical toughness, wear resistance, and the reduction in crack growth coupled with improved thermal conductivity, resistance to thermal shock and increased electrical conductance. For example, the ceramics are inherently brittle and the incorporation of SWNTs is known to have improved toughness by as much as 24% [138].

Significant efforts have gone into theoretical and experimental investigations of SWNT-based composites [81-83,137-147], but challenges in fabrication, particularly for ceramics and metals have not been overcome. Fabrication methods such as, hot pressing, sintering, milling, covalent grafting and in-situ catalytic growth in ceramic matrices via chemical vapor deposition (CVD), have been used. These methods may be classified as those where the SWNTs and the ceramic were physically mixed and then bonded by heat-treatment, or those where the nanotubes were grown in a ceramic matrix via CVD. This in many cases reported in the literature generates a mixture of single and multiwall nanotubes along with amorphous carbon. As an example of the former approach, Al_2O_3 /nanotube composites were prepared [148] by ball milling a methanol suspension of the ceramic and nanotubes for 24 hours. An example of the latter is the synthesis from the slurry of SiC and ferrocene in xylene, which was sprayed into a reactor at 1000°C under argon [138]. The observed ineffective utilization of SWNTs as the reinforcing material in

many of these composites has been attributed to the non-uniform dispersion of SWNTs, and the poor interfacial adhesion to the matrix. The latter results in ineffective load transfer across the nanotube/matrix interface, and the “pullout” of carbon nanotubes has been observed when the composite is under strain [149]. An important issue has been the high temperature and reactivity of some of the current methodologies, which can destroy and/or damage the SWNTs.

The author believes that the interfacial bonding can be improved by in-situ growth of the ceramic on the SWNT rather than by adding the SWNT onto a pre-prepared ceramic. The composite thus formed will have significantly different properties compared to those made by other techniques. Thus the author investigated and report a rapid, low temperature microwave-induced, approach [127] which formed a unique silicon carbide-SWNT composite with a novel hierarchical structure. This was examined by a combination of infrared and Raman spectroscopy, x-ray diffraction, and electron microscopy. The reaction involves the microwave-induced decomposition of chlorotrimethylsilane in the presence of SWNTs.

To reduce/eliminate residual metal catalyst and to generate $-COOH$ groups, the SWNTs were first treated in nitric acid solution for few minutes under the microwave [127]. In a typical composite forming reaction, about 10 mg of the pretreated SWNTs and 5 ml of chlorotrimethylsilane were added to the microwave reaction vessel. At the same time, another 5 ml of chlorotrimethylsilane was used as the control in a separate vessel. Both the vessels were subjected to microwave induced reaction for 10 minutes, with the power set at 75% of a total of 900 watts, and the pressure set at 125 psi. Once cooled, the liquid in the control vessel remained clear, but a tree-like solid composite was observed

standing in the reaction solution. It was carefully removed from the reaction chamber, washed with chloroform, ethyl alcohol, and distilled water. After air drying over night, the composite weighed about 70 mg.

Chemistry under microwave radiation is known to be somewhat different, faster and more efficient [110-112] as compared to that under conventional thermal reaction conditions. In some cases, even a reduction in activation energy has been reported [117]. Microwave-induced reactions may therefore provide favorable kinetics and make reactions possible that would not be expected to occur otherwise. Under our reaction conditions, a gray-black solid with a branched structure as shown in the optical image in Figure 6.7A and 6.7B rapidly precipitated out of the fine suspension. The composite was between 2 to 4 cm each in length, width and height. It was probably restricted by the size of the reaction vessel. The bulk structure was strong enough to be handled manually. The reaction was found to be highly reproducible; a solid composite of similar morphology, shape, color was obtained every time.

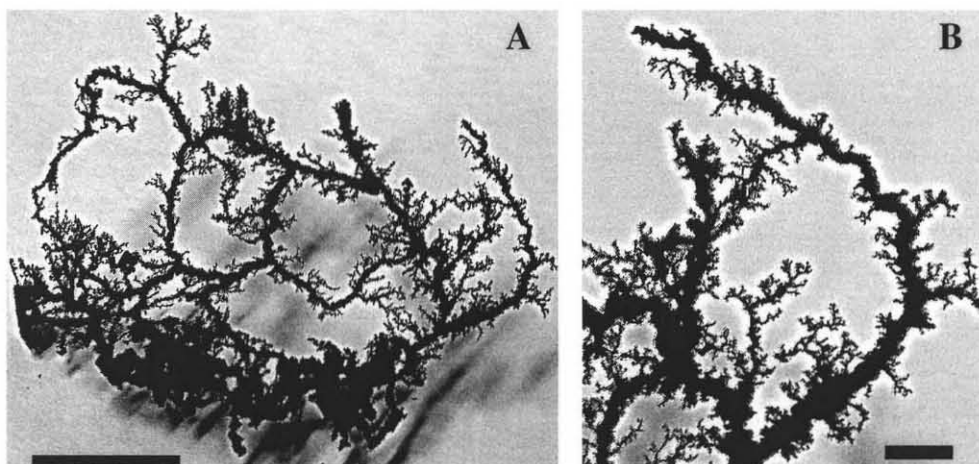


Figure 6.7 Optical pictures of the SWNTs and SiC composite. (A) Whole composite. Scale bar, 1 cm. (B) Magnified portion of the composite. Scale bar, 2 mm.

EDX analysis detected four elements in the composite: C, Si, O and Cl, with atomic compositions of 55%, 33%, 9%, and 3% respectively. This indicated a composite composition of 65% of SiC, 15% of SWNTs and 15% of SiO₂ by weight, assuming that all the oxygen was incorporated in SiO₂. The relatively small amount of chlorine might have been from absorbed chloro-trimethyl silane that remained after the washing and drying. X-ray diffraction (XRD) scan of composite was performed using an area detector and a rotating anode x-ray generator equipped with a graphite monochromator (Cu K α ; $\lambda=1.5418$ Å). The composite was finely ground prior to the XRD scattering. The presence of nanocrystalline SiC is clearly indicated by the XRD pattern displayed in Figure 6.8, which shows the (111), (220) and (311) reflections of face-centered-cubic SiC [150] at 2θ values of 35.6, 60.2 and 71.7 degrees, respectively. The presence of amorphous SiO₂ is indicated by a broad shoulder near 22 degrees.

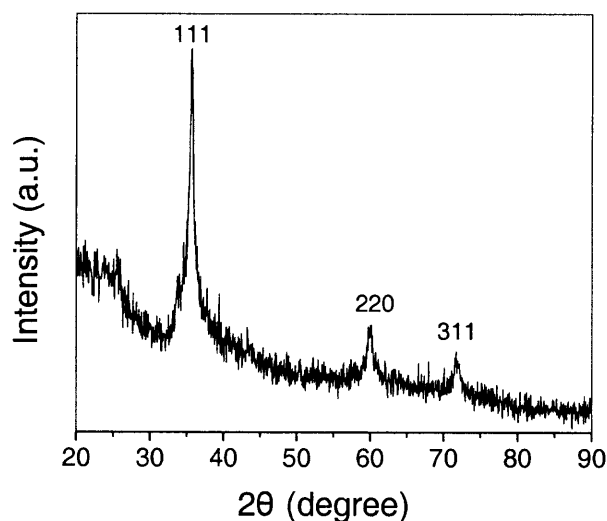


Figure 6.8 XRD of SiC-SWNT composite.

The FTIR spectra of the starting material, the final composite and the chlorotrimethyl silane in the control vessel are shown in Figure 6.9. Without the SWNTs, the chlorotrimethyl silane in the control vessel remained unchanged under microwave

irradiation, and its spectrum was identical to that of the starting material, which is shown in Figure 6.9b. The FTIR spectrum from the nitric acid purified SWNTs is shown in Figure 6.9a. The carboxylic (-COOH) groups generated during the purification process gave rise to the line at 1730 cm^{-1} due to the C=O stretching mode. However, the COOH groups were absent in the composite as shown by the spectrum in Figure 6.9c. A strong, relatively broad Si-C stretching line was seen at 838 cm^{-1} . In addition, on comparing the spectrum of chlorotrimethyl silane (Figure 6.9b) with that of the composite, it was observed that the C-H stretching mode lines at 2965 cm^{-1} and 2902 cm^{-1} and the different Si-C stretching and rocking modes at 846 cm^{-1} , 760 cm^{-1} and 660 cm^{-1} , were absent in Figure 6.9c. This indicates the complete cleavage of the SiC-H₃ bonds during the microwave reaction. The weak line at 1052 cm^{-1} in Figure 3c also suggests the formation of small amounts of SiO₂ in the composite. The presence of unreacted chlorotrimethyl silane in the control vessel indicated that the SWNTs were clearly involved in the formation of the SiC-SWNT composite. The absence of -COOH groups in the SiC-SWNT composite suggest that the reaction was initiated at these (-COOH) sites.

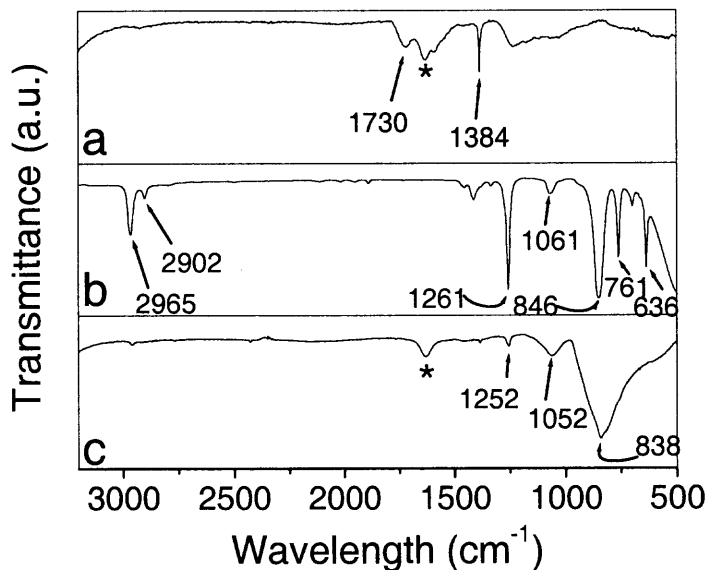


Figure 6.9 FTIR spectra of: (a) purified and acid washed SWNTs; (b) chlorotrimethyl silane; (C) SWNTs-SiC composite. “*” denotes the water impurity from KBr.

Part of the composite was uniformly ground for Raman measurements (Figure 6.10). Maybe due to trace amounts of absorbed chlorotrimethyl silane, the Raman spectrum of the composite was accompanied by some background fluorescence. However, the existence of SWNTs can be seen from both the radical breathing mode and the tangential mode of the Raman spectra. As compared to the pristine SWNTs, the Raman spectra of SiC-SWNT showed a strong increase in intensity of the defect mode, which most likely was due to the increased sp^3 -hybridization induced disorder on the nanotube framework after functionalization [120,121].

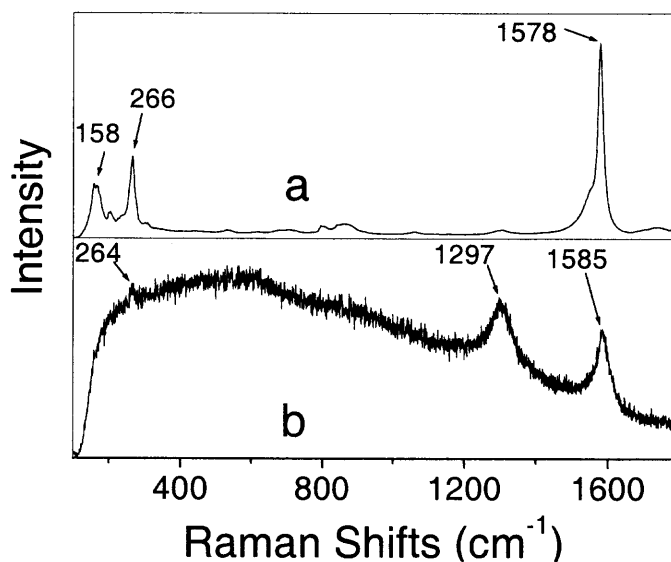


Figure 6.10 Raman spectra of: (a) pristine SWNTs, (b) SiC-SWNT composite.

The SEM images (Figure 6.11) provide insights into how the three dimensional architecture of the composite was formed. As indicated by Figure 6.11a and 6.11b, the nucleation of SiC probably occurred on the SWNT sidewalls at the onset of the reaction. Then, the SiC particles randomly cross-linked (Figure 6.11a) and grew into the macroscopic architecture shown in Figure 6.7. As shown in Figure 6.11c, in certain areas of the composite, the SWNTs were completely covered by the SiC spheres. The image shown in Figure 6.11d is from the surface of a fractured region, and the nanotubes that formed the underlying framework of the composite structure are still embedded. This indicates strong interfacial binding of the SWNTs to SiC. The nanotubes therefore appear to reinforce the composite in a manner similar to steel in reinforced concrete. It is likely that the high tensile strength of the SWNTs prevented their breakage during fracture of the composite.

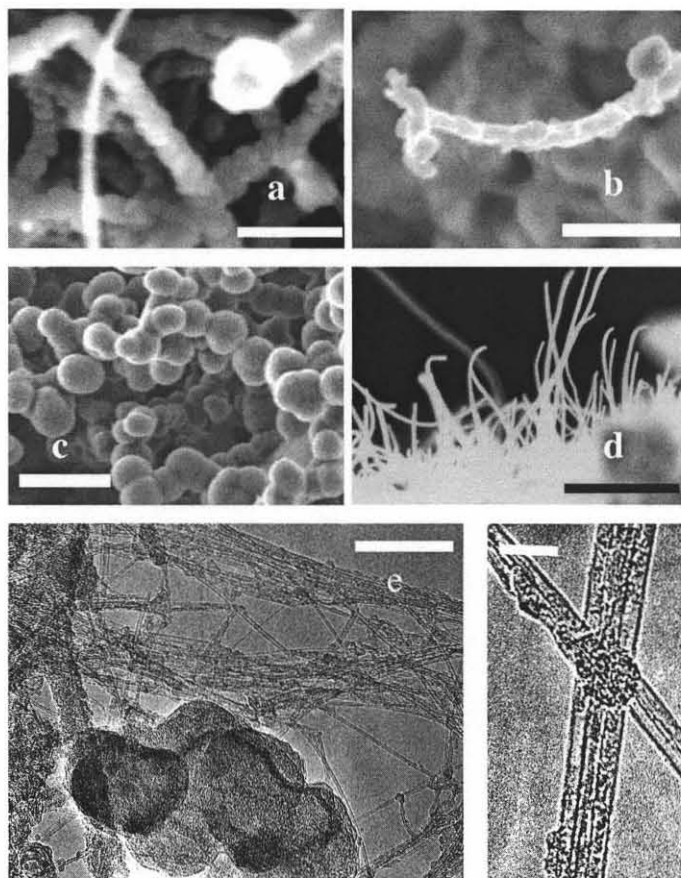


Figure 6.11 SEM and TEM images of SWNTs-SiC composite. (a) SEM image of SWNTs covered by fine SiC particles (scale bar, 200 nm). (b) SEM image showing an individual nanotube covered by SiC particles (scale bar, 200 nm). (c) SEM image showing a portion of SWNTs fully covered by SiC spheres (scale bar, 200 nm). (d) SEM image showing embedded nanotubes from the fractured composite (scale bar, 1 μm). (e) TEM image of debundled, SiC coated SWNTs, and randomly linked by SiC spheres (scale bar, 50 nm). (f) Magnified TEM image showing the SiC coated and linked nanotubes (scale bar, 10 nm).

A small portion of the composite was ground and sonicated in methanol for about 5 minutes. Then a drop of the suspension was cast onto the TEM grid for measurements. The TEM image in Figure 6.11e shows that the SWNTs were debundled and randomly linked by SiC spheres, which are clearly seen at the bottom of the image. A fine coating is observed on the SWNT sidewall in the magnified TEM image in Figure 6.11f. In addition, the SWNTs appeared to be cross-linked. Relatively few SiC particles are seen in

the TEM images because the grinding and sonication during the TEM sample preparation removed some of the loosely held particles.

A proposed mechanism for the growth of the SiC-SWNT composite is shown in Figure 6.12a. The growth appeared to be initiated by the reaction of $-\text{Si}(\text{CH}_3)_3$ at the $-\text{COOH}$ sites by forming HCl and CO_2 . The methyl-silane thus formed was further decomposed by the microwave radiation to produce randomly growing SiC nanoparticles, which covered the nanotube surface and led to the formation of a heterogeneous SiC-SWNT network. The process is shown in Figure 6.12b, a layer of SiC chemically bonded to the SWNT surface, onto which larger SiC spheres grew. The O_2 in the reaction chamber reacted to form small amounts of SiO_2 , which could be etched away by dilute HF.

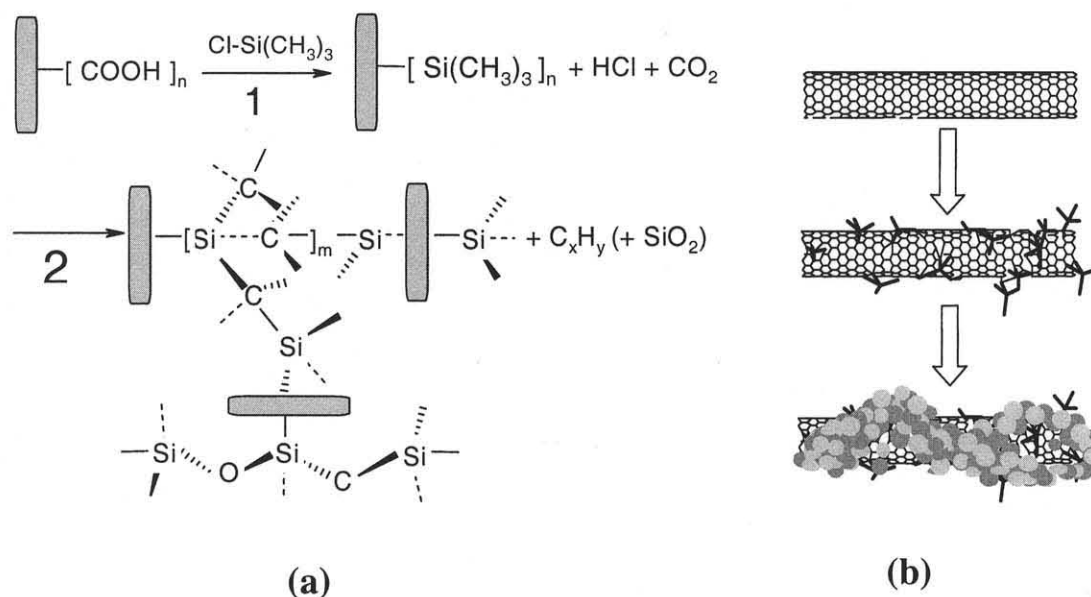


Figure 6.12 Growth of the SiC-SWNT composite: (a) mechanism, (b) pictorial illustration, of the linkage between SiC and SWNTs.

In summary, a novel, low temperature, microwave-induced approach for the synthesis of a high purity SiC-SWNT composite is reported. The reaction, which was

completed in a matter of minutes, involved the nucleation of SiC directly on the SWNT bundles. Formation of multiwalled tubes and other carbonaceous structures usually seen in the reverse approach of growing SWNTs in a ceramic matrix, were not observed here. The composite formed is expected to find applications as a structural and electronic material.

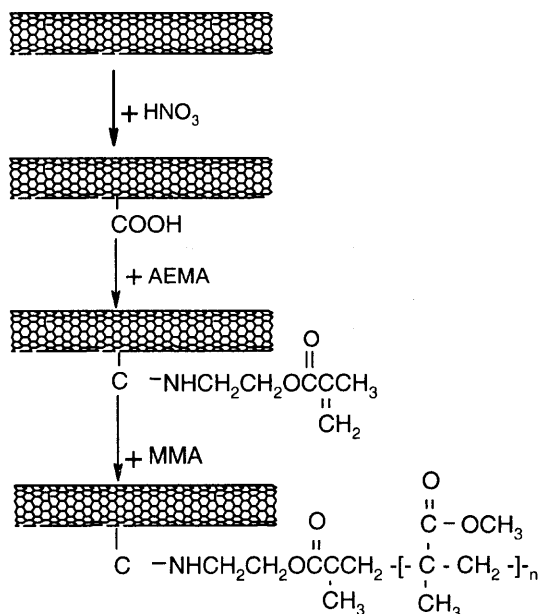
6.3.2 Synthesis of Carbon Nanotube/Poly Methyl Methacrylate (PMMA) Nanocomposite in Supercritical Carbon Dioxide

With the exception of the nanoceramic composites, the synthesis of carbon nanotube reinforced polymeric composites has been investigated world wide as well. The ineffective utilization of nanotubes as reinforcement in composites, caused by non-uniform dispersion of SWNTs in matrix and poor interfacial bonding between them, are the two factors for the ineffective utilization of nanotubes as reinforcement in composites. Recently, several groups reported functionalization of SWNTs with various chemical agents to enhance their interaction with a polymer matrix [121,124,151]. Chemically modified SWNTs possess surface properties that allow them to have enhanced interactions with polymer chains, which greatly improve the composite properties. SWNT surface modification with whole polymer chains has also been reported [152]. However the nature of polymer chains and their usually large molecular weights sometimes make them undesirable candidates for insertion between nanotube bundles. As an alternative, SWNTs have been mixed with monomers, which are then polymerized. The relative high diffusivity of monomers allows them to penetrate into the nanotube bundle matrix and eventually grow into polymers inside the SWNT matrix [124]. Sonication and heating/refluxing were often used as a method to break down

nanotube agglomerates and improve mass transfer during reaction. With the nanotube surface area fixed, the higher diffusivity of the monomers will lead to more polymers in contact with the surface, and a better composite is produced as a result.

In this section of the chapter, the author reports on using supercritical carbon dioxide (scCO₂) as a medium for the synthesis of a carbon nanotube/ Poly Methyl Methacrylate (PMMA) nanocomposite. The principle is functionalization of SWNT surfaces with small molecules containing double bonds followed by in situ dispersion polymerization with vinyl monomers in scCO₂. Dispersion polymerization in scCO₂ has been well studied in the last decade [153]. It has been applied for particle coating [154] and nanocomposite synthesis [155]. In this work, the addition of small molecules onto CNT surface not only make the surface reactive, but also enhances the dispersion of CNT due to the high compatibility of the small molecules with scCO₂. Taking advantage of the extremely high diffusivity and high solvation strength of scCO₂, the reactant (monomer) can reach virtually everywhere in the system, thus the monomer/CNT contact area is maximized.

The SWNTs used in this experiment were obtained from Carbon Nanotechnology Inc. (Hipco process). Carbon dioxide gas was purchased from Matheson with 99% purity. All other chemicals were purchased from Sigma-Aldrich Chemicals, including methyl methacrylate (MMA), poly (dimethyl siloxane) methacrylate (PDMS-MA), 2,2'-Azobisisobutyronitrile (AIBN), 2-aminoethyl methacrylate (AEMA), ethanol, acetone and N,N-dimethyl formide (DMF).



Scheme 6.1 SWNT surface modification followed by in-situ polymerization.

The whole functionalization mechanism is proposed in Scheme 6.1. To generate carboxylic groups ($-\text{COOH}$) and also for removing the catalyst particles remained after production, the received SWNTs were first treated in 70% HNO_3 for 10 minutes using microwave oven [127]. Then, 5mg of the acid treated carbon nanotubes (SWNT-COOH) were refluxed with 20 mg AEMA overnight in DMF. The AEMA modified carbon nanotubes (SWNT-AEMA) were obtained after removing the excess AEMA by slow filtration and washing with 100ml distilled water and 100ml ethanol.

For polymerization, the mixture containing 2ml MMA, 40 mg AIBN, 0.2ml PDMS-MA, and 2 mg AEMA-modified SWNTs was sonicated for 30 minutes in water bath before transferred into a 25-ml cylindrically shaped Parr[®] high-pressure reactor vessel. The mixture was then purged with CO_2 at atmospheric pressure for five minutes. Finally, the vessel was pressurized with CO_2 as heating is also supplied. The final pressure was set at 4200 ± 200 psi, while temperature was at $65 \pm 2^\circ\text{C}$. A detailed description of the

experimental setup and temperature/pressure control can be found in reference [154]. In control experiment, pristine SWNTs were added into the same polymerization mixture.

During this dispersion polymerization, surfactant poly (dimethyl siloxane) –mono methacrylate (PDMS-MA) prevents PMMA from quickly precipitating out due to agglomeration. The polymerization process was visually monitored through two sapphire windows. SWNTs were found to quickly precipitate out at the bottom of the reactor after the pressurization, due to the extraction of other reactants by scCO₂. The polymerization progressed the same way as previous reported [154], e.g. experiencing a transparent-milky-turbid-precipitate transition. After 24 hours of a typical colloid-forming process, a mixture of white (PMMA), black and gray powders (CNTs with PMMA) were collected. To remove PMMA that are physically attached to the SWNTs, the nanocomposite samples were carefully washed three times with acetone, THF, and a combination of both respectively. For a small percentage of the total sample, 20~30ml solvents were used to slowly remove PMMA from the sample on a filter paper during the first two washes. In the third time, the sample was dispersed in 10ml acetone/THF mixture and sonicated for 2 hours at 60°C, followed by a filtration step using 20~30ml solvents.

A sample of the final product was analyzed by FTIR. The nanocomposite surface morphology was examined with FE-SEM. For comparison, all specimens, including pristine and modified carbon nanotubes, were sputter-coated before characterization. To further verify the coating of PMMA onto CNT surfaces, TEM sample was deposited on a 300-mesh copper grid coated with carbon films were used as sample supports.

Samples are mixed with KBr and then pressed for FTIR measurement. Figure 6.13 shows the FTIR spectra of HNO₃ treated SWNT (a), AEMA-modified SWNTs (SWNT-

AEMA) (b), and PMMA functionalized SWNT (SWNT-PMMA) (c). In Figure 6.13a, the peak at 1580 cm^{-1} was assigned to stretching mode of C=C bond, which is close to the defect site of the nanotubes. The C=O band at 1730 cm^{-1} indicated successful generation of COOH on the nanotubes. The sharp peak at 1384 cm^{-1} is probably due to the nitration of SWNTs, which occurred during the high pressure HNO_3 treatment in the microwave [127]. After the attachment of AEMA, the C=O band from the formed amide bond is showing at 1650 cm^{-1} in the enlarged inset in Figure 6.13b. The C-H stretching and bending modes showing at 2911 cm^{-1} and 1434 cm^{-1} provide another prove of the successful reaction between SWNT-COOH and AEMA. The peak at 1730 cm^{-1} from SWNT-COOH is replaced by the peak at 1710 cm^{-1} , which is the ester C=O stretching band from AEMA. In the spectrum of SWNT-PMMA (Figure 6.13c), the peak at 1725 cm^{-1} is mainly from the C=O band of $-\text{COOCH}_3$ groups (Scheme 6.1). Three different C-H stretching bands from the polymer are clearly showing at 2940 cm^{-1} , 2913 cm^{-1} and 2843 cm^{-1} . The peaks at 1259 cm^{-1} from Si-O and at 800 cm^{-1} from Si-C indicate the presence of the surfactant PDMS-MA. It should be noticed that the -MA group of this surfactant allows it to react with MMA and growing PMMA chains.

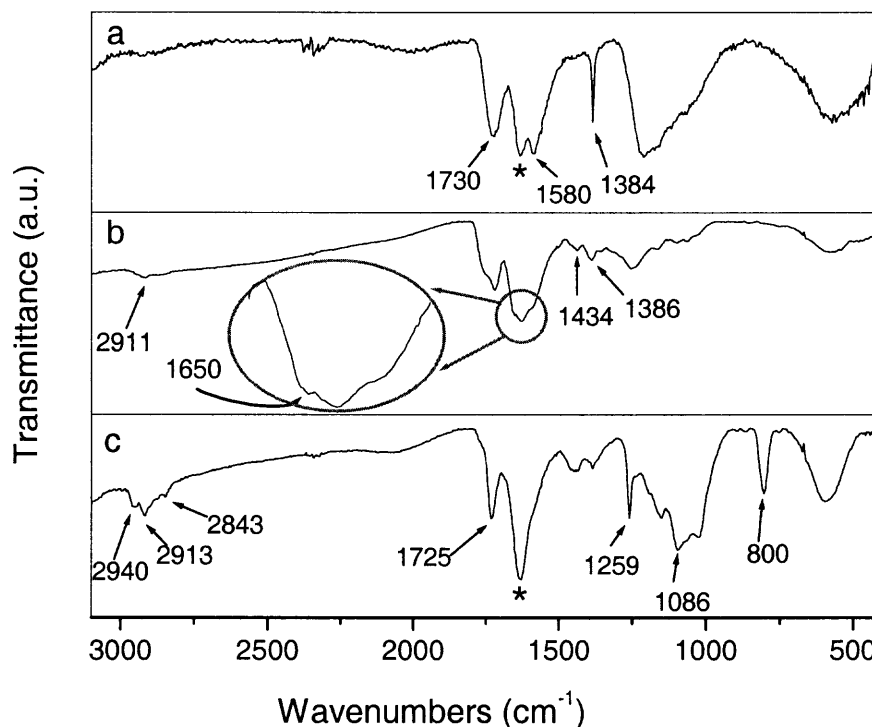


Figure 6.13 FTIR spectra of: (a) SWNT-COOH, (b) SWNT-AEMA and, (c) SWNT-PMMA. (*) denotes the water impurity from KBr.

The SEM images of SWNT-COOH and SWNT-AEMA are shown in Figure 6.14a and 6.14b, and the photo insets in the two images are two samples suspension in polymerization mixture. The photo was taken 15 minutes after both suspensions were taken out of a sonication bath, in which they were sonicated for half an hour. As shown by the photo of SWNT-COOH, aggregation and precipitation were observed immediately after the sonication, which the suspension of SWNT-AEMA remained stable. As comparing to the SEM image (Figure 6.14a) SWNT-COOH, the SEM image (Figure 6.14b) of AEMA modified nanotubes show that lots of area of the nanotube surface and tube ends are covered by some light-color coating, which is an indication of AEMA attachment. The electron conductivity of AEMA is much lower than CNT, so, at the same distance to electron source, the areas covered with AEMA appears brighter on electron micrograph.

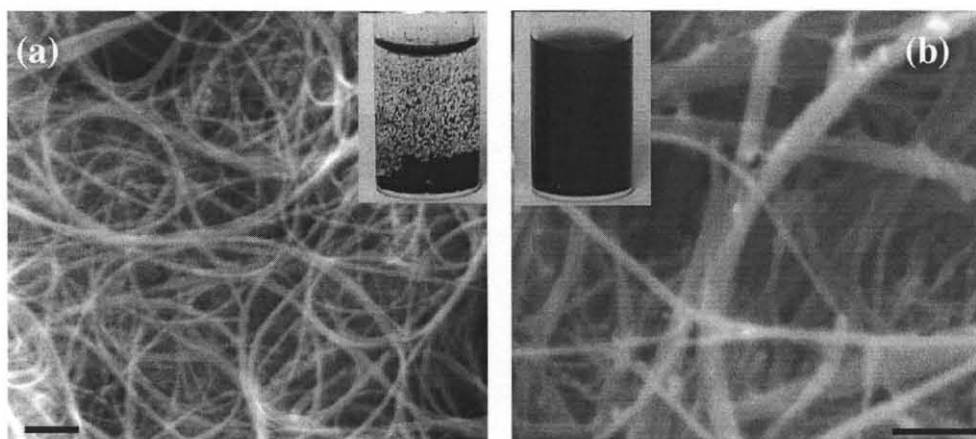


Figure 6.14 SEM images of: (a) SWNT-COOH, scale bar, 100 nm. (inset) photo of the nanotube sample in the polymerization mixture. (b) SWNT-AEMA, scale bar, 100 nm. (inset) photo of the nanotube sample in the polymerization mixture.

Typical PMMA particles synthesized with dispersion polymerization in $scCO_2$ are usually in the size range of hundreds to thousands of nanometers [153]. Particle size and degree of agglomeration can be controlled by varying monomer concentration, surfactant ratio, pressure etc. Shown in Figure 6.15a is a micrograph of pure PMMA sample synthesized under the current polymerization condition. As can be seen, slightly agglomerated particles with primary size of ~ 300 nm were obtained. Shown in Figure 6.15b-d are SEM images of original CNT/PMMA composite samples, in which coexistence of PMMA particles and film coating layer onto CNTs was clearly observed. Unlike loosely agglomerated spherical particles obtained in Figure 6.15a, the PMMA particles are of less regular shape and broad size distribution, and heavily agglomerate with each other, as shown in Figure 6.15 b&c. The polymer coating thickness onto CNT was found to be non-uniform, probably due to the excessive amount of PMMA produced. Figure 6.15d shows the higher magnifications of certain sample points. It was interesting to find small PMMA particles (<100 nm) attached or skewered onto the nanotubes.

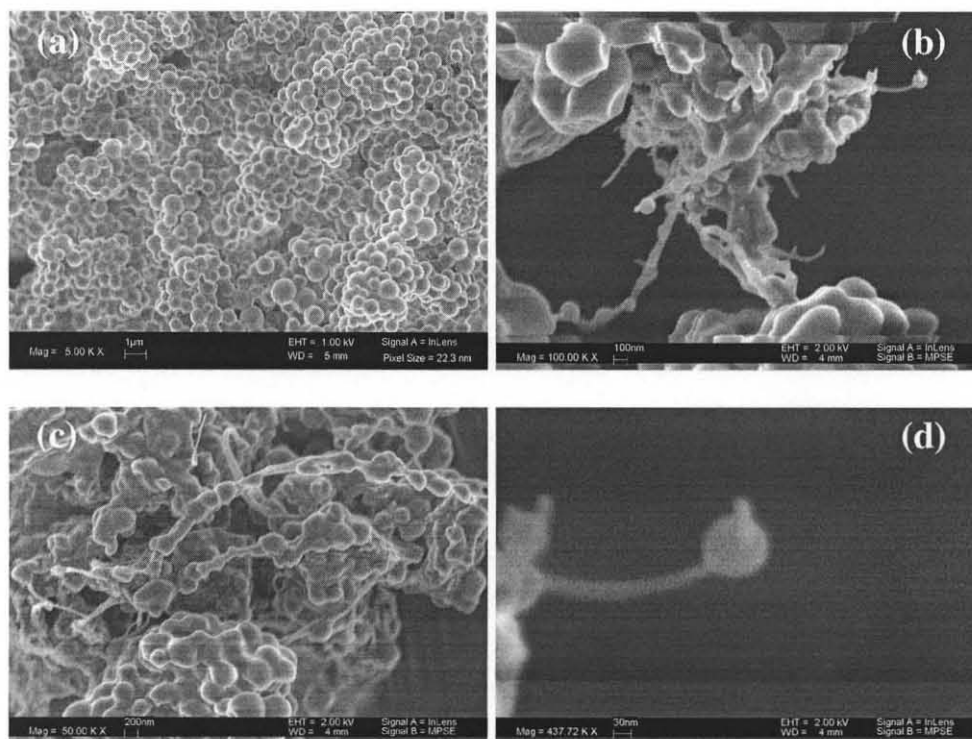


Figure 6.15 SEM image of: (a) PMMA; (b-d) PMMA/CNT composite.

To get rid of the physically attached PMMA, the PMMA/CNT composites were intensively washed with acetone or/and THF. The composites morphology was examined by SEM after each wash. After the first wash, the samples become less agglomerated, as indicated in Figure 6.16. Although the amount of polymer was visually found significantly decreased, a large number of PMMA particles still exist. A detailed examination of the composite surface morphology clearly indicates coating of PMMA onto CNTs, as shown in the insets.

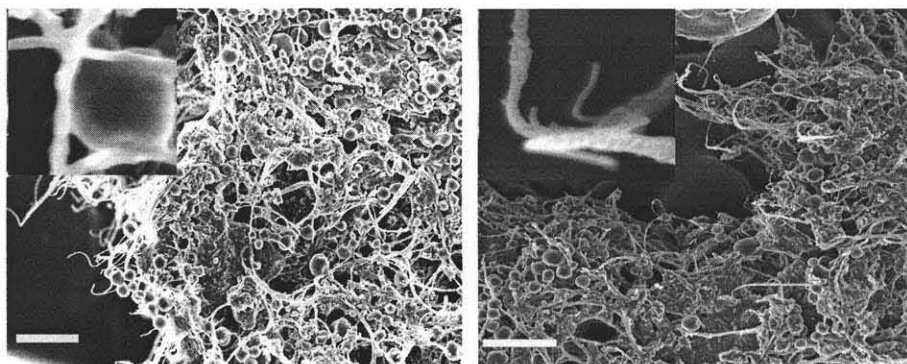


Figure 6.16 Two typical SEM images of the PMMA/CNT composite after first wash with acetone, scale bars, 1 μm . (Insets) magnified portions of the images.

When more polymers were removed, the composite sample appeared more like the assembly of PMMA-coated CNTs. Shown in Figure 6.17a is the sample after a second wash, after which individual polymer particles were completely eliminated. More extraction of polymer with heated acetone/THF mixture under sonication led to samples with morphology. As shown in Figure 6.17b, coated CNTs with diameter of $\sim 20\text{nm}$ were obtained. Such thin coating morphology has rarely been reported in the literature to the best of our acknowledge. The success here is attributed to the extremely high diffusivity and high solvation strength of scCO_2 , which allow the reactants to easily penetrate the CNT matrix throughout the reaction.

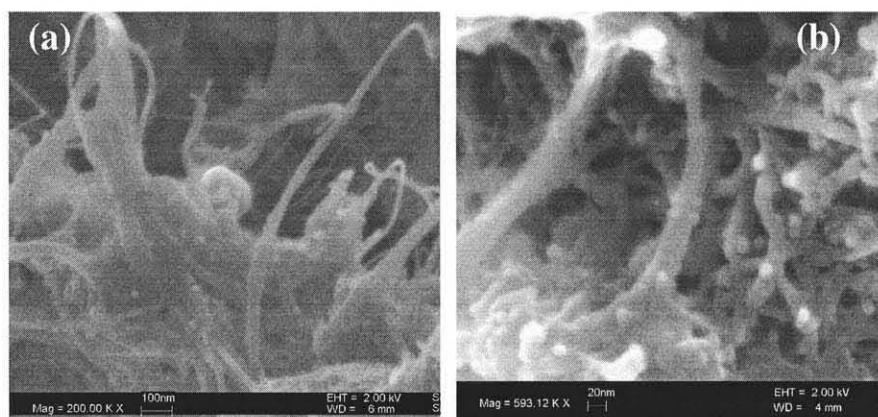


Figure 6.17 SEM images of PMMA/CNT composite: (a) second wash; (b) third wash or more.

TEM imaging was performed on pristine and reacted CNTs after the final wash to give a more detailed picture of PMMA/CNT interaction. Pristine (as bought) Hipco SWNTs existed in bundles and contained some iron catalyst particles (Figure 6.18a). As shown in Figure 6.18b, most of the reacted SWNTs were shown clearly debundled, which might be caused by polymerization in $scCO_2$. The attached polymer is also observable from the sidewalls of each nanotube.

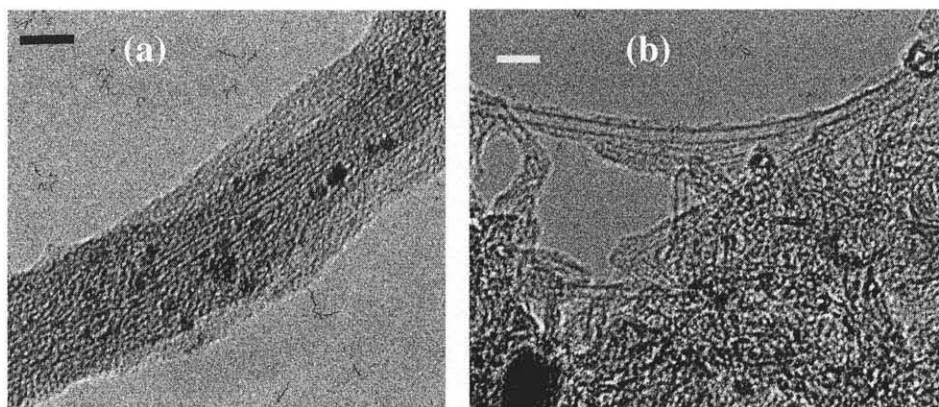


Figure 6.18 TEM images of (a) pristine CNTs, scale bar, 10 nm, (b) reacted CNTs after the third (or more) wash, scale bar, 10 nm.

At the early stage of dispersion polymerization, the formation of oligomer/polymer nuclei follows a mechanism of homogeneous nucleation. In contrast, introducing reactive CNTs with high surface area may induce heterogeneous nucleation. It appeared that polymerization occurred simultaneously in the $scCO_2$ and on the surface of CNTs, where grown polymers developed into a coating layer. This latter mechanism of polymer growth is more like a precipitation polymerization compared to dispersion polymerization due to the fact that the reaction sites are constrained on the immobile solid substrates instead of the dispersed polymer particles growing in the medium. This also explains the heavy agglomeration of PMMA particles, which is typical in precipitation polymerization.

In addition to the heterogeneous nucleation mentioned above, the composite formation mechanism can also be explained using a copolymerization approach, where AEMA-modified CNTs can be regarded as to copolymerize with MMA. It should also be noted that the modified CNTs may function as cross linkers, thus preventing successful stabilization of individual PMMA particles from happening.

In control experiment, composite material was prepared with unmodified CNTs as filler material. As shown in the inset of Figure 6.15a, bare CNTs do not disperse well in the reactant mixture even with sonication. A through examination of the product with SEM indicated that CNTs are primarily present in the form of large bundles. This is another indication that modification with AEMA helps CNTs to debundle. The bundle surfaces were found to be covered with PMMA, as shown in Figure 6.19. Although it is possible that polymers also formed between individual CNTs inside the large bundles, the CNT/PMMA interaction is not expected to be favorable due to the hydrophilicity difference.

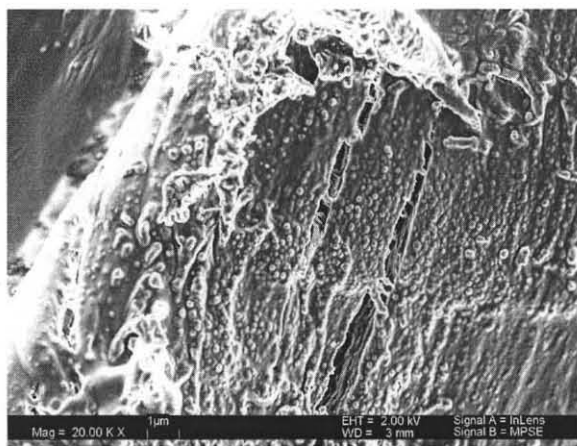


Figure 6.19 SEM image of PMMA coating of unmodified CNT bundles.

Using the in situ polymerization based method, CNT/PMMA nanocomposite was successfully prepared in scCO₂ in this study. PMMA was found to chemically bonded

onto CNT surfaces through copolymerization with AEMA molecules. Excellent surface coverage of CNTs with PMMA throughout all samples was achieved, thanks to the superb diffusivity and solvation strength of scCO₂, which allow complete wetting of CNT surfaces with reactants. Surface functionalization with AEMA was found to be critical to the success of nanocomposite synthesis, due to the lack of debundling of CNTs and possibly unfavorable interaction between hydrophilic CNT surfaces and hydrophobic monomers. The success of functionalization of CNT with PMMA using this method can be generalized to various other polymers.

6.4 Applications of Vertical Oriented Single Wall Carbon Nanotubes in Biofuel Cell and Biosensor

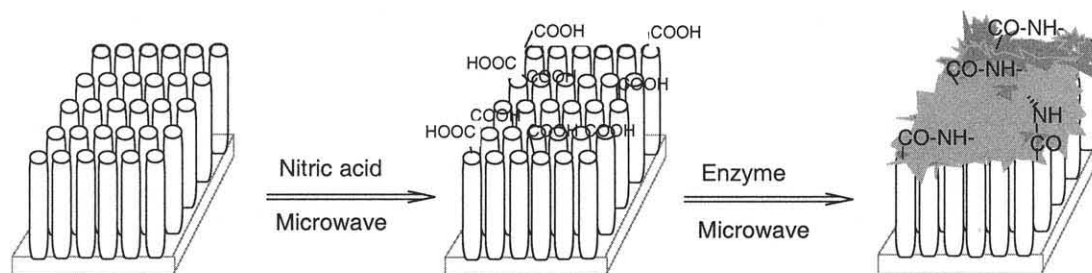
Fuel cells are expected to be a prime candidate for environmentally friendly electric power generation technology. One of the challenges in conventional, proton exchange membrane (PEM) fuel cells is the high cost of the noble metal Pt catalyst. The utilization of multiwall carbon nanotubes as the catalyst support to reduce the usage of Pt has been reported, and higher electrocatalytic activity was observed from the fabricated nanotube-based electrode [156,157].

Biofuel cells are an attractive alternative to conventional fuel cells, because they eliminate the dependence on precious metal catalysts by replacing them with biological catalysts, such as enzymes [158]. Also, there are more choices of fuels or oxidants for biofuel cell applications. For example, glucose, alcohol and lactate can all be used as fuels. Furthermore, biofuel cells can be operated at ambient temperature or lower, which make them useful as implantable power for medicinal applications.

Carbon nanotubes, especially single wall carbon nanotubes (SWNTs), have remarkable structural, mechanical and electrical properties, and the similarity in length scales with redox enzymes. These novel properties of SWNTs suggest that they may be favorable for biofuel cell and biosensor electrode applications. In fact, direct electron transfer of glucose oxidase on carbon nanotubes have been observed and reported by different research groups [97,159]. In this research, vertically oriented SWNTs grown on a conductive, doped Si wafer were used as electrodes for biofuel cell and biosensor applications. The growth and characterization of oriented SWNTs were discussed in Chapter 4.

Two methods were used to attach the enzymes onto the vertically oriented SWNTs. These included electrochemically-induced and microwave-induced reactions. For the former, the functionalization with the enzyme, β -NAD (nicotinamide adenine dinucleotide) synthetase was carried out in a three-electrode cell, with 0.1 M of KCl as the electrolyte. The reaction was carried out in 80 ml of pH 7 phosphate buffer (40 mM) with 50 mg of the enzyme. A Si wafer with oriented SWNTs was used as the working electrode, with a platinum wire as counter electrode and a saturated calomel electrode (SCE) as reference electrode. Cyclic voltammetry (CV) was carried out at a scan rate of 50 mV/s in the range between -1 volt to 1 volt using a computer-controlled Elchema PS-205B potentiostat-galvanostat. After reaction, the SWNT electrode was rinsed with distilled water and dried in air. The microwave reaction is illustrated as Scheme 6.2. In order to have carboxylic acid groups react with enzymes, vertically aligned SWNTs grown on a silicon wafer were immersed in a thin layer of 70% nitric acid. The wafer was then placed in a microwave oven and reacted for 2 minutes using 90 W of microwave

power in an open vessel reaction. Excess nitric acid on the SWNTs was washed off with DI water. Carboxylic (-COOH) groups are expected to be generated at the tube ends as a result of this reaction. For preparing the anode, a couple of drops of glucose oxidase (GOx) solution (1 mg dissolved in 3 drops of water) were drop-coated onto the nitric acid treated nanotubes. After drying in air, the whole substrate (with nanotubes and enzyme) was reacted under microwaves for 2 minutes at a power of 45W using a dry medium reaction. This results in covalent attachment of the enzyme to SWNTs via the amidation reaction as shown by previous chemical functionalization studies (Chapter 5). The excess enzyme was rinsed off using DI water. The same anode was used for a preliminary demonstration of biosensor activity. Using similar reaction conditions, the enzyme bilirubin oxidase (BOD) was used to prepare the cathode for demonstration of a liquid electrolyte biofuel cell.



Scheme 6.2 Schematic illustration of the microwave functionalization of SWNTs.

A Si substrate with oriented SWNTs obtained using the dip-coating catalyst/promoter method (for details see Chapter 4) was used to electrochemically react the SWNT tips with the enzyme, β -NAD synthetase. The reaction was carried out for 10 scan cycles between -1 V to $+1$ V. The CV curve was reproducible for each scan. As shown in Figure 6.20, the CV indicates an irreversible oxidation peak at $+0.39$ V, which

can be attributed to the oxidative attachment of the enzyme, possibly at the tube ends of the vertically aligned SWNTs.

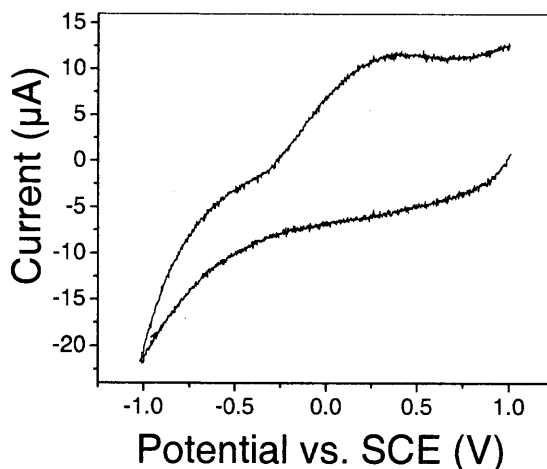


Figure 6.20 Cyclic Voltammogram of oriented SWNT film on silicon with 50 mM β -NAD synthetase in pH 7 phosphate buffer. Scan rate, 50 mV/s. Further details are provided in the text.

The SEM images in Figure 6.21 show the top view of the oriented SWNTs before and after electrochemical functionalization with β -NAD synthetase. The oriented SWNTs were about 2 to 3 μm in length, and closely packed on the Si wafer (Figure 6.21a). Figure 6.21 shows a typical SEM image from the enzyme functionalized SWNT films. The bottom half of the image, which shows lighter contrast compared to the top half of the image, is from the enzyme functionalized SWNTs. The enzyme appears to be uniformly attached to the oriented nanotube ends. However, some enzyme aggregation was found in some spots, as evident from the higher magnification image in Figure 6.21c.

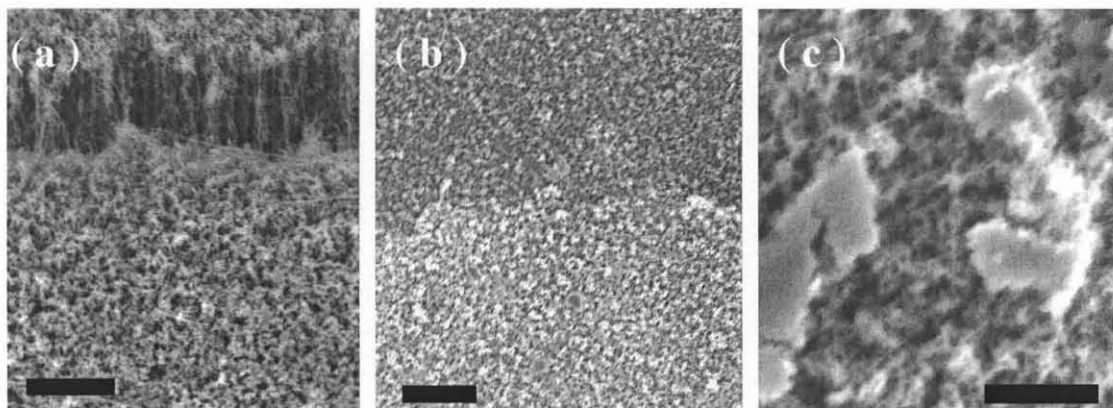


Figure 6.21 SEM images of pristine and enzyme-functionalized, oriented SWNT film on silicon: (a) Pristine oriented SWNTs, Scale bar, 1 μm . (b) SEM image showing reacted (bottom) and unreacted (top) film, Scale bar, 2 μm . (c) Higher magnification SEM image of the enzyme reacted SWNTs showing the lighter contrast enzyme particles on top of the darker tube ends of the SWNTs. Scale bar, 500nm.

The functionalization of SWNTs via the electrochemical approach was found to be simple and straightforward. However, this technique normally requires relatively large amount of enzyme, and would dramatically increase the cost when expensive enzymes need to be employed. In addition, the exact reaction linkage or chemisorption between the SWNT and enzymes is unclear. On the other hand, the microwave functionalization technique consumes only a small amount (order of milligrams or less) of enzyme, and the reaction is fast.

As shown in Figure 6.22, two electrodes made by the microwave reaction technique were tested in preliminary experiments using a fuel cell setup with a liquid electrolyte [160]. The anode consists of GOx functionalized, oriented SWNTs on Si, and the cathode is comprised of oriented SWNTs functionalized with bilirubin oxidase (BOD). 100 mM of pH 7 phosphate buffer was used as the liquid electrolyte. Without the addition of any oxidant between the two electrodes, a maximum current of 40 nA (1 cm^2 working area) and a maximum open circuit voltage of 280 mV were detected. After

addition of β -D-glucose (100 mM concentration) the output was increased to about 80 nA current and 480 mV open circuit voltage, indicating fuel cell action. However, we have not measured the polarization curve under load conditions because of the high resistivity of the silicon wafers available. These measurements will be performed in continuing studies in our group using more conductive silicon or metal coated substrates.

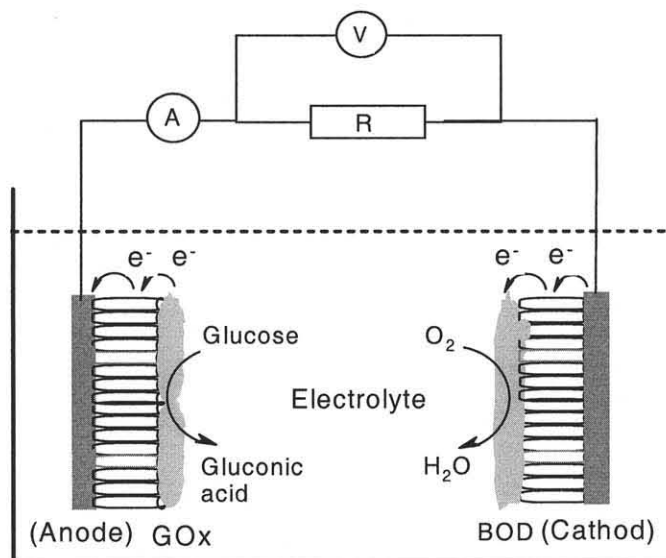


Figure 6.22 Schematic illustration of the fuel cell set up.

Some preliminary results regarding the utilization of the oriented SWNTs in sensing application have also been obtained. Shown in Figure 6.23 is the schematic set up of a glucose biosensor. The working electrode is the same anode as used in the fuel cell applications. At the same time, a saturated calomel electrode (SCE) was used as reference electrode, and platinum was used as counter electrode.

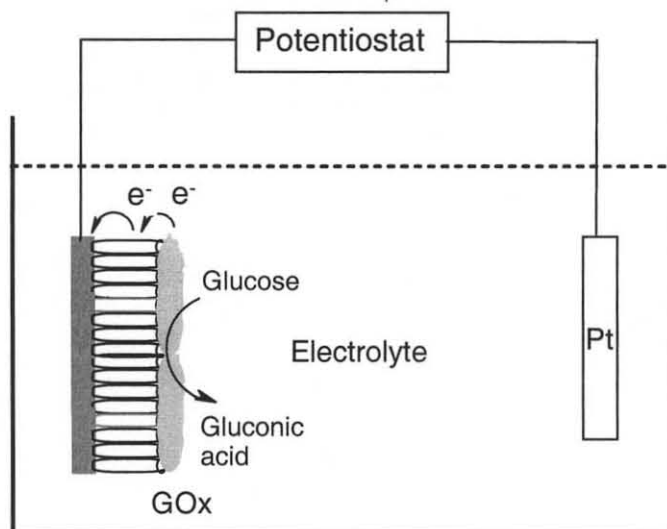


Figure 6.23 Schematic set up of a glucose biosensor.

The working area of the working electrode is about 0.5 centimeter square. The electrode was first tested 100 mM pH 7 phosphate buffer. The obtained cyclic voltammogram (CV) is shown in black in Figure 6.24. May be because of the presence of oxygen or other impurity in the buffer, the CV curve is little noisy and irregular. However, the direct electron transfer is clearly indicated by the peak at 0.3V (or 15 μ A), and this would indicate the electroactivity of the fabricated electrode. More importantly, the CV curve (red) in Figure 6.24 shows that there is a sizable increase in current after the addition of glucose (total concentration of glucose is 120 mM). This is in agreement with the data by Guiseppi-Elie's group [97]. The increase in current should be associated with the enzymatic reaction of glucose: $\text{Glucose} \longrightarrow \text{Gluconolactone} + 2\text{H}^+ + 2\text{e}^-$.

This result consequently confirms that the oxidase still maintained its specific enzyme activity.

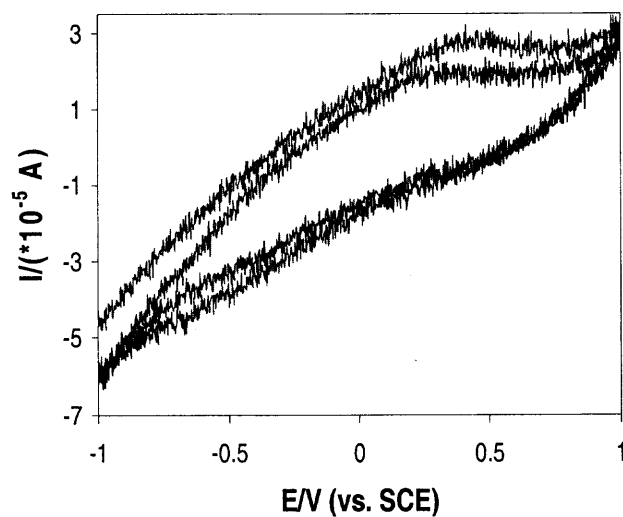


Figure 6.24 CV curves of the electrode in 100 mM pH 7 phosphate buffer: (black) without glucose, (red) with 120 mM glucose. Scan rates, 100 mV/s.

In summary, the utilization of oriented SWNTs in biofuel cell and biosensors has been demonstrated. Preliminary positive results have been obtained for both applications. However, these biofuel cell and biosensor could be greatly improved by using more conductive substrate (other than Si), and by optimizing the enzyme attachment to the electrodes.

CHAPTER 7

SUMMARY

As a new member of the carbon family, carbon nanotubes (CNTs) and especially single-wall carbon nanotubes (SWNTs) show fascinating properties with promising prospects for applications. Their robust structure, novel electronic properties, hollow shape, nanometer size and micrometer lengths make them attractive to researchers in different scientific fields.

Many methods for the synthesis of CNTs have been developed by researchers from all over the world. Here, chemical vapor deposition (CVD) was used for SWNT synthesis. The CVD method offers more advantages than other methods, such as more choices for carbon source, possibility for controlled and oriented growth and *in-situ* fabrication of CNT-ceramic composites. Some aspects of bulk synthesis and details of vertically oriented synthesis of SWNTs have been developed using CVD in the research work for this thesis.

Functionalization is key to obtaining debundled individual SWNTs with a range of wrapped, chemically bonded and tethered functional polymers, biomolecules and chemical groups targeted for specific applications and in some instances to produce soluble CNTs. Other than the modification of a conventional organic reaction approach to produce enzyme functionalized SWNTs, the further development of electrochemical and supercritical CO₂ reactions, and the discovery of microwave assisted SWNT functionalization, have been the most significant achievements of the research conducted for this thesis. The latter approaches are also more environmentally friendly and time-efficient than the conventional reaction approaches.

The chemical functionalization of SWNTs with different functional groups via these approaches was successfully carried out, and many of them were reported for the first time to the best of my knowledge. These include the attachment of enzymes via covalent bonding and the development of the microwave assisted functionalization technique. Notably, the microwave-assisted amidation, 1, 3-dipolar cyclo addition and nitration of SWNTs were all completed on the order of minutes. Further optimization and investigation, as well as detailed quantification of the microwave-assisted reactions need to be carried out going forward.

Utilizing SWNTs for electrochemically-induced hydrogen storage was also investigated in this research. This was done on self-assembled SWNT nanopaper membranes used as the working electrode in an electrochemical cell. The hydrogen storage reactions were carried out on both pristine and catalytic metal and conducting polymer, polyaniline modified SWNT electrodes, and 2~3 wt% of hydrogen storage were consistently obtained, but more work needs to be done to achieve the 6 wt% or better mandated by the Department of Energy for automotive fuel cells. In addition, it is yet to be determined if part of this hydrogen uptake is due to nanoscale capillarity-induced water uptake in the nanotubes. Solid state NMR and in-situ Raman measurements, already in progress in our group, needs to be done in order to clarify this and understand the mechanism of electrochemical adsorption.

The applications of SWNTs for making both ceramic and polymeric composites were also investigated. The composite fabrication was carried out using novel microwave (for ceramic composites) and supercritical CO₂ (for polymeric composites) techniques. The microwave fabrication method provided low reaction temperatures, which protect

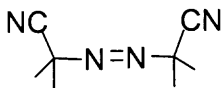
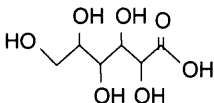
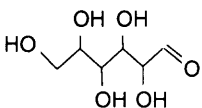
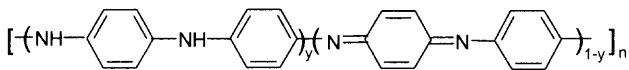
SWNTs from being damaged or oxidized during the composite synthesis reactions. From supercritical CO₂, more uniform coating of polymethyl methacrylate (PMMA) on SWNTs has been achieved. Utilization of vertically oriented SWNTs for biosensor and biofuel cell applications was also investigated and some interesting preliminary results obtained which will be studied in more detail in our group. These results showed that the enzyme, glucose oxidase attached to the tips of oriented SWNTs by electrochemical and microwave techniques were active in the presence of glucose in a biofuel cell and a biosensor arrangement.

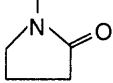
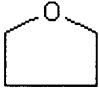
In conclusion, this study represents the first stage of a larger investigation of CNT functionalization for applications in hydrogen storage, biofuel cells, biosensors and the fabrication of a wide range of CNT-based nanocomposites. Much of this research will continue in our group.

APPENDIX

STRUCTURE OF POLYMERS, ENZYMES AND COMPLEX MOLECULES USED

This appendix lists the names and the corresponding structure of the complex molecules used in this research.

Compound	Structure
2-aminoethyl methacrylate (AEMA)	$\text{H}_2\text{C}=\text{C}(\text{CH}_3)\text{CO}_2\text{CH}_2\text{CH}_2\text{NH}_2$
Amino lipase (AK)	N/A
Azobisisobutyronitrile (AIBN)	
Bilirubin oxidase (BOD)	N/A
Citric acid	$\text{HOC}(\text{COOH})(\text{CH}_2\text{COOH})_2$
DMF (N, N-dimethyl formamide)	$\text{HCON}(\text{CH}_3)_2$
Gluconic acid/gluconolactone	
β -D-glucose	
Glucose oxidase (GOx)	N/A
β -NAD (nicotinamide adenine dinucleotide) synthetase	N/A
Polyaniline (PAni)	 <p style="text-align: center;">PANI</p>

Compound	Structure
Poly (dimethyl siloxane) methacrylate (PDMS-MA),	$\text{--[O--Si(CH}_3)_2\text{COOCH}_3\text{]}_n\text{--}$
Polymethylmethacrylate (PMMA)	$\text{--[CH}_2\text{C(CH}_3\text{)(CO}_2\text{CH}_3\text{)]}_n\text{--}$
Polyurethane	$\text{--[NHCH}_2\text{CH}_2\text{NHCOCH}_2\text{CH}_2\text{O]}_n\text{--}$
Polyvinylpyrrolidone (PVP)	$\text{--[CH}_2\text{--CH]}_n\text{--}$ 
Tetrahydrofuran (THF)	

REFERENCES

- [1] Retrieved from the website of Cambridge university engineering department
<http://www-g.eng.cam.ac.uk/cnt/>.
- [2] M. Meyyappan, M. Meyyappan, Carbon Nanotubes: Science and Applications, (2004) chapter 1 P1-23.
- [3] S. Iijima, Nature 354 (1991) 56.
- [4] S. Iijima, T. Ichihashi, Nature 363 (1993) 603.
- [5] C.H. Olk, J.P. Heremans, J. P. J. Mater. Res. 9 (1994) 259.
- [6] P.M. Ajayan, O.Z. Zhou, Carbon nanotubes: Synthesis, Structure, Properties, and Applications, edited by M.S. Dresselhaus, M.S., Dresselhaus, G., Avouris, P. Springer-Verlag, New York. Topic in Applied Physics, 80 (2001) 391.
- [7] M.S. Dresselhaus, G. Dresselhaus, P.C. Eklund, Science of Fullerenes and Carbon Nanotubes (Academic, New York. 1996).
- [8] M.S. Dresselhaus, G. Dresselhaus, P. Eklund, R. Saito, R. Physics World, January, (1998) 33.
- [9] M.S. Dresselhaus, G. Dresselhaus, R. Saito, R. Carbon 33 (1995) 883.
- [10] Z.K. Tang, N. Wang, X.X. Zhang, J.N. Wang, C.T. Chan, P. Sheng, New Journal of Physics 5 (2003) 1-29.
- [11] M. Zhang, M. Yudasaka, S. Iijima, J. Phys. Chem. B 108 (2004) 149.
- [12] P.M. Ajayan, Chem. Rev. 99 (1999) 1787.
- [13] A.M. Rao, P.C. Eklund, S. Bandow, A. Thess, R.E. Smalley, Nature 388 (1997) 257.
- [14] R.S. Lee, H.J. Kim, J.E. Fisher, A. Thess, R.E. Smalley, Nature 388 (1997) 255.
- [15] B.I. Yakabson, C.J. Brabec, J. Bernholc, Phys. Rev. Lett. 76 (1996) 2511.
- [16] B.I. Yakabson, R.E. Smalley, Am. Sci. July-August (1997) 324.
- [17] S. Iijima, J. Chem. Phys. 104 (1996) 1.

- [18] P.M. Ajayan, T.W. Ebbesen, T. Ichihashi, S. Iijima, K. Tanigaki, H. Kiura, *Nature* 362 (1993) 522.
- [19] S.C. Tsang, P.J.F. Harris, M.L.H. Green, *Nature* 362 (1993) 520.
- [20] H. Kataura, Y. Kumazawa, Y. Maniwa, I. Umezu, S. Suzuki, Y. Ohtsuka, Y. Schiba, *Synthetic Metals* 103 (1999) 2555.
- [21] M.S. Dresselhaus, G. Dresselhaus, A. Jorio, A.G. Souza Filho, M.A. Pimenta, R. Saito, *Acc. Chem. Res.* 35 (2002) 1070.
- [22] H. Dai, *Carbon nanotubes: Synthesis, Structure, Properties, and Applications*, edited by M. S. Dresselhaus, M. S., Dresselhaus, G., Avouris, P. Springer Verlag, New York. *Topic in Applied Physics* 80 (2001) 29.
- [23] D.S. Bethune, C.H. Kiang, M. DeVries, G. Gorman, R. Savoy, J. Vazquez, R. Beyers, *Nature* 363 (1993) 605.
- [24] C. Journet, W.K. Maser, P. Bernier, A. Loiseau, M.L. Delachapelle, S. Lefrant, P. Deniard, R. Lee, J.E. Fisher, *Nature* 388 (1997) 756.
- [25] A. These, R. Lee, P. Nikolaev, H.J. Dai, P. Petit, J. Robert, C.H. Xu, Y.H. Lee, S.G. Kim, A.G. Rinzler, D.T. Cobert, G.E. Scuseria, D. Tomanek, J.E. Fisher, R.E. Smalley, *Science* 273 (1996) 483.
- [26] W.K. Maser, E. Munoz, A.M. Benito, M.T. Martinez, G.F. de la Fuente, Y. Maniette, E. Anglaret, J.L. Sauvajol, *Chem. Phys. Lett.* 292 (1998) 587.
- [27] J. Liu, A.G. Rinzler, H. Dai, J.H. Hafner, R.K. Bradley, P.J. Boul, A. Lu, T. Iverson, K. Shelimov, C.B. Huffman, F. Todorquez-Macias, Y.-S. Shon, T.R. Lee, D.T. Colber, R.E. Smalley, *Science* 280 (1998) 1253.
- [28] K.B.K. Teo, C. Singh, M. Chhowalla, W.I. Milne, *Encyclopedia of Nanoscience and Nanotechnology* 1 (2004) 665.
- [29] P. Nikolaev, M.J. Bronikowski, R.K. Bradley, F. Rohmund, D.T. Colbert, K.A. Smith, R.E. Smalley, *Chem. Phys. Lett.* 313 (1999) 91.
- [30] H. Hongo, M. Yudasaka, T. Ichihashi, F. Nihey, S. Iijima, *Chem. Phys. Lett.* 361 (2002) 349.
- [31] Q. Fu, S. Huang, J. Liu, *J. Phys. Chem. B* 108 (2004) 6124.

- [32] Y. Li, D. Mann, M. Rolandi, W. Kim, A. Ural, S. Hung, A. Javey, J. Cao, D. Wang, E. Yenilmez, Q. Wang, J.F. Gibbons, Y. Nishi, H. Dai, *Nano Lett.* 4 (2004) 317.
- [33] Y. Murakami, S. Chiashi, Y. Miyauchi, M. Hu, M. Ogura, T. Okubo, S. Maruyama, *Chem. Phys. Lett.* 385 (2004) 298.
- [34] M. He, X. Duan, X. Wang, J. Zhang, Z. Liu, C. Robinson, *J. Phys. Chem. B* 108 (2004) 12665.
- [35] A. Cassell, N. Franklin, T. Tomblor, E. Chan, J. Han, H. Dai, *J. Am. Chem. Soc.* 121 (1999) 7975.
- [36] N.R. Franklin, H. Dai, *Adv. Mater.* 12 (2000) 890.
- [37] A. Star, T.-R. Han, J.-C.P. Gabriel, K. Bradley, G. Gruner, *Nano Lett.* 3 (2003) 1421.
- [38] Y. Sun, S.R. Wilson, D.I. Schuster, *J. Am. Chem. Soc.* 123 (2001) 5348.
- [39] M.F. Islam, E. Rojas, D.M. Bergey, A.T. Johnson, A.G. Yodh, *Nano Lett.* 3 (2003) 269.
- [40] J. Zhang, J.-K. Lee, Y. Wu, R.W. Murray, *Nano Lett.* 3 (2003) 403.
- [41] R.J. Chen, Y. Zhang, D. Wang, H. Dai, *J. Am. Chem. Soc.* 123 (2001) 3838.
- [42] X. Wang, Y. Liu, W. Qiu, D.J. Zhu, *Mater. Chem.* 12 (2002) 1636.
- [43] M.J. O'Connell, P. Boul, L.M. Ericson, C. Huffman, Y. Wang, E. Haroz, C. Kuper, J. Tour, K.D. Ausman, R.E. Smalley, *Chem. Phys. Lett.* 42 (2001) 265.
- [44] M. Zheng, A. Jagota, E.D. Semke, B.A. Diner, R.S. Mclean, S.R. Lustig, R.E. Richardson, N.G. Tassi, *Nature materials* 2 (2003) 338.
- [45] E.T. Michelson, I.W. Chiang, J.L. Zimmerman, P.J. Boul, J. Lozano, J. Liu, R.E. Smalley, R.H. Hauge, J.L. Margrave, *J. Phys. Chem. B* 103 (1999) 4318.
- [46] J. Chen, A.M. Rao, S. Lyuksyutov, M.E. Itkis, M.A. Hamon, H. Hu, R.W. Cohn, P.C. Eklund, D.T. Colbert, R.E. Smalley, R.C. Haddon, *J. Phys. Chem. B* 105 (2001) 2525.
- [47] V. Georgakilas, K. Kordatos, M. Prato, D.M. Guldi, M. Holzinger, A. Hirsch, *J. Am. Chem. Soc.* 124 (2002) 760.

- [48] J.L. Bahr, J. Yang, D.V. Kosynkin, M.J. Bronikowski, R.E. Smalley, J.M. Tour, J. Am. Chem. Soc. 123 (2001) 6536.
- [49] F. Pompeo, D.E. Resasco, Nano Lett. 2 (2002) 369.
- [50] H. Peng, L.B. Alemany, J.L. Margrave, V.N. Khabashesku, J. Am. Chem. Soc. 125 (2003) 15174.
- [51] K.A. Williams, P.T.M. Veenhuizen, B.G. de la Torre, R. Eritja, C. Dekker, Nature 420 (2002) 761.
- [52] Y.-P. Sun, K. Fu, Y. Lin, W. Huang, Acc. Chem. Res. 35 (2002) 1096.
- [53] K. Fu, W. Huang, Y. Lin, L.A. Riddle, D.L. Carroll, Y.-P. Sun, Nano Lett. 1 (2001) 439.
- [54] W. Huang, S. Taylor, K. Fu, Y. Lin, D. Zhang, T.W. Hanks, A.M. Rao, Y.-P. Sun, Nano Lett. 2 (2002) 311.
- [55] V. Georgakilas, K. Kordatos, M. Prato, D.M. Guldi, M. Holzinger, A. Hirsch, J. Am. Chem. Soc. 124 (2002) 760.
- [56] N. Tagmatarchis, M. Prato, J. Mater. Chem. 14 (2004) 437.
- [57] M. Holzinger, J. Abraham, P. Whelan, R. Graupner, L. Ley, F. Hennrich, M. Kappes, A. Hirsch, J. Am. Chem. Soc. 125 (2003) 8566.
- [58] E.T. Michelson, C.B. Huffman, A.G. Rinzler, R.E. Smalley, R.H. Hauge, J.L. Margrave, Chem. Phys. Lett. 296 (1998) 188.
- [59] V.N. Khabashesku, W.E. Billups, J.L. Margrave, Acc. Chem. Res. 35 (2002) 1067.
- [60] J.L. Stevens, A.Y. Huang, H. Peng, I.W. Chiang, V.N. Khabashesku, J.L. Margrave, Nano Lett. 3 (2003) 331.
- [61] L. Zhang, V.U. Kiny, H. Peng, J. Zhu, R.F.M. Lobo, J.L. Margrave, V.N. Khabashesku, Chem. Mater. 16 (2004) 2055.
- [62] P.M. Ajayan, O.Z. Zhou, Carbon nanotubes: Synthesis, Structure, Properties, and Applications, edited by M.S. Dresselhaus, G. Dresselhaus, P. Avouris, Springer-Verlag, New York. Topic in Applied Physics 80 (2001) 29.
- [63] J.A. Castellano, Handbook of Display Technology (Academic Press, San Diego 1992).

- [64] A.G. Rinzler, J.H. Hafner, P. Nikolaev, L. Lou, S.G. Kim, D. Tomanek, P. Nordlander, D.T. Colbert, R.E. Smalley, *Science* 269 (1995) 1550.
- [65] W. Zhu, C. Bower, O. Zhou, G.P. Kochanski, S. Jin, *Appl. Phys. Lett.* 75 (1999) 873.
- [66] Q.H. Wang, A.A. Setlur, J.M. Laruerhass, J.Y. Dai, E.W. Seelig, R.H. Chang, *Appl. Phys. Lett.* 72 (1998) 2912.
- [67] P. Selvam, B. Viswanathan, C.S. Swamy, V. Srinivasan, *International Journal of Hydrogen Energy* 13 (1988) 87.
- [68] A.C. Dillon, M.J. Heben, *Appl. Phys. A* 72 (2001) 133.
- [69] A.C. Dillon, K.M. Jones, T.A. Bekedahl, C.H. Kiang, D.S. Bethne, M.J. Heben, *Nature* 386 (1997) 377.
- [70] C. Nützenadel, A. Zttel, D. Chartouni, L. Schlapbach, *Electrochemical and Solid-State Letters*, 2 (1999) 30.
- [71] S.M. Lee, K.S. Park, Y.C. Choi, Y.S. Park, J.M. Bok, D.J. Bae, K.S. Mahm, Y.G. Choi, S.C. Yu, N. Kim, T. Frauenheim, Y.H. Lee, *Synthetic Metals* 11 (2000) 209.
- [72] Y. Ye, C.C. Ahn, C. Witham, B. Fultz, J. Liu, A.G. Rinzler, D. Colbert, K.A. Smith, R.E. Smalley, *Appl. Phys. Lett.* 74 (1999) 2307.
- [73] P. Chen, X. Wu, J. Lin, K. Tan, *Science* 285 (1999) 91.
- [74] M. Hirscher, M. Becher, M. Haluska, U. Dettlaff-Weglikowska, A. Quintel, G.S. Duesberg, Y.-M. Choi, P. Downes, M. Hulman, S. Roth, I. Stepanek, P. Bernier, *Appl. Phys. A* 72 (2001) 129.
- [75] M. Shiraishi, T. Takenobu, M. Ata, *Chem. Phys. Lett.* 367 (2003) 633.
- [76] H. Kajiura, S. Tsutsui, K. Kadono, M. Kakuta, M. Ata, *Appl. Phys. Lett.*, 82 (2003) 1105.
- [77] D.V. Schur, B.P. Tarasov, S.Y. Zaginaichenko, V.K. Pishuk, T.N. Veziroglu, Y. M. Shul'ga, A.G. Dubovoi, N.S. Anikina, A.P. Pomytkin, A.D. Zolotareno, *International Journal of Hydrogen Energy* 27 (2002) 1063.
- [78] L. Schlapbach, A. Zuttel, *Nature* 414 (2001) 353.
- [79] M.G. Nijkamp, J.E.M.J. Raaymakers, A.J.V. Dillen, K.P.D. Jong, *App. Phys. A* 72 (2001) 619.

- [80] C. Liu, Y.Y. Fan, M. Liu, H.T. Cong, H.M. Cheng, M.S. Dresselhaus, *Science* 28-6 (1999) 1127.
- [81] B.I. Yakobson, C.J. Bernholc, *Phys. Rev. Lett.* 76 (1996) 2511.
- [82] X. Zhang, T. Liu, T.V. Sreekumar, S. Kumar, V.C. Moore, R.H. Hauge, R.E. Smalley, *Nano Lett.* 3 (2003) 1285.
- [83] R. Sen, B. Zhao, D. Perea, M.E. Itkis, H. Hu, J. Love, E. Bekyarova, R.C. Haddon, *Nano Lett.* 4, 459-464 (2004).
- [84] P. Lidström, J. Tierney, B. Wathey, J. Westman, *Tetrahedron* 57 (2001) 9225.
- [85] Retrieved from the website of <http://homepages.ed.ac.uk/ah05/ch1a.html>.
- [86] Retrieved from the website of <http://homepages.ed.ac.uk/ah05/basicintro.html>.
- [87] Y. Murakami, S. Chiashi, Y. Miyauchi, M. Hu, M. Ogura, T. Okubo, S. Maruyama, *Chem. Phys. Lett.* 385 (2004) 298.
- [88] H. Konno, S. Sato, H. Habazaki, M. Inagaki, *Carbon* 42 (2004) 2756.
- [89] X. Ding, L. Huang, X.T. Zeng, S.P. Lau, B.K. Tay, W.Y. Cheung, S.P. Wong, *Carbon* 42 (2004) 3030.
- [90] H.M. Christen, A.A. Puretzky, H. Cui, K. Belay, P.H. Fleming, D.B. Geohegan, D.H. Lowndes, *Nano Lett.* 4 (2004) 1939.
- [91] S. Maruyama, R. Kojima, Y. Miyauchi, S. Chiashi, M. Kohno, *Chem. Phys. Lett.* 360 (2002) 229.
- [92] E. Guibal, *Separation and Purification Technology* 38 (2004) 43.
- [93] V.N. Kislenco, *Journal of Colloid and Interface Science* 275 (2004) 183.
- [94] J.H. Kim, J. Won, Y.S. Kang, *Journal of Membrane Science* 237 (2004) 199.
- [95] M. Rhazi, J. Desbrières, A. Tolaimate, M. Rinaudo, P. Vottero, A. Alagui, *Polymer* 43 (2002) 1267.
- [96] B.R. Azamian, J.J. Davis, K.S. Coleman, C.B. Bagshaw, M.L.H. Green, *J. Am. Chem. Soc.* 124 (2002) 12664.
- [97] A. Guiseppi-Elie, C. Lei, R.H. Baughman, *Nanotechnology* 13 (2002) 559.

- [98] S.G. Wang, Q. Zhang, R. Wang, S.F. Yoon, J. Ahn, D.J. Yang, J.Z. Tian, J.Q. Li, Q. Zhou, *Electrochem. commun.* 5 (2003) 800.
- [99] S.G. Wang, Q. Zhang, R. Wang, S.F. Yoon, *Biochem. Biophys. Res. Commun.* 3-11 (2003) 572.
- [100] X. Yu, D. Chattopadhyay, I. Galeska, F. Papadimitrakopoulos, J.F. Rusling, *Electrochem. Commun.* 5 (2003) 408.
- [101] Y. Lin, F. Lu, Y. Tu, Z. Ren, *Nano Lett.* 4 (2004) 191.
- [102] M.J. Bronikowski, P.A. Willis, D.T. Colbert, K.A. Smith, R.E. Smalley, *J. Vacuum Sci. Technol. A* 19 (2001) 1800.
- [103] A. Goyal, Y. Wang, R. Sharma, Z. Iqbal, "Bulk Growth of Single and Double Wall Carbon Nanotubes by CO Disproportionation at Atmospheric Pressure", in preparation.
- [104] L. Feng, H. Li, F. Li, Z. Shi, Z. Gu, *Carbon* 41 (2003) 2385.
- [105] W. Huang, S. Taylor, K. Fu, Y. Lin, D. Zhang, T.W. Hanks, A.M. Rao, Y.-P. Sun, *Nano Lett.* 2 (2002) 311.
- [106] C.A. Dyke, J.M. Tour, *J. Am. Chem. Soc.* 125 (2003) 1156.
- [107] R.K. Saini, I.W. Chiang, H. Peng, R.E. Smalley, W.E. Billups, R.H. Hauge, J.L. Margrave, *J. Am. Chem. Soc.* 125 (2003) 3617.
- [108] C. Journet, W.K. Maser, P. Bernier, A. Loiseau, M. Lamy de la Chapelle, S. Lefrant, P. Deniard, R. Lee, J.E. Fischer, *Nature* 388 (1997) 756.
- [109] F. Pompeo, D.E. Resasco, *Nano Lett.* 2 (2002) 369.
- [110] F. Bensebaa, F. Zavaliche, P. L'Ecuyer, R.W. Cochrane, T. Veres, *J. Colloid Interface Sci.* 277 (2004) 104.
- [111] G. Zhou, V.G. Pol, O. Palchik, R. Kerner, E. Sominski, Y. Koltypin, A. Gedanken, *J. Solid State Chem.* 177 (2004) 361.
- [112] A. Loupy, *C. R. Chimie* 7 (2004) 103.
- [113] A. Shaabani, A. Bazgir, *Tetrahedron Lett.* 45 (2004) 2575.
- [114] M. Ardon, G. Hogarth, D.T.W. O'croft, *J. Organomet. Chem.* 689 (2004) 2429.
- [115] A. Lew, P.E. Krutzik, M.E. Hart, A.R. Chamberlin, *J. Comb. Chem.* 4 (2002) 95.

- [113] G.A. Strohmeier, C.O. Kappe, *J. Comb. Chem.* 4 (2002) 154.
- [117] D.A. Lewis, J.D. Summers, T.C. Ward, J.E. McGrath, *J. Polym. Sci. A* 30 (1992) 653.
- [118] Y. Lin, A.M. Rao, B. Sadanadan, E.A. Kenik, Y.P. Sun, *J. Phys. Chem. B* 106 (2002) 1294.
- [119] Y.P. Sun, K. Fu, Y. Lin, W. Huang, *Acc. Chem. Res.* 35 (2002) 1096.
- [120] H. Pan, L. Liu, Z.X. Guo, L. Dai, F. Zhang, D. Zhu, R. Czerw, D.L. Carroll, *Nano Lett.* 3 (2003) 29.
- [121] C.A. Mitchell, J.L. Bahr, S. Arepalli, J.M. Tour, R. Krishnamoorti, *Macromolecules* 5 (2002) 8825.
- [122] W. Zhu, N. Minami, S. Kazaoui, Y.J. Kim, *Mater. Chem.* 14 (2004) 1924.
- [123] L. Zhang, V.U. Kiny, H. Peng, J. Zhu, R.F.M. Lobo, J.L. Margrave, V.N. Khabashesku, *Chem. Mater.* 16 (2004) 2055.
- [124] S. Qin, D. Qin, W.T. Ford, D.E. Resasco, J.E. Herrera, *Macromolecules* 37 (2004) 752.
- [125] Y. Lin, L.F. Allard, Y.-P. Sun, *J. Phys. Chem. B* 108 (2004) 3760.
- [126] Y. Wang, Z. Iqbal, S. Malhotra, *Chem. Phys. Lett.* 402 (2005) 96.
- [127] Y. Wang, Z. Iqbal, S. Mitra, *Carbon* 43 (2005) 1015.
- [128] D. Lin-Vien, N.B. Colthup, W.G. Fateley, J.G. Grasselli, "The Handbook of Infrared and Raman Characteristic Frequencies of Organic Molecules", Academic Press, New York (1991), Chap. 11.
- [129] Z. Iqbal, *Nanostructured Carbon for Advanced Applications*, Kluwer Academic Publishers, Dordrecht, 2001, p. 309.
- [130] Y. Wang, Z. Iqbal, *Mater. Res. Soc. Symp. on Materials for Hydrogen Storage*, 837 (2005) N4.4.1.
- [131] L.J. Bellamy, "The Infra-red Spectra of Complex Molecules", Chapman and Hall, London (1975) 332.
- [132] F.J. Owens, unpublished.

- [134] M. Shiraishi, T. Takenobu, A. Yamada, M. Ata, H. Kataura, *Chem. Phys. Lett.* 3-58 (2002) 213.
- [135] M. Ritschel, M. Uhlemann, O. Gutfleisch, A. Leonhardt, A. Graff, C. Täschner, J. Fink, *Appl. Phys. Lett.*, 80 (2002) 2985.
- [136] Y. Wang, S. Malhotra, Z. Iqbal, *Mater. Res. Soc. Symp. Proc.* 800 (2004) 351.
- [137] W.A. Curtin, B.W. Sheldon, *Materials Today* 7 (2004) 44.
- [138] R. Kamalakaran, F. Lupo, N. Grobert, T. Scheu, N.Y. Jin-Phillipp, M. Ruhle, *Carbon* 42 (2004) 1.
- [139] S.B. Sinnott, O.A. Shenderova, C.T. White, D.W. Brenner, *Carbon* 36 (1998) 1.
- [140] O. Lourie, H.D. Wagner, *Appl. Phys. Lett.* 73 (1998) 3527.
- [141] A. Peigney, C.H. Laurent, E. Flahaut, A. Rousset, *Ceram. Int.* 26 (2000) 677.
- [142] S. Singh, Y. Pei, R. Miller, P.R. Sundararajan, *Advanced Functional Materials* 13 (2003) 868.
- [143] H. Ye, H. Lam, N. Titchenal, Y. Gogotsi, F. Ko, *Appl. Phys. Lett.* 85 (2004) 1775.
- [144] X. Zhou, E. Shin, K.W. Wang, C.E. Bakis, *Composites Science and Technology* 64 (2004) 2425
- [145] J. Zhu, H. Peng, F. Rodriguez-Macias, J.L. Margrave, V.N. Khabashesku, A.M. Imam, K. Lozano, E.V. Barrera, *Advanced Functional Materials* 14 (2004) 643.
- [146] K. Lau, C. Gu, G. Gao, H. Ling, S.R. Reid, *Carbon* 42 (2004) 426.
- [147] N. Tai, M. Yeh, J. Liu, *Carbon* 42 (2004) 2774.
- [148] X. Wang, N.P. Padture, H. Tanaka, *Nature materials* 3 (2004) 539.
- [149] P.M. Ajayan, O.Z. Zhou, *Carbon nanotubes: Synthesis, Structure, Properties, and Applications*, edited by M.S. Dresselhaus, G. Dresselhaus, P. Avouris, Springer-Verlag, New York. *Topic in Applied Physics* 80 (2001) 391.
- [150] G. Xi, Y. Peng, S. Wan, T. Li, W. Yu, Y. Qian, *J. Phys. Chem. B.* 108 (2004) 20102.
- [151] H. Kong, C. Gao, D. Yan, *Macromolecules* 37 (2004) 4022.

- [152] Y. Lin, B. Zhou, K.A.S. Fernando, P. Liu, L.F. Allard, Y.-P. Sun, *Macromolecules* 36 (2003) 7199.
- [153] J.L. Kendall, D.A. Canelas, J.L. Young, J.M. DeSimone, *Chem. Rev.* 99 (1999) 543.
- [154] B. Yue, J. Yang, Y. Wang, C. Huang, R. Dave, R. Pfeffer, *Powder Technology* 46 (2004) 32.
- [155] B. Yue, J. Yang, R. Dave, R. Pfeffer, C. Huang, In Review.
- [156] T. Matsumoto, T. Komatsu, K. Arai, T. Yamazaki, M. Kijima, H. Shimizu, Y. Takasawa, J. Nakamura, *Chem. Commun.* 7 (2004) 840.
- [157] H. Tang, J.H. Chen, Z.P. Huang, D.Z. Wang, Z.F. Ren, L.H. Nie, Y.F. Kuang, S.-Z. Yao, *Carbon* 42 (2004) 191.
- [158] M.M. Christine, D.M. Shelley, S.B. Martin, *Lab on a Chip* 5 (2005) 218.
- [159] C. Cai, J. Chen, *Analy. Biochem.* 332 (2004) 75.
- [160] E. Katz, I. Willner, A.B. Kotlyar, *J. Electroanal. Chem.* 479 (1998) 64.